

1-1-2010

Metal Chalcogenide Nanocrystal Assembly: From Synthesis To Applications

Qinghong Yao
Wayne State University,

Follow this and additional works at: http://digitalcommons.wayne.edu/oa_dissertations

Recommended Citation

Yao, Qinghong, "Metal Chalcogenide Nanocrystal Assembly: From Synthesis To Applications" (2010). *Wayne State University Dissertations*. Paper 38.

This Open Access Dissertation is brought to you for free and open access by DigitalCommons@WayneState. It has been accepted for inclusion in Wayne State University Dissertations by an authorized administrator of DigitalCommons@WayneState.

**METAL CHALCOGENIDE NANOCRYSTAL ASSEMBLY: FROM
SYNTHESIS TO APPLICATIONS**

by

QINGHONG YAO

DISSERTATION

Submitted to the Graduate School

of Wayne State University,

Detroit, Michigan

in partial fulfillment of the requirements

for the degree of

DOCTOR OF PHILOSOPHY

2010

MAJOR: CHEMISTRY (Inorganic)

Approved by:

Advisor

Date

DEDICATION

To my beloved parents, husband and daughter

ACKNOWLEDGEMENTS

My deepest gratitude goes to my advisor, Prof. Stephanie L. Brock. I would like to thank her for her continuous advices, encouragement, and support all through my graduate study in Wayne State University. It was a great experience for me to study and work under her guidance. She is always patient, supportive and friendly to me and the other students. She is always available for students to talk with even when she is extremely busy. She gave me numerous valuable advices, which are not only on my research study, but also on my long-term career development. Her deep knowledge, great passion for science, and logic way of thinking has made a deep impression on me. Under her guidance, I have started to learn how to work and think independently, conduct research work with a critical eye and write papers in a scientific way, even though I am still learning and have a long way to go.

I would like to take this opportunity to thank my dissertation committee members, Prof. Charles H. Winter, Prof. Andrew Feig and Prof. Gavin Lawes. Their valuable suggestions and comments have made great help for the achievement of this dissertation. I would also like to thank Prof. Claudio N. Verani and Prof. Christy S. Chow for writing recommendation letters for me and sending them on time. Additionally, I want to thank Prof. Christy S. Chow and Prof. Ayad Al-Katib for their research collaborations, from which I have learnt many new interesting and useful experimental techniques and research skills.

I would also like to thank Mr. Keshab Rijal (Prof. Chow's group) and Ms. Kristina Cole (Prof. Al-Katib's group) for their collaborative work, tips and valuable discussions.

Characterization techniques are very important in this dissertation study, on which I spent a lot of time in Central Instrument Facility (CIF) of Department of Chemistry in WSU. I am very grateful to Dr. Yi Liu for the initial training on transmission electron microscopy and scanning electron microscopy instruments and the following numerous times of kind assistance and valuable suggestions for TEM and SEM analysis all through my Ph.D study. My thank also goes to Dr. Mary Jane Heeg for the training on powder X-ray diffractometry and her good maintenance of the instrument; Ms. Sharla Wood for her hard work on maintaining the “small” instruments in CIF; Dr. Eric McCullen of the Smart Sensors Institute at WSU for assistance with XPS; Marty Krol and Nestor Ocampo for their kind help on computer and internet maintenance.

I would like to express my gratitude to all the staff members in the Department of Chemistry, especially to Ms. Sharon Kelly, Ms. Debbie McCreless, Ms. Melissa Barton, Ms. Mary Wood and Ms. Erin Bachert. I am grateful to all the staff members of Science Store for their hard work to ensure the purchase and arrival of chemicals and apparatus.

My thankful feeling goes to the past Brock group members for their help during the beginning time of my Ph.D study. My special thanks go to Dr. Indika Arachchige, who gave me the initial training on the synthesis of nanoparticles and aerogels and several characterization techniques. He was always happy to share his wonderful research experiences and ready to answer my numerous questions. I really appreciate Dr. Kennedy Kalebaila and Dr. Kristy Gregg’s great suggestions on how to improve my synthesis and

characterization skills. My appreciation also goes to Dr. Keerthi Senevirathne for his help on inert atmosphere experimental techniques and discussions. I am also grateful to the rest of the past group members, Dr. Hongtao Yu, Ms. Valentina Ganzha-Hazen and Dr. Palaniappan Arumugam (Pops) for their kind interactions. My grateful feeling goes to all of the current Brock group members. My special thanks go to my classmate, Elayaraja Muthuswamy. He is a wonderful and helpful person to work with. I am also very grateful to have the rest of the current group members as my colleagues: Irina Pala, Shreya Ganguly, Yanhua Zhang, Layan Savithra, Lasantha Perera and Asha Bhandara for their great friendship, research discussions, coffee breaks, parties, and birthday presents.

Finally, I would like to express my deepest gratitude to my beloved parents for their love, encouragement and sacrifices through my life. I am very grateful to my beloved sisters. Although they are far away from me, their love and numerous phone calls always encourage me to do better. I am deeply grateful to my beloved husband for his love, tremendous supports and understanding over these years. Last but not least, my deep love and thanks go to my precious daughter for her wonderful smile.

TABLE OF CONTENTS

Dedication	ii
Acknowledgements	iii
List of Tables	vii
List of Figures	viii
List of Schemes	x
Chapter 1 – Introduction.....	1
Chapter 2 – Experimental and Characterization Techniques.....	31
Chapter 3 – Porous CdTe Nanocrystal Assemblies: Ligation Effects on the Gelation Process and the Properties of Resultant Aerogels.....	59
Chapter 4 – Cation Exchange Reactions in Metal Chalcogenide Aerogels: Ag ₂ Se, PbSe and CuSe Gels and Aerogels.....	82
Chapter 5 – Optical Sensing of Triethylamine Using CdSe Aerogels.....	97
Chapter 6 – Conclusions and Prospectus.....	131
References	137
Abstract.....	148
Autobiographical Statement.....	150

LIST OF TABLES

Table 3.1	EDS data of CdTe nanocrystals and aerogels.....	68
Table 3.2	Porosimetry data for CdTe aerogels.....	71
Table 4.1	Atomic ratios of CdSe, Ag ₂ Se, CuSe and PbSe aerogels obtained by EDS.....	89
Table 4.2	Porosimetry data for CdSe and Ag ₂ Se aerogel.....	93
Table 5.1	Structure, crystallite size, elemental composition and optical properties of CdSe nanoparticle precursors and aerogels.....	102
Table 5.2	Elemental composition and porosimetry data for as-prepared, heated and pyridine-washed CdSe aerogels, pre- and post-sensing.....	120

LIST OF FIGURES

Figure 1.1 A schematic illustration of the electronic states in bulk and Nanocrystalline semiconductors.	2
Figure 1.2 Spatial electronic state correlation diagram for a nanocrystalline semiconductor.	4
Figure 1.3 Schematic illustrations of 1D, 2D and 3D assemblies of nanocrystals.....	14
Figure 1.4 Schematic illustration of drying methods for generation of aerogels, ambigels and xerogels from wet gels.....	19
Figure 2.1 Phase diagram of CO ₂ and an illustration of a possible supercritical drying path.....	34
Figure 2.2 Schematic illustration of the formation of an X-ray as an M shell electron drops down to the vacancy in the K shell level, which was left by an ionized K shell electron.	36
Figure 2.3 Schematic illustration of the diffraction of X-rays by crystal planes.....	37
Figure 2.4 Schematic illustration of possible processes when an incident electron beam interacts with a specimen.	40
Figure 2.5 Six basic types of adsorption/desorption isotherms	48
Figure 3.1 PXRD pattern of TOPO-capped CdTe nanocrystals. The ICDD-PDF overlay of hexagonal CdTe (PDF # 19-0193, solid lines) is shown as vertical lines.....	63
Figure 3.2 PXRD pattern of MUA exchanged CdTe nanocrystals. The ICDD-PDF overlays of hexagonal CdTe (PDF # 19-0193, solid lines) and hexagonal Te (PDF # 85-0557, dotted lines) are shown as vertical lines.....	64
Figure 3.3 PXRD pattern of TOPO-capped and MHA-capped aerogels	

and of TOPO capped CdTe nanocrystals. The ICDD-PDF overlay of hexagonal CdTe (PDF # 19-0193) are shown as vertical lines. * indicates the most intense reflection of crystalline Te.....66

Figure 3.4 TEM images of MHA-capped [A] and TOPO-capped [B] aerogels (left, low resolution; right, high resolution). Groups of lattice fringes, and their corresponding d-spacing and indices, are shown in the high resolution images.....67

Figure 3.5 N₂ adsorption (filled circles) /desorption (filled squares) isotherm of TOPO-capped (a) and MHA-capped CdTe aerogel; the inset shows the BJH pore size distribution.....70

Figure 3.6 Optical absorption (data converted from diffuse reflectance) spectra of TOPO-capped nanocrystals (TOPO-CdTe NCs) (black squares), and TNM oxidized MHA-capped aerogels (TNM-MHA-CdTe AGs) (red circles), TOPO-capped aerogel (TOPO-CdTe AGs) (blue triangles) and photo-oxidized MHA-capped aerogels (PO-MHA-CdTe AGs) (white triangles).....72

Figure 3.7 Photoluminescence spectra of TOPO-capped (black triangles) and MHA-capped (blue circles) CdTe nanocrystals, and heated TNM oxidized MHA-capped CdTe aerogels (red squares), photo-oxidized MHA-capped CdTe aerogels (purple triangles), unheated TNM oxidized MHA-capped CdTe aerogels (white circles) and TOPO-capped CdTe aerogels (white triangles).....73

Figure 3.8 TEM image of a dispersed TOPO-capped CdTe aerogel solution. The inset shows a high resolution TEM image of a single nanocrystal of CdTe.....74

Figure 4.1 Photograph of initial CdSe wet gel (left), Ag⁺ exchanged CdSe wet gel (middle), and resultant Ag₂Se aerogel (right).....85

Figure 4.2 PXRD pattern of the CdSe aerogel [A], Ag₂Se aerogel [B], PbSe aerogel [C] and CuSe aerogel [D]. The ICDD-PDF overlays of hexagonal CdSe (PDF # 08-0459), cubic Ag₂Se (PDF # 27-0619), cubic PbSe (PDF # 78-1903) and hexagonal CuSe (PDF # 27-0185) are shown as lines in [A] through [D], respectively. The inset images show the crystal structure of hexagonal CdSe [A] and cubic Ag₂Se (cation

sites partially occupied) [B]..	87
Figure 4.3 EDS spectra of aerogels of CdSe [A, top], Ag ₂ Se [A, bottom], PbSe [B] and CuSe [C]. EDS of PbSe was acquired by TEM/EDS, the rest of aerogels were analyzed by SEM/EDS. The presence of Si in the PbSe aerogel [B] is attributed adventitious dust and Cu is de to the copper grid upon which the PbSe sample was deposited for TEM measurements.....	89
Figure 4.4 Optical absorption [A] (data converted from diffuse reflectance) and photoluminescence spectra [B] of the initial CdSe aerogel (grey) and Ag ₂ Se aerogel (black).....	91
Figure 4.5 Transmission Electron Micrographs of CdSe [A], Ag ₂ Se [B], CuSe [C] and PbSe [D] aerogels.....	92
Figure 4.6 N ₂ adsorption (filled circles)/desorption (filled squares) isotherms of an Ag ₂ Se aerogel. The inset shows the corresponding BJH modeled pore size distribution.....	94
Figure 4.7 Photograph of partially exchanged CdSe wet gel, sliced in two.....	95
Figure 5.1 Experimental set-up for probing TEA sensing by CdSe aerogels..	99
Figure 5.2 PXRD pattern of the CdSe nanoparticle precursor and resultant aerogels. The ICDD-PDF overlay of hexagonal CdSe (PDF # 08-0459) is shown as vertical lines.	101
Figure 5.3 Optical absorption and photoluminescence spectra of CdSe nanoparticles (TOPO-capped) and the corresponding aerogel (excitation wavelength: 450 nm).....	104
Figure 5.4 N ₂ adsorption (filled circles)/desorption (filled squares) isotherms of a typical CdSe aerogel. The inset shows the BJH modeled pore size distribution..	104
Figure 5.5 PL changes for as-prepared CdSe aerogels when alternating the exposure of aerogels to argon and TEA (a) static mode (b) kinetic mode. The sample was excited at 450 nm and the emission at 538 nm was monitored in the kinetic mode. The flow rate was 50 mL/min	

and the TEA partial pressure was 0.007 atm (TEA concentration: 7×10^3 ppm).....	107
Figure 5.6 PXRD patterns of as-prepared and heated aerogels. The ICDD-PDF overlay of hexagonal CdSe (PDF # 08-0459) is shown as vertical lines.	109
Figure 5.7 IR spectra of as-prepared (bottom) and heated (top) CdSe aerogels. Data were acquired using KBr pellets with identical weight percents of CdSe aerogel.....	109
Figure 5.8 PL changes for vacuum annealed CdSe aerogels when alternating the exposure of aerogels to argon and TEA: (a) static mode, (b) kinetic mode. The peak at 600 nm in (a) marked with an * is due to the glass wool used to preclude movement of the aerogel sample during testing. The sample was excited at 450 nm and monitored at an emission wavelength of 541 nm in the kinetic mode. A flow rate of 100 mL/min and a TEA partial pressure of 0.075 atm (TEA concentration: 7.5×10^4 ppm) were employed.	111
Figure 5.9 Cd and Se 3d regions of XPS spectra of as-prepared and heated CdSe aerogels.....	113
Figure 5.10 PXRD patterns of as-prepared and pyridine-washed aerogels. The ICDD-PDF overlays of hexagonal CdSe (PDF # 08-0459) are shown as vertical lines	115
Figure 5.11 IR spectra of as-prepared (bottom) and pyridine-washed (top) CdSe aerogels. Data were acquired using KBr pellets with identical weight percents of CdSe aerogel.....	115
Figure 5.12 (a) PL spectra of the pyridine washed and as-prepared CdSe aerogel, (b) kinetic PL mode showing PL changes for the pyridine washed CdSe aerogels when alternating the exposure of aerogels to argon and TEA. The sample was excited at 450 nm and monitored at an emission wavelength of 520 nm. A flow rate of 100 mL/min and a TEA partial pressure of 0.075 atm (TEA concentration: 7.5×10^4 ppm) were employed.....	117
Figure 5.13 Se 3d regions of XPS spectra of as-prepared and pyridine-washed CdSe aerogels.....	118

Figure 5.14 PXRD patterns of as-prepared, heated and pyridine-washed CdSe aerogels pre-sensing and post-sensing. The ICDD-PDF overlays of hexagonal CdSe (PDF # 08-0459) are shown as vertical lines.....	121
Figure 5.15 TEM micrographs of as-prepared (a, b, c, d), heated (e, f) and pyridine-washed (g, h) CdSe aerogels pre-sensing (a, c, e, g) and post-sensing (b, d, f, h).....	122
Figure 5.16 XPS spectra of as-prepared, heated and pyridine-washed CdSe aerogels pre- and post-sensing. The ionization at ca. 59 eV in the Se XPS corresponds to SeO ₂	123
Figure 5.17 IR spectra of as-prepared, heated and pyridine-washed CdSe aerogels pre- and post-sensing.....	124
Figure 5.18 PL changes as a function of TEA concentration (a) for two independently prepared monolithic CdSe aerogels and (b) for the same monolithic aerogel sample (sample A) over three cycles. The flow rate was fixed at 100 mL/min.....	126
Figure 5.19 Langmuir adsorption isotherm for sample A for the 2nd and 3rd testing cycles; the lines serve to guide the eyes. The inset presents a double-reciprocal plot for the same data; the lines represent a linear fit of the data.....	129

LIST OF SCHEMES

Scheme 3.1	Proposed mechanism of TOPO capped and MHA-capped CdTe oxidative gelation and reductive dispersion.....	79
-------------------	--	----

CHAPTER 1

INTRODUCTION

1.1 Semiconductor Nanocrystals

As a rapidly growing multidisciplinary research area, semiconductor nanocrystal research has received great attention from a wide range of scientists, including physicists, chemists, material scientists, engineers, and biologists. This extensive interest arises from the unique optical and electronic properties of semiconductor nanocrystals that dramatically distinguishes them from their bulk counterparts.¹ In a bulk semiconductor, the essentially infinite number of atomic orbitals overlaps and forms continuous energy levels, leading to the formation of conduction and valence bands.² In contrast to metallic materials, intrinsic semiconductors have a completely separated conduction band and valence band with a constant band gap (HOMO-LUMO separation) in the range of 0.3 to 3.8 eV depending on the identity of the material.^{1,2} In the case of a semiconductor of nanocrystalline size, the band gap energy increases as the physical size of the material decreases within a critical range. Specifically, when the size decreases below the bulk exciton Bohr radius, there are not a sufficient number of atoms to form the continuum of energy levels. Instead, electrons and holes are quantum confined in three dimensions by the nanocrystallite, resulting in the breakdown of continuous energy bands into discrete atomic-like energy states, as illustrated in Figure 1.1.^{1,3,4} Depending on the identity of the semiconductor (IV, III-V, II-VI or IV-VI group), the critical radius can be widely different, ranging from 2 nm to 60 nm.¹

As previously mentioned, a consequence of quantum confinement is a blue shift of the first excitonic absorption peak in comparison to that for the corresponding bulk material.

By means of an effective mass approximation model, Brus has shown that the magnitude of the blue shift of the band gap energy is approximately inversely proportional to the size of the semiconductor nanocrystals.⁵⁻⁷ The blue shift of the band gap energy can be calculated by

$$\Delta E_g = (\hbar^2/8R^2)(1/m_e + 1/m_h) - 1.8e^2/4\pi\epsilon_0\epsilon R \quad (1.1)$$

in which R is the nanocrystal radius, m_e is the effective mass of the electron in the semiconductor, m_h is the effective mass of the hole in the semiconductor, ϵ is the dielectric constant of the semiconductor, and ϵ_0 is the permittivity of a vacuum.^{6,7} The ability to tune optical absorption and emission properties by varying particle size facilitates the application of nanocrystals for a range of uses, including sensors, photovoltaics, light emitting diodes (LED), biomedical labels and so on.^{1,3}

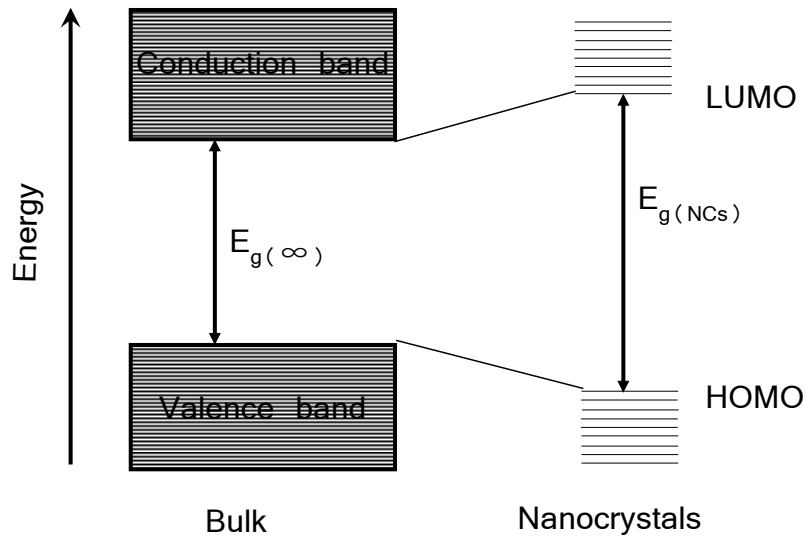


Figure 1.1. A schematic illustration of the electronic states in bulk and nanocrystalline semiconductors (adapted from Steigerwald and Brus⁵).

Along with size-dependent opto-electronic properties, a second important feature of semiconductor nanocrystals is the increase in surface to volume ratio with diminishing particle size; such that a 2.8 nm diameter CdSe particle has 37% of its atoms on the surface, which drops to < 1 % in its bulk form. As a result, the surface composition and structure strongly influence both the physical and chemical properties of semiconductor nanocrystals. For example, the photoluminescence properties can be dramatically different depending upon the passivation of the nanocrystal surface. In general, the nanocrystal surface often contains trap states caused by defects (vacancies or local lattice mismatches), unsaturated bonds (dangling bonds), surface ligands or other adsorbates on the surface (Figure 2). The excited electron or hole can be trapped by these energy states, thereby circumventing band-edge to band-edge radiative recombination yielding diminished band-edge luminescence. Recombination of these trapped electrons and holes can lead to trap-state luminescence that appears as characteristic broad emission band at a lower energy than the band-edge luminescence.³ To obtain enhanced band-edge luminescence, a well passivated surface is needed. The depassivation can be achieved by overcoating the nanocrystal core with organic ligands or a secondary inorganic phase (shell).³ It has been well documented that certain coordinating ligands (alkyl phosphine oxides, alkyl amines⁸⁻¹⁰ and fatty acids^{11, 12}) can provide efficient passivation of the nanocrystal surface. A second semiconducting phase with a wider band gap grown on the nanocrystal core has proven to be even more effective at passivation.³ ZnS is one of the most widely used shell materials for CdSe nanocrystals due to its wide band gap (3.6 eV)

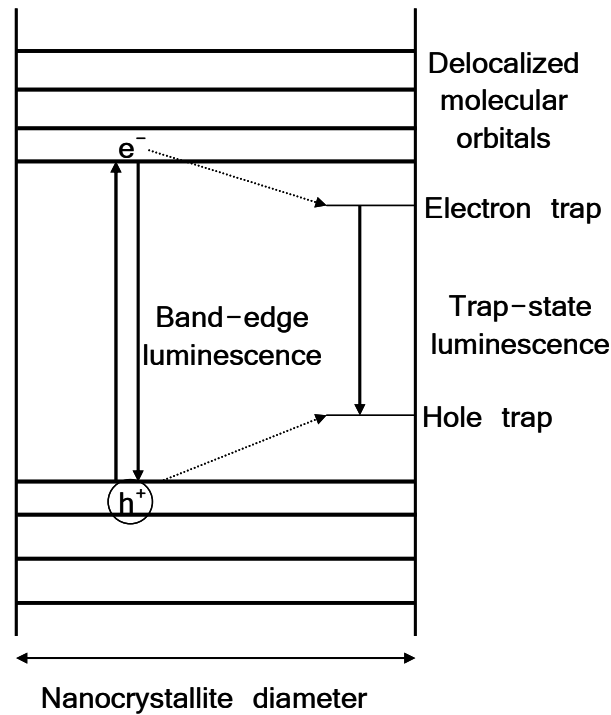


Figure 1.2. Spatial electronic state correlation diagram for a nanocrystalline semiconductor (adapted from Chestnoy and Brus¹³).

1.2 Metal Chalcogenide Nanocrystals

Semiconducting metal chalcogenide nanocrystals (II-VI and IV-VI) are a class of materials that exhibit band gap energies spanning from the mid-to-near infrared (PbS, PbSe, PbTe) to the visible (CdS, CdSe, CdTe) and into the ultraviolet (ZnS, ZnSe) region. In particular, CdE (E = S, Se, Te) nanocrystals and their core/shell formulations (e.g. CdSe/ZnS) have been of great interest to nanomaterial scientists due to their relatively easy synthesis, the ability to produce high quality nanocrystals in terms of size and shape, and the associated capability to tune the absorption and emission throughout the visible region.

Cadmium based chalcogenide nanocrystals are regarded to be promising materials for biological imaging.¹⁴ Compared to conventional fluorophores (e.g. organic dyes), semiconductor nanocrystals have several advantages as fluorescent labels. Along with a relatively long fluorescence lifetime (hundreds of nanoseconds), they show a narrow, tunable, symmetric emission spectrum, and they are photo-chemically stable.¹⁵ However, the utility of nanocrystals in fluorescence imaging was initially prohibited by their insolubility in aqueous media due to the hydrophobic surface of nanocrystals (as dictated by the surface capping groups). The insolubility problem has been overcome by modification of the nanocrystal surface with phospholipids,¹⁶ amphiphilic polymers,¹⁷ dendrimers,¹⁸ and oligomeric phosphines¹⁹ to facilitate the conjugation of nanocrystals to proteins and peptides, enabling their use in bio-imaging and bio-sensing. In addition, CdE nanocrystals are promising candidates for fabrication of optical devices. Early in 1994, Alivisatos and co-workers reported a hybrid organic/inorganic LED device based on a multilayer structure alternatively assembled by CdSe nanocrystallite layers with indium tin oxide (ITO) and semiconducting *p*-paraphenylene vinylene (PPV) thin films.²⁰ The device could emit light from red to yellow by using the nanocrystal size from 5 nm to 3 nm.

Optical sensing applications of CdSe nanocrystals are of particular interest to this dissertation research. The use of CdSe for sensing of Lewis bases has been previously demonstrated for both single crystals²¹ and nanoparticle–polymer composites.²² Meyer *et al.*²¹ have studied the PL properties of CdSe single crystals in the presence of gaseous amines, observing enhanced PL when single-crystal CdSe samples (etched with Br₂/MeOH to obtain Cd rich, (0001) faces) were exposed to a series of amines: NH₃, CH₃NH₂, (CH₃)₂NH, and (CH₃)₃N. The PL enhancement trend was correlated with the intrinsic basicity of the amines,

which provides evidence for acid–base adduct formation between the gaseous amine molecules and the atoms at the surface of the semiconducting crystal. In 2003, Nazzal *et al.* investigated the use of discrete hexadecylamine-capped CdSe nanoparticles embedded in a polymer matrix as gas sensors.²² In their work, a photoirradiation procedure was employed to activate the nanoparticle surfaces before and during exposure to different gases. Using single-particle fluorescence measurements, they found increased PL intensity when the sample was exposed to triethylamine (TEA), while a decrease in PL intensity was observed when the analyte was benzylamine. Recently, the concept of optical sensing with metal chalcogenide nanocrystals was exploited in bio-nanosensors where nanocrystals (i.e. CdSe or CdSe/ZnS) function as fluorescence resonance energy transfer (FRET) donors transferring energy to an organic acceptors (i.e. dye).²³⁻²⁶

Compared to the Cd materials, PbE (E = S, Se, Te) nanocrystals have a narrow band gap in the near-infrared region, and these are sometimes referred to as infrared quantum dots. Based on this characteristic, PbE nanocrystals are also finding application in whole-body imaging.²⁷ The advantage of using infrared quantum dots for optical imaging is due to their long wavelength, which allows them to be imaged in deep organs where cadmium based nanocrystals can not be detected due to the limited penetration depth of visible light.²⁷

1.3 Synthesis Methods for Metal Chalcogenide Nanocrystals

Both physical and chemical methods have been employed to prepare semiconductor nanocrystals. The physical processes require high energy input to achieve the formation of nanoparticles²⁸ by molecular-beam-epitaxy (MBE) and metal-organic-chemical-vapor-deposition (MOCVD); or nanowires²⁹ by vapor-liquid-solid (VLS) growth. On the other

hand, colloidal chemical synthesis needs only a low energy input to build nanocrystals from the molecular level, and does not require any special equipment. For these reasons, colloidal chemical synthesis represents the most widely used method to prepare semiconducting nanocrystals. With respect to phases of direct relevance to the dissertation work, group II-VI and IV-VI metal chalcogenide nanocrystals have been successfully prepared by arrested precipitation methods (room temperature synthesis) and molecular precursor method (high temperature synthesis), as discussed more fully below.

1.3.1 Formation of Metal Chalcogenide Nanocrystals by the Arrested Precipitation Method

Arrested precipitation reactions performed in inverse micelles (AOT/H₂O/heptane solution, AOT=di(2-ethylhexyl)sulfosuccinate sodium salt) have been successfully conducted to produce CdS, CdSe, CdTe, ZnS and HgSe nanocrystals, among others.^{30, 31} The method involves kinetically controlled nucleation of metal chalcogenides by mixing separate inverse micelle solutions of metal ions and chalcogenide ions. The inverse micelle solutions are prepared by dispersion of a small amount of dilute aqueous metal ions (or chalcogenide ions) into a large amount of non polar solvent (e.g. hexane) along with surfactant (e.g. AOT).^{32, 33} Upon mixing the two solutions, the micellar contents are dynamically exchanged, precipitating metal chalcogenide within the inverse micellar envelope. The size of the prepared nanocrystals is controlled by the molar ratio of surfactant to water.^{31, 33} The nanocrystal surface is subject to further modification by exchanging with other organic ligands to facilitate the isolation and subsequent processing. Nanocrystals prepared by this method are usually poorly crystalline due to defect formation during room temperature

synthesis (insufficient energy to anneal out the defects). As a consequence, the photoluminescence properties of these nanomaterials often suffer from the defective structure and band-edge emission is usually buried beneath a broad and intense trap-state emission band.^{31, 34}

1.3.2 Formation of Metal Chalcogenide Nanocrystals by the Molecular Precursor Method

The molecular precursor method has been applied to the synthesis of a variety of metal chalcogenide nanocrystals.^{1, 3} The method is based on pyrolysis of metal-organic complex precursors in hot coordinating solvents (150-360 °C); the high temperature can effectively anneal defects out of the nanocrystal. Thus, the resultant nanocrystals are highly crystalline and exhibit sharp band-edge emission. According to the classic study by La Mer and Dinegar,³⁵ a typical high temperature synthesis involves two distinguishing events: a single and short nucleation event at elevated temperatures (>300 °C) followed by slower controlled growth of the existing nuclei at a reduced temperature (150~250 °C).^{9, 35} The formation of nuclei can be achieved by rapid injection of a precursor (e.g. chalcogenide precursor) into a hot coordinating solvent that contains the other thermally decomposed precursor reagent (e.g. metal precursor). The action results in a sudden increase of precursor concentration beyond the nucleation threshold and leads to nuclei formation.⁹ As long as the consumption rate of precursor by deposition onto the growing nanocrystals is higher than the addition rate of precursor decomposed from the reagent in solution, no further nucleation will occur and the existing nanocrystals will grow into bigger particles. An alternative approach to trigger the nucleation event is by pre-mixing the reaction reagents with the coordinating solvent at low

temperature and ramping up the temperature to a level that causes quick decomposition of precursor reagents into molecular precursors and a subsequent nucleation burst.³ Then the temperature is maintained at a level that is high enough for the existing nuclei to grow into bigger particles and low enough to avoid additional nuclei forming.

Several important parameters govern the quality of the prepared nanocrystals in terms of size and shape monodispersity. As the above description of the synthesis procedure shows, time and temperature are critical to control the size of the nanocrystals. Generally, a longer reaction time produces a larger average particle size. Temperature plays a contrasting role in nucleation and growth steps. Nuclei size decreases with increasing nucleation temperature, whereas particle size increases with increasing growth temperature. Precursor concentration can influence the reaction but the effect depends strongly on the characteristics of the surfactant/coordinating solvent.

The coordinating solvents not only function as reaction media, they also coordinate to the nanocrystal surface along with any added surfactants to passivate the nanocrystal surface sites and prevent the nanocrystals from aggregating and flocculating.³ In many cases, the coordinating solvent itself is the surfactant. Common coordinating solvents include alkyl phosphines, alkyl phosphine oxides, alkylamines, alkylphosphates, alkylphosphites, alkylphosphonic acids, as well as fatty acids and alkylthiols, and these vary with respect to length of alkyl chain and degree of chain branching.³ The polar head group binds to the nanocrystal surface and the non-polar carbon chain tail points out to the solvent. This arrangement of the surfactants allows the nanocrystals to be dispersed in many common non-polar organic solvents. Depending on how strongly the coordinating groups binds to the nanocrystal surface and how bulky the groups are, different sizes of nanocrystals can be

produced. Strongly binding and bulkier groups tend to yield smaller particles. A high ratio of precursor concentration to surfactants (coordinating solvents) facilitates larger particle preparation.³ Additionally, anisotropic shaped nanocrystals (rods, wires, tetrapods and so forth) can be produced by increasing precursor concentrations, the solubility of which is facilitated by strong coordinating groups, as anisotropic growth of nanocrystals is favored at high precursor concentrations.³⁶

1.3.3 Synthesis of CdSe and CdTe Nanocrystals

Since CdSe and CdTe nanocrystals are of particular interest in this dissertation research, their various synthesis methods will be discussed in detail in this section. As mentioned in Section 1.3.2, CdSe and CdTe nanocrystals have been prepared by both the inverse micelle method and molecular precursor method, but recently the focus has been on the latter method. A pioneering study was reported by Murray *et al.*⁸ in which CdE (E = S, Se, Te) nanocrystals were synthesized by using dimethylcadmium ($\text{Cd}(\text{CH}_3)_2$) as the cadmium precursor, trioctylphosphine (TOP) chalcogenide as the chalcogenide precursor, and trioctylphosphine oxide (TOPO) as the coordinating solvent. The resultant nanocrystals were highly crystalline and had a narrow size distribution. This synthesis has been further developed by several groups. Peng *et al.*³⁷ studied the kinetics of the CdSe synthesis and found that monodisperses nanocrystal growth needs continuous monitoring and adjustment of the monomer concentration to keep the growth within “size focusing regime”. Talapin *et al.*³⁸ reported greatly enhanced photoluminescence (QY~65 %) of CdTe nanocrystals by using dodecylamine (DDA) as the stabilizer, which is a good Lewis base functioning as electron donor. However, all of these methods employed $\text{Cd}(\text{CH}_3)_2$ as the Cd precursor, which is

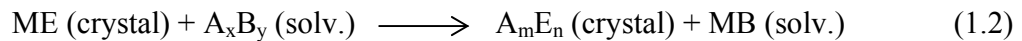
extremely toxic and pyrophoric, and thus limited the practicality of the synthesis method. This drawback motivated Peng *et al.* to modify the synthesis by using a mild reaction reagent CdO as the Cd precursor and adding hexylphosphonic acid (HPA) or tetradecylphosphonic acid (TDPA) as surfactant.¹⁰ The quality of the nanocrystals produced by the CdO approach is comparable to those produced by Cd(CH₃)₂. Other less hazardous cadmium sources, such as (CH₃COO)₂Cd and Cd myristate salts have also been employed for preparation of CdSe and CdTe nanocrystals.^{11, 39, 40} Additionally, the combination of cadmium salts with anions of a fatty acid, such as stearic acid and lauric acid, produces larger nanocrystals (>4 nm in diameter),¹¹ where the growth step is more favorable in comparison with the TOPO-TOP system. Alkyl amines with different chain length and branching (oleylamine, hexadecylamine, diocylamine) have been used as surfactants to produce highly luminescent quantum dots owing to electron donor properties of the Lewis basic amines.

In addition to the high temperature synthesis, room temperature aqueous method can be applied to CdSe and CdTe nanocrystals synthesis. In a typical CdTe nanocrystal synthesis, Cd(ClO₄)₂ is dissolved in water and a thiol stabilizer is added to the system, followed by the adjustment of pH to basic conditions (>11). After the system is deaerated, H₂Te gas is passed through the reaction solution, leading to nucleation of CdTe. Growth is allowed to proceed over several days. Generally, nanocrystals prepared by this aqueous method exhibit relatively broad size distribution (>20%). Therefore, subsequent size selective precipitation is often necessary to separate out the different sizes of nanocrystals. However, a rough tuning of the initial particle size can be achieved by changing the identity of the thiolate capping groups. It has been reported that thiolate ligands attach to the metal ions before nucleation takes place.³ Therefore, the strength of the bond between the metal and the specific thiolate stabilizer

directly affects the nucleation speed: when the bond is strong, slow nucleation will occur, leading to the generation of smaller particles and vice versa.³ In the literature, CdTe nanocrystals have been synthesized using a variety of thiols, such as thioglycolic acid (TGA),⁴¹ 1-thioglycerol,⁴² mercaptoethylamine,⁴² L-cystein⁴² and mercaptopropionic acid.⁴³

1.3.4 Cation-Exchange Reactions of Metal Chalcogenide Nanocrystals

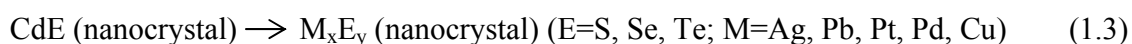
Cation-exchange reactions are a class of reactions that involves exchange of a metal cation in one compound by a mobile metal cation in solution.⁴⁴ For a cation-exchange reaction in II-VI crystals, the reaction can be generally described by



where M = Zn, Cd; E = S, Se, Te; A = a metal; B = NO₃⁻, Cl⁻ or other anions; x, y, m and n values are decided by the oxidation states of the metals and anions. Theoretically, in order to carry out the reaction, the standard molar Gibbs energy (ΔG^0) of the reaction should have a negative sign. In other words, the solubility product constants (K_{sp}) of the product (A_mE_n) should be lower than that of the reactant (ME). Additionally, the cations should have high diffusion coefficients to ensure a reasonable reaction rate.⁴⁴

However, many thermodynamically favored reactions with mobile metal ions involved are still resistant to ion-exchange under ambient conditions because of the high activation energy required for the diffusion of ions in and out through the solid lattice framework. Studies have shown that the activation barrier dramatically decreases as particle size decreases.⁴⁵ Based on this, various new compositions of thin films and nanoparticles have been prepared via cation exchange reactions. For example, ZnS thin films were

converted to Ag_2S , Cu_2S , Bi_2S_3 , and Sb_2S_3 films by simply treating them with solutions containing Ag^+ , Cu^+ , Bi^{3+} , or Sb^{3+} ions, respectively.^{46, 47} The transformation of binary metal chalcogenide nanocrystals has been demonstrated by treatment of CdE with appropriate ions as shown in Equation 1.3.^{48, 49}



Xia *et al.*⁵⁰ reported a versatile route to prepare core-shell structure of Se@MSe ($\text{M} = \text{Zn, Cd, Pb}$) via cation exchange of $\text{Se@Ag}_2\text{Se}$ with Zn^{2+} , Cd^{2+} and Pb^{2+} . Overall, cation-exchange reactions in nanocrystals provide new and complementary synthetic route to a variety of nanocrystals.

1.4 Nanocrystal Assembly Methods

Recent advances in the preparation of semiconductor nanocrystals with control of accurate size,^{8, 51} shape^{52, 53} and structure have triggered a secondary stage of extensive research focused on bottom-up assembly of nanocrystals into functional solid-state materials. Many new assembly methods have been developed for construction of one-dimensional (1D), two-dimensional (2D) and three-dimensional (3D) structures (Figure 1.3) Generally, 1D assemblies of nanocrystals lead to the formation of nanowires⁵⁴ and nanochains,⁵⁵ 2D assemblies generate nanosheets^{56, 57} and monolayer films,⁵⁸ and 3D assemblies of nanocrystals result in macroscopic superstructures, such as colloidal crystal superlattices. Since 3D assemblies of nanocrystals are of particularly relevance to the dissertation research, they will be the focus of this section.

In principle, 3D bottom-up assemblies can be achieved via many methods, with or

without templates. Among them, the layer by layer assembly method and the self-organization of close-packed nanocrystals method represent two common approaches that are used.

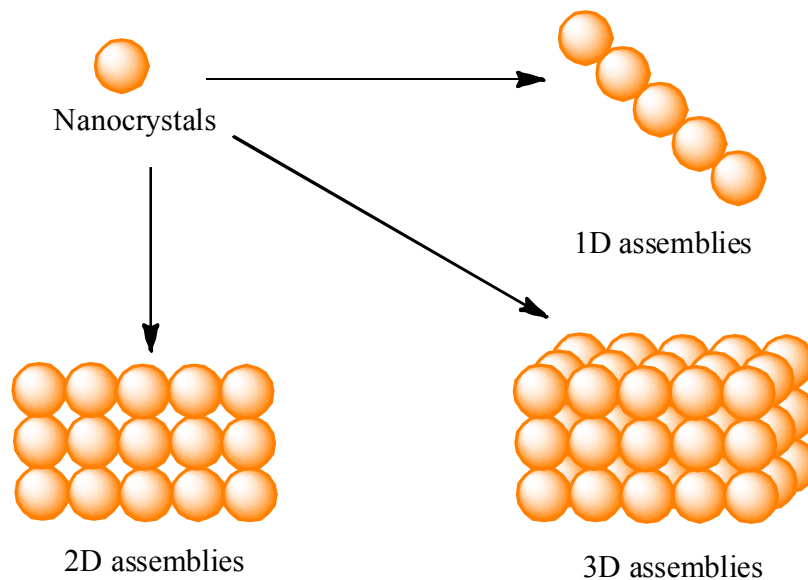


Figure 1.3 Schematic illustrations of 1D, 2D and 3D assemblies of nanocrystals.

1.4.1 Layer by Layer Assembly (LBL) Method

The LBL method is typically conducted by alternative deposition of charged nanoparticle layers with oppositely charged polyelectrolyte (PE) layers. The multilayer assembly is driven by the electrostatic force between the nanoparticle layers and the PE layers. Varying the nanoparticle components of one of the layers leads to unlimited but controllable multi-composition LBL assembly.⁵⁹ While the method is simple and flexible, the least distance between two nanoparticle layers can not be shorter than the thickness of the PE monolayer (on the order of several angstroms); thus, efficient inter-layer interactions are

limited by the characteristics of the PE layer. Later studies⁶⁰ have shown this limitation can be overcome by using CdTe nanocrystals prepared with opposite charges as building blocks (i.e. without PE layers) where the charge of the nanocrystal surface is governed by the stabilizer coated on the surface. The distance between two nanoparticle layers in this case is equal to the thickness of stabilizer coating at the interface of the two nanoparticle layers. However, the stability of the assembled structure is low due to the easy removal of the deposited layers resulting from unbalanced surface charges during the process of film growth.

1.4.2 Self-Organization of Close-Packed Nanocrystals

Self-organization of close-packed nanocrystals is conducted by slow solvent evaporation of colloidal nanocrystal solutions. Depending on the composition of the solvent, locally-ordered colloid glasses or long-range ordered superlattice structures can be created. During glassy film formation, the solvent composition is tailored to maintain the stabilization of the colloidal solution; slow solvent evaporation leads to random close-packing of nanocrystals. In contrast, for superlattice crystallization, a high boiling point alcohol (non-solvent) is added to the colloidal nanocrystal non-polar solution to induce destabilization of the colloidal solution. When the solvent evaporates, nanocrystals transit from the dispersion to an aggregation state. The transition is controlled slowly enough to let nanocrystals have time to find the equilibrium superlattice sites, eventually leading to a 3D long-range structure. The superlattice approach has been extensively employed to grow a variety of superlattices including metals (Co, Au, Ag, Pt),⁶¹⁻⁶³ semiconductors (CdSe,⁶⁴ Ag₂S, InP,⁶⁵ PbS, PbSe, PbTe), magnetic nanocrystals and some binary mixtures (PbSe/Fe₂O₃)⁶⁶.

While the method is applicable to many nanocrystals, nanocrystals in the assembled structures remain separated from each other by the organic capping ligands, similar to the case of LBL assembly. Therefore, direct interaction between nanocrystals is limited by the surface groups. Consequently, from the perspective of electronic device performance, the superlattice structure may have limited electron-transport capability.

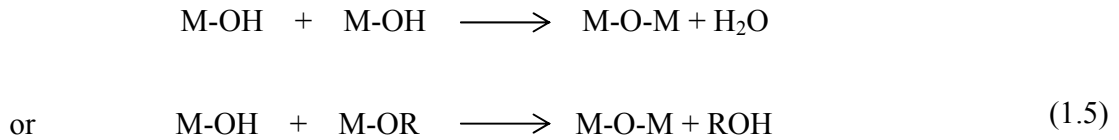
1.5 Sol-Gel Assembly Method

In contrast to the above described methods for generation of 3-D nanoparticle assemblies, the sol-gel method results in nanocrystal networks without a secondary phase to moderate particle-particle interactions (e.g. polyelectrolytes or organic capping groups at the particle-particle interfaces). The sol-gel method has been traditionally focused on the synthesis of metal oxide gels. A typical sol-gel process involves a two-step inorganic polymerization of metal alkoxide precursors ($M(OR)_n$): hydrolysis and condensation.⁶⁷ In the first step, the alkoxy ligands of $M(OR)_n$ precursors are hydrolyzed into an alcohol and hydroxylated metal centers ($M-OH$) are formed as new reactants for the subsequent reaction (Equation 1.4). In the condensation step, the $M-OH$ species propagate in 3D to react with each other, by eliminating either water or alcohol (Equation 1.5). A series of condensation reactions initially produces small oligomers interconnected by $M-O-M$ bonds. Upon aging, these oligomers further aggregate to form the wet gel.

(1) Hydrolysis



(2) Condensation



For the most common example of silica, the morphology of the resultant gel depends on the reaction pH.⁶⁸ Under acidic conditions (pH 2-5), hydrolysis is favored and the condensation reaction is the rate-determining step. A large number of oligomers is formed simultaneously, resulting in polymer-like gels with few branches and small pores. When the reaction is conducted under basic conditions, hydrolysis is the rate-determining step; the condensation of monomers or small oligomers is favored, leading to gels composed from nanoparticles with large pores. In both cases, the nanoparticles or oligomers are directly connected to their neighbors. without intervening ligands.

1.6 Wet Gel Drying Methods

A dry material can be obtained by extraction of pore solvent from a wet gel. Depending on the desired properties, different gel drying methods are used (Figure 1.4). When the wet gel is dried from the mother liquid (a surface wetting solvent, such as water or alcohol in the case of silica) under ambient condition, the capillary forces at the liquid-vapor interface result in the collapse of the pore structure as the pore solvent evaporates, leading to xerogel formation, a relatively dense dried gel with a deformed gel structure.

On the other hand, when the gel is dried from a supercritical fluid, there are no liquid-vapor interfaces existing in the pores; thus the porosity of the wet gel can be preserved during removal of pore solvent and the structure of the wet gel network is largely maintained, producing an aerogel. The process results in the production of aerogels with pores filled with

air.

Based on the solvent that is used for drying, supercritical fluid drying (SFD) can be placed into two categories: hot and cold SFD.⁶⁸ Hot SFD is performed in organic solvents (alcohol or acetone) and generally requires high temperature and pressure to bring the solvent to the supercritical state. For example, ethanol needs ~ 250 °C and 5~8 MPa to be supercritical.⁶⁷ The potential risk of explosion associated with the high temperatures and high pressures raise safety concern and limit the practicality of the method. Additionally, high temperatures can result in rearrangement reactions, damage to functional organic groups, phase separation and loss of stoichiometry during drying. Consequently, the resultant aerogels may exhibit low surface area and narrow pore size distributions. In contrast to hot SFD, cold SFD, introduced by Tewari *et al.*,⁶⁹ uses liquid CO₂ as the solvent. The advantage of using liquid CO₂ is the low temperature (30-40 °C) at which CO₂ becomes supercritical phase ($P \sim 8$ MPa). However, liquid CO₂ is not very miscible with most common solvents, so a time-consuming solvent exchange step in which the original pore solvent is exchanged with a more liquid CO₂ miscible solvent is performed prior to cold SFD.

An alternative way to dry that produces materials with porosity intermediate between aerogel and xerogels is to dry the wet gel at ambient pressure from pore solvents with low surface tension (i.e. non surface-wetting solvents). This method has been extended from silica to other compositions, such as V₂O₅ and MoO₂.⁷⁰ The resultant materials, referred to ambigels, have comparable surface areas and pore volumes compared to the correspondent aerogels dried by SFD method. As this dissertation is focused largely on aerogels, these materials will be discussed more fully in the following sections.

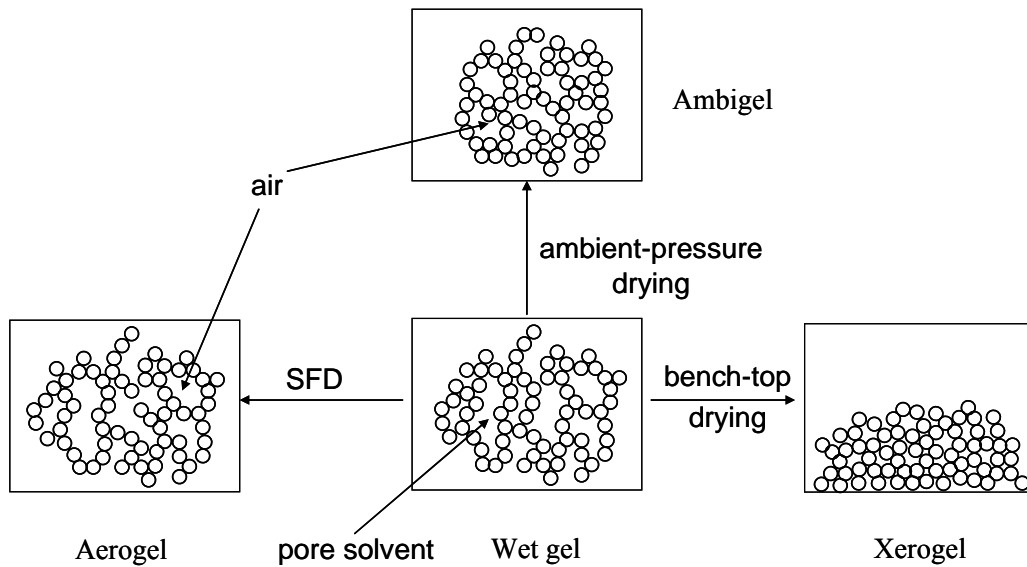


Figure 1.4 Schematic illustration of drying methods for generation of aerogels, ambigels and xerogels from wet gels.

1.7 Physical Properties and Applications of Aerogels

Aerogels consist of a highly porous network which is composed of connected nanoscale building blocks. They have many interesting physical properties including large inner surface areas, high porosities (both micropores (<2 nm) and mesopores (2~50 nm)), low densities, low thermal conductivity ($0.020 \text{ Wm}^{-1}\text{K}^{-1}$ in air), optical transparency, low sound velocity, low refractive index (1.007 to 1.024), and low dielectric constant (<2), where the numbers listed are corresponding to SiO_2 aerogels. These unique structural, optical, thermal and acoustic properties have made aerogels great candidates for many potential and actual applications, such as sensors,⁷¹ catalysts,⁷² catalyst supports,⁷³ thermal insulators,⁷⁴ batteries,⁶⁸ interlayer dielectrics,⁶⁷ nuclear waste storage,⁷⁵ and applications in life science,

such as encapsulation of active enzymes⁷⁶ and biosensors.⁷⁷ Sensing applications of aerogels are directly relevant to the dissertation, and are discussed more fully in the following section.

1.8 Previous Studies on Sensing Applications of Aerogels

In principle, sensing methods are based on the interactions of surface atoms of the sensing material with analytes.⁷⁸ If the adsorption of the analyte changes the properties of the material, and this can be recorded, it can act as a sensing platform. A good sensor material should have high sensitivity (large and rapid response) towards the adsorption of an analyte; secondly, the sensor should be mechanically and chemically stable in the operating environment. Further, the sensor should be designed to have high specificity and affinity to the analyte of interest, while showing no or an unrelated response to other components coexisting with the analytes.

Aerogels are good candidates as sensor materials because of their high surface areas and large open porous structures. The former exposes a large number of reactive sites on the surface to analyte molecules. The latter provides good accessibility for analyte molecules to the responsive nanoscale domains because the diffusion rate through the mesoporous aerogel framework is only slightly lower (10x) than that in open air.⁷⁹ Among all types of aerogels, silica based systems are the most widely studied for sensing applications because of their high optical transparency, good mechanical and chemical stability, ability to incorporate additional active phases and the permeability of the gel network to small analyte molecules. In particular, silica aerogel sensors based on collisional luminescence quenching by molecular oxygen have received significant attention.^{71, 80, 81} In these oxygen sensors, fluorophores (e.g. dyes) generally function as the luminescence indicator, and these are

covalently attached, or physically entrapped within, the silica aerogel. Ayer and co-workers⁸² have reported an alternative way to make silica aerogels intrinsically luminescent by treatment with 2.45 GHz radiation under a reducing atmosphere (NH₃ or H₂). The fluorophores in this case are defect centers throughout the SiO₂ lattice created by the radiation treatment. No matter what the fluorophore is, the quenching mechanisms are similar. When incident light has been absorbed, the fluorophore is excited to the excited state. If the fluorophore directly relaxes to the ground state, the excess energy is emitted as photoluminescence. However, when collisional quenching takes place, oxygen, a known efficient quencher,⁸³ collides with the fluorophore, and the excited fluorophore transfers its excess energy via non-radiative relaxation. Therefore, this quenching process causes a decrease in photoluminescence intensity. The efficiency of the quenching is determined by the frequency of collisions happening between the fluorophore and oxygen molecules, which can be calculated by the Stern-Volmer equation,

$$I_0/I = 1 + K_{SV}[Q] \quad (1.6)$$

where I_0 is emission in the absence of quencher; I = emission intensity in the presence of quencher; $[Q]$ = concentration of quencher; and K_{SV} = Stern-Volmer equilibrium constant. A Stern-Volmer plot, I_0/I vs. $[Q]$, is linear if only one quencher is present, whereas a non-linear Stern-Volmer plot indicates different quenchers are present in the sensing environment.⁸³

In addition to oxygen aerogel sensors, Rolison *et al.*⁸⁴ have studied NO sensing by incorporation of active enzymes into silica aerogels. In this study, cytochrome c protein superstructures were self-organized around gold nanoparticles and encapsulated into silica aerogels. The biocomposite silica aerogels exhibited a clear shift in the Soret band (visible

absorption at 409 nm) when the embedded enzyme was exposed to NO. Sensing experiments were conducted by monitoring the kinetic Soret band intensity change when switching gas flow between NO and argon.

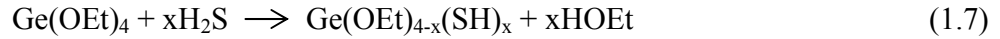
1.9 Types of Aerogels

SiO₂ aerogels have been extensively studied and are the best investigated system among aerogels. They date back to Kistler's first report of a SiO₂ aerogel in 1930's.⁸⁵ In principle, the sol-gel synthesis strategy used for SiO₂ gels can be extended to form other metal oxide gels. However, many metal alkoxide precursors have higher reactivities toward water than Si(OR)₄, resulting in precipitation rather than gelation. By substitution of part of the alkoxy group by a chelating or bridging ligand, the reactivity of a metal alkoxide precursor can be modified, enabling a wide variety of aerogels to be prepared, including Al₂O₃, TiO₂, ZrO₂, SnO₂, V₂O₅, Cr₂O₃, Fe₂O₃, MoO₂ and Nb₂O₅ aerogels.⁶⁷ Based on the development of single component aerogels, multicomponent metal oxide aerogels can be prepared by assembly of precursors with similar hydrolysis and condensation rates. Typical binary or ternary systems include TiO₂/SiO₂, Al₂O₃/SiO₂, 3Al₂O₃/2SiO₂, Fe₂O₃/SiO₂, Fe₂O₃/Al₂O₃, V₂O₅/MgO, PbO/ZrO₂, BaO/Al₂O₃, PbTiO₃, NiO/Al₂O₃/MgO, and 2MgO/2Al₂O₃/5SiO₂.⁶⁸ Because the high porosity of aerogels makes them very suitable for catalysis, considerable attention has been focused on formation of active metal-containing aerogels, beginning with Pt/SiO₂ and Ni/SiO₂,⁸⁶ and extending to Cu/SiO₂, Pt/MoO₂, Pt/Al₂O₃, Pt/TiO₂, V/SiO₂, Pd/Al₂O₃, and Pd/CeO₂.⁶⁸ In all cases, the frameworks have been oxide-based. Only in the last two decades has there been focus on non-oxide systems, such as carbon aerogels, which were first reported by Polanski in 1994.⁸⁷

In 2004, the Brock group reported the first synthesis of metal chalcogenide aerogels.^{31, 88} The resultant materials have highly porous three dimensional solid networks while retaining the inherent properties of the semiconducting quantum-confined building blocks. These materials are described more fully in the next section.

1.10 Previous Studies on Metal Chalcogenide Gels and Aerogels

The first syntheses of metal chalcogenide gels were performed by traditional sol-gel processes. The thiolyses process is similar to the hydrolysis process employed in metal oxide gel preparation, but H₂S is used as the sulfur source and metal alkoxides or amides as the metal precursors. For example, GeS₂ gels can be obtained by a series of thiolysis and condensation reactions of Ge(OEt)₄ with H₂S, as shown in Equation (1.7) and (1.8).



A number of metal sulfide gels (La₂S₃,⁸⁹ TiS₂,⁹⁰ NbS₂,⁹¹ MoS₂,⁹² WS₃,⁹² Re₂S₇,⁹² NiS,⁹²) have been prepared via thiolysis sol-gel routes. However, most of the gels exhibit poor building block crystallinity or dense morphologies.

Alternatively, Gacoin and co-workers^{32, 93, 94} have reported a two-step synthesis strategy for CdS gel preparation. In this approach, primary CdS nanoparticles were first synthesized from Cd(NO₃)₂ and H₂S by use of an inverse micelle method followed by surface exchanging with 4-fluorophenylthiolate (FPhSH). In the second step, the thiolate complexed CdS nanoparticles were treated with H₂O₂, which caused oxidative loss of surface thiolate

groups on the nanoparticles and ultimately led to gel network formation. The ratio of H_2O_2 to FPhSH ($X = [\text{H}_2\text{O}_2 / \text{FPhSH}]$) is critical in terms of control of the gelation process. The value of X should be less than 0.5 but great than 0.2 to ensure a progressive gelation process rather than forming a precipitate ($X > 0.5$) or failing to depassivate sufficiently to induce a gel ($X < 0.2$). An advantage of this two-step strategy is that the separation of the nanoparticle formation step from the condensation step ensures formation of colloidal gel.

In 2004, Mohanan *et al.*⁸⁸ reported the first synthesis of a metal sulfide aerogel, CdS, by using the two-step sol-gel strategy followed by supercritical CO_2 drying. This synthesis approach was later shown to be generally applicable to the assembly of other metal chalcogenide nanoparticles into aerogel structures: PbS, ZnS and CdSe.³¹ The resultant aerogels retain 90-95 % of the wet gel volume and exhibit the characteristic base-catalyzed silica aerogel morphology, consisting of a three dimensional highly porous solid network composed of interconnected nanoparticles. Although the prepared aerogels are assembled three dimensional networks, no significant shift of optical absorption peak was observed for the aerogels relative to their nanoparticle counterparts, indicating the quantum confined optical properties of the building blocks are retained in the assembly. The chalcogenide aerogels have high BET surface areas (119-250 m^2/g), comparable to traditional silica aerogels when the values are converted to silica equivalent BET surface areas (476-600 m^2/g). However, the original metal chalcogenide aerogels were found to be poorly luminescent due to partial quenching of the band-edge emission by defect structures in room temperature synthesized nanoparticles. Subsequently, Arachchige *et al.* discovered that aerogels from CdSe nanocrystals prepared via elevated temperature synthesis routes have significantly enhanced band-edge emission.³⁴ Moreover, the PL could be augmented still further by

coating a thin layer of ZnS shell onto the primary CdSe nanoparticle core prior to gelation.⁹⁵ By varying the primary particle size, yellow-green to red emitting CdSe/ZnS aerogels can be obtained.

The gelation mechanism for the assembly of thiolate (11-mercaptoundecanoic acid) capped metal chalcogenide nanoparticles (CdSe, CdS and ZnS) has been proposed by Brock and co-workers very recently.⁹⁶ Briefly, the study proposed that during gelation, the thiolate ligands are either chemically- or photo-oxidized to produce disulfide species, thereby exposing the nanoparticle surface. The decomplexed Cd²⁺ ions were then solvated, leaving a chalcogenide rich particle surface. By further oxidation, the E²⁻ (E=S, Se) ions were oxidized into E⁻ fragments, which can link the particles together to form a gel network supported by (E₂)²⁻ or (E_n)²⁻ fragments. The polychalcogenide bonding in the aerogels was confirmed by Raman and X-ray photoelectron spectroscopies.⁹⁶ Consistent with the redox mediated gelation, the resultant gels can be redispersed by addition of reducing agents (e.g. thiol).

1.11 Previous Studies on the Assembly of CdTe Nanocrystals

Among cadmium chalcogenide nanocrystals, CdTe nanocrystals have received considerable attention due to their size-dependant emission properties, spanning from the UV through the near IR, as well as their large window for absorbance ($\lambda < 825$ nm based on a bulk band gap of 1.5 eV) and high extinction coefficient ($> 1 \times 10^5$ cm⁻¹M⁻¹).⁹⁷ These factors, combined with the documented synthetic methods for obtaining high-quality CdTe nanocrystals with control of size,^{8, 12, 97} shape^{12, 98} and surface chemistry^{99, 100} have made them promising materials for many applications, such as light emitting diodes (LED),¹⁰¹⁻¹⁰³ photovoltaic devices,^{104, 105} and sensors.^{106, 107} However, applications that rely on electrically

connected systems require the discrete nanocrystals accessible by solution phase strategies to be assembled into superstructures while retaining the inherent properties of the primary nanocrystals. Furthermore, for certain applications (e.g. sensing and photocatalysis), the assembled nanostructures should be open and accessible to small molecules to facilitate access to the reactive nanocrystal surface.

A few studies have been performed on the assembly of CdTe nanocrystals. Kotov *et al.* reported self-assembly of thiolate stabilized CdTe nanocrystals into 1D nanowires⁵⁴ or 2D sheets⁵⁶ via partial depletion of thiolate stabilizers by washing with methanol. In contrast to the oxidization induced gelation process employed by the Brock group, the assembly was reported to occur in the absence of an external oxidant and in the dark. Later, Gaponik and Eychmüller demonstrated 3D assembly of thioglycolic acid (TGA)-capped CdTe nanocrystals into gels and aerogels.¹⁰⁸ They used aging, chemical oxidation and photochemical methods to induce gelation and produced the aerogel by supercritical drying. The CdTe gels and aerogels were found to exhibit the classic pearl-necklace architecture and were highly luminescent. However, other physical properties (e.g. surface area, crystal phase and elemental composition) were not evaluated. More recently, Eychmüller and co-workers reported 3D assembled nanostructures containing piled up CdTe@Cd-TGA complex nanowires.¹⁰⁹ Without employing an oxidative process, the assembly was achieved by partial removal of TGA capping groups in the presence of ethanol and a high concentration of salt. The CdTe nanocrystals are essentially embedded in the Cd-TGA gel matrix.

1.12 Thesis Statement

The dissertation study is focused on synthesis, characterization and applications of

metal chalcogenide aerogels. The specific goals are to (1) explore the suitability of the sol-gel synthetic method developed for sulfides and selenides for high surface area tellurides (CdTe) and evaluate the validity of the proposed gelation mechanism for CdSe assembly for these systems; (2) study cation-exchange reactions of primary metal chalcogenide gels as a route to the synthesis of new compositions of aerogels; (3) investigate the suitability of CdSe aerogels as optical sensors for Lewis bases and study the sensitivity of the luminescence property of the aerogel to the change of surface characteristics and determine the accessibility of the metal chalcogenide aerogels to small molecules.

1.12.1 Porous CdTe Nanocrystal Assemblies: Ligation Effects on the Gelation Process and the Properties of Resultant Aerogels (Chapter 3)

As mentioned in Section 1.11, direct assembly of CdTe nanocrystals is highly motivated by the potential value of CdTe networks for many interesting applications. Previous studies from the Brock group have demonstrated the general applicability of the two-step sol gel synthetic strategy for metal sulfides and selenides.^{31, 110} Moreover, the recent gelation mechanism study by Brock and co-workers⁹⁶ suggests that the gelation of nanoparticles is due to the chemical oxidation or photo-oxidation of the particle surface and subsequent formation of interparticle bonding between surface chalcogenide species. Therefore, this oxidative gelation approach is expected to be applicable to the assembly of CdTe nanocrystals, because tellurides are more easily oxidized than sulfides or selenides. Hence, this part of the dissertation research explores the synthesis of CdTe gels and aerogels by our previously developed method and compares these materials to related aerogels reported by Eychmüller and co-workers.¹⁰⁸ Additionally, we evaluate the assembly of CdTe

nanocrystals without thiolate exchange as an intermediate step, thereby testing a hypothesis drawn from the mechanism study, that thiolate capping groups are not necessary for gelation.

1.12.2 Cation Exchange Reactions in Metal Chalcogenide Aerogels: Ag₂Se, PbSe and CuSe Gels and Aerogels (Chapter 4)

Sol-gel assembly of nanoparticles has been shown to be a powerful tool for the preparation of metal chalcogenide aerogels in previous studies.^{31, 34, 88, 95, 111} However, the chemistry is limited to nanoparticles with established syntheses and to compositions that are robust to gelation conditions. To expand the repertoire of chemistries that can be accessed within the aerogel framework, alternative synthetic methods are desired. As we discussed in Section 1.3.4, cation exchange reactions have been demonstrated as useful and simple methods for preparing new compositions of thin films and nanoparticles without having to assemble the new nanostructures from the bottom-up.^{48, 49, 112} Importantly, this approach is not limited to discrete nanoparticles; liquid crystal templated mesostructures can also be transformed and without losing their mesoscale order.¹¹³ Because metal chalcogenide gels are formed from nanoscale building blocks, we surmised that a kinetically rapid mechanism of cation exchange would take place in the gel system as well. This would enable efficient production of new aerogel compositions without the need to synthesize each individual nanoparticle phase or figure out the vagaries of synthesis and ligand modification of different building blocks, as well as optimal gelation conditions for rendering monoliths with minimal surface oxidation. Therefore, in this part of the dissertation study, we explore a new synthesis method for generating new composition of metal chalcogenide aerogels: cation exchange reactions of primary CdSe wet gels.

1.12.3 Optical Sensing of Triethylamine Using CdSe Aerogels (Chapter 5)

Traditional silica aerogels have demonstrated excellent potential for applications in sensing, however, optical sensing based on photoluminescence (PL) typically requires introduction of a secondary phase as a fluorescence indicator into the silica framework.^{114, 115} Semiconducting metal chalcogenide aerogels (CdS, CdSe, PbS, ZnS) retain the quantum confined properties of their discrete nanoparticulate building blocks.^{31, 34, 111, 116, 117} They have a similar band gap energy (E_g) to the precursor nanoparticles, lying in the UV/visible to near-IR part of the spectrum, and are intrinsically luminescent.^{31, 34, 111, 116, 117} Therefore, sensing can be potentially achieved with intrinsic metal chalcogenide aerogels without necessitating the introduction of an extrinsic phase (fluorophore), as is the case with silica.

As discussed in Section 1.2, CdSe has been previously used for sensing of Lewis bases as single crystals by Meyer *et al.*²¹ and as nanoparticle-polymer composites by Nazzal *et al.*²² The operative mechanism is a PL enhancement resulting from acid-base adduct formation between the gaseous amine molecules and the atoms at the surface of the semiconducting crystal. Accordingly, in analogy to what has been observed in single crystals and discrete nanoparticles, we hypothesized that the Lewis acidic characteristics of the metal chalcogenide aerogels would allow adduct formation to take place between the aerogel surface and Lewis basic analyte molecules, changing the surface electronic structure of the aerogel and therefore leading to a change in the PL. Our prior studies have shown that quantum confinement effects intrinsic to the nanoparticle building blocks can be largely retained in the low-dimensional aerogel network, and that the native PL properties, particularly the intensity of the band edge emission, can be altered by varying the surface groups on the aerogel.^{31, 34, 116} Additionally, the porous structure and the high surface atom to

interior atom ratio of aerogels allows good accessibility of gaseous molecular analytes and maximizes the available binding sites on the nanoscale domains. Hence, in the last part of the dissertation study, we have investigated the photoluminescence sensing properties of CdSe aerogels to triethylamine, enabling a direct comparison to the previous sensing studies on CdSe nanoparticles; further, we have studied the sensing response to changes of the surface characteristics of the aerogel and explored the accessibility of the porous aerogel structure to the external analyte molecules.

CHAPTER 2

EXPERIMENTAL AND CHARACTERIZATION TECHNIQUES

Metal chalcogenide aerogels are synthesized by sol-gel assembly of the corresponding nanocrystals followed by subsequent supercritical CO₂ drying. The prepared nanocrystals and aerogels are characterized by powder X-ray diffraction, electron microscopy (scanning electron microscopy, transmission electron microscopy and energy dispersive spectroscopy), atomic absorption spectroscopy, UV-Visible spectroscopy, diffuse reflectance UV-Visible spectroscopy, photoluminescence spectroscopy, infrared spectroscopy, X-ray photoelectron spectroscopy, and surface area and porosimetry analysis. This chapter will list the chemical materials used in this dissertation study, describe the experimental techniques (glove box utilization, Schlenk line technique, supercritical CO₂ drying) that are used to prepare the metal chalcogenide nanoparticles and aerogels and the characterization techniques used for evaluation of the chemical and physical properties of the synthesized materials.

2.1 Materials

Trioctylphosphine oxide (TOPO, 90%), cadmium oxide (99.99%), tellurium powder (99.9 %), selenium powder (99.5%), trioctylphosphine (TOP, 90%), 11-mercaptoundecanoic acid (MUA, 95%), 16-mercaptohexadecanoic acid (MHA, 90 %), and tetranitromethane (TNM) were purchased from Sigma-Aldrich. Tetramethylammonium hydroxide pentahydrate (TMAH, 99%), triethylamine (TEA, 99%) and silver nitrate were purchased from Acros. N-tetradecylphosphonic acid (TDPA, 98%) was purchased from Alfa-Aesar. Cupric nitrate

(98.8 %), lead nitrate (99.3 %), ethyl acetate, acetone, toluene, pyridine and methanol were purchased from Fisher.

2.2 Experimental Techniques

2.2.1 Inert Atmosphere Glove Box

An inert atmosphere glove box is a device that permits handling and chemical processing of air and/or moisture sensitive materials.¹¹⁸ Generally, a glove box consists of a tightly sealed steel box with a plastic observation window, one or more pairs of arm-length rubber gloves attached to ports on the window, a large and small antechamber equipped with evac/refill controller, purge valves and vacuum pump.¹¹⁸ Materials are transferred into or out of the glove box through the antechamber. Continuous circulation of an inert gas (argon) is necessary to maintain a good inert atmosphere condition. Copper and molecular sieves are used to remove O₂ and H₂O.

2.2.2 Schlenk Line Techniques

Schlenk line techniques are air-free manipulation techniques that allow air sensitive reactions to be performed in the ambient. A Schlenk line is an apparatus consisting of two manifolds: one manifold is connected to a high-vacuum pump; the other is connected to an inert gas line (typically argon or nitrogen).¹¹⁸ Commonly, a Schlenk line has several ports each with two-way stopcocks, so one can run several reactions at the same time with careful management.¹¹⁸ Flasks containing chemicals are connected to the Schlenk line via attachment at these ports. The flasks are degassed first by high-vacuum pump, and then purged with an inert gas. The degassing-purging cycle is repeated several times to achieve an inert

atmosphere in the flask. During an experiment, solvent vapor and gaseous products generated from the reaction are condensed in a liquid N₂ cold trap to protect the vacuum pump, and the inert gas is purged through the reaction vessel and vented via an oil bubbler to release the extra pressure.

2.2.3 Supercritical CO₂ Drying

Supercritical CO₂ drying is one type of wet gel drying technique for the production of aerogels. As mentioned in Section 1.6 of Chapter 1, drying the wet gel under conditions where the solvent is in a supercritical state of solvent can avoid surface tension and collapse of pore walls; therefore, the produced aerogels have minimum gel shrinkage and preserve the wet gel structure.⁷⁵ A liquid will become a supercritical fluid when it reaches the critical point. Different liquids require different temperatures and pressures to bring the liquid to the supercritical state. Organic solvents and liquid CO₂ are often used as the solvent for supercritical drying.⁷⁵ The former needs a high temperature to become supercritical, whereas liquid CO₂ becomes supercritical just above room temperature. A possible “cold” supercritical drying path is shown in Figure 2.1. As illustrated, when the temperature is increased (e.g. up to 39 °C), the pressure of the sealed vessel in a supercritical dryer is automatically increased (ca. 1300 psi, 9 MPa). Liquid CO₂ becomes supercritical. The wet gel is maintained under this condition for certain time (ca. 30 min.) to ensure a complete formation of supercritical fluid. Subsequently, the vessel is slowly vented over a time period of 30-40 min. while maintaining the same temperature. During the venting process, CO₂ is slowly extracted from the gel while staying supercritical, leading to the formation of aerogel. Once the pressure of the system is completely released (complete removal of CO₂),

temperature is decreased to room temperature.

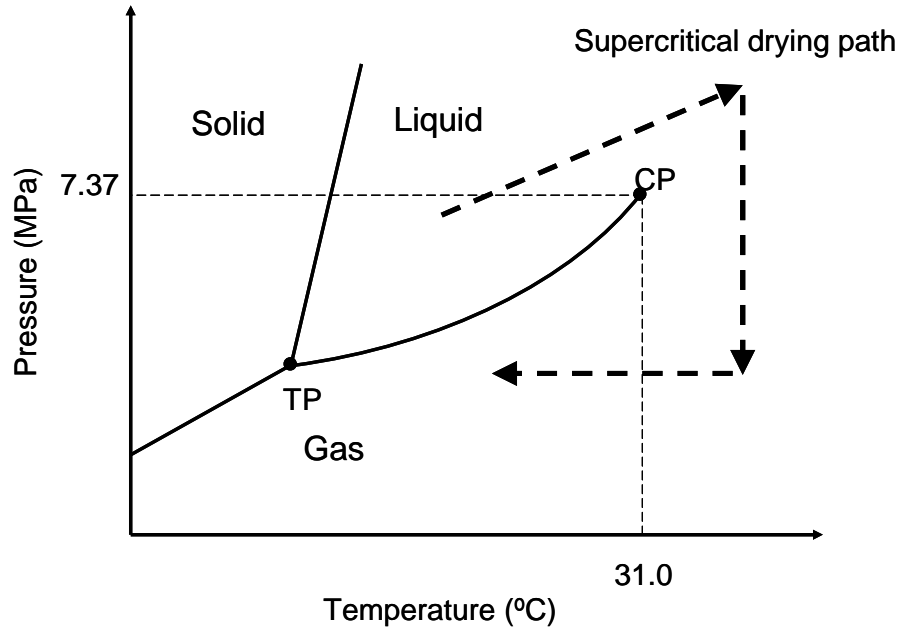


Figure 2.1. Phase diagram of CO₂ and an illustration of a possible supercritical drying path (adapted from Pierre and Pajonk⁷⁵). CP = critical point; TP = triple point.

As mentioned in Section 1.6 of Chapter 1, the supercritical CO₂ drying method produces aerogels that have larger surface areas and retain more of the pore structure of the wet gel relative to the product of “hot” supercritical fluid drying, as it is possible to avoid most side reactions at the lower temperature at which supercritical CO₂ drying is conducted. In this dissertation study we employed a SPI-DRY model critical point dryer equipped with a liquid CO₂ tank for aerogel preparation. An ISOTEMP 1006S model water heater/cooler was used to control the temperature of the CPD chamber. The typical drying process is as follows.

The acetone immersed wet gels are loaded into the CPD dryer boat and subsequently filled with liquid CO₂ at 19 °C and 800-1000 psi. The temperature and pressure is maintained for 3-4 hours to allow complete replacement of the pore liquid (acetone) by liquid CO₂. Fresh liquid CO₂ is refilled once every hour during the exchange step. Subsequently, the temperature is raised to 39 °C and the pressure automatically increases to 1300-1400 psi, producing a supercritical fluid. The fluid is vented over 40 min.

2.3 Characterization Techniques

2.3.1 Powder X-ray Diffraction (PXRD)

PXRD is a widely used diffraction technique in materials science that can provide information about structure, phase and crystallite size. The principle of PXRD mimics the well-known diffraction of visible light by an optical grating wherein diffraction happens when the separation between lines on a grating is comparable to the wavelength of the incident light.² Analogous to optical grating diffraction, PXRD uses X-rays as incident light, and these are diffracted by regularly repeating crystal planes in the material because the interplane spacing is similar to the wavelength of X-rays ($\sim 1 \text{ \AA}$).²

X-rays are generated when high-energy charged particles (e.g. electrons) from a heated filament bombard a metal target. As shown in Figure 2.2, some of the K shell (1s) electrons of the target metal are ionized by the accelerated electrons and leave vacancies. The outer shell electrons immediately transit to the K shell and occupy the vacant sites. Excess energy is released as X-rays during these transitions. The most intense radiation is $K\alpha$ (L-K) and this is consequently used more often than the others (e.g. $K\beta$ (M-K)) in PXRD. In practice, Cu is commonly used as the target metal in diffractometers due to its suitable $K\alpha$

radiation wavelength (1.54\AA) and high intensity. The rest of the radiation is filtered out by a Ni foil to obtain monochromatic beam of $K\alpha$ X-rays.²

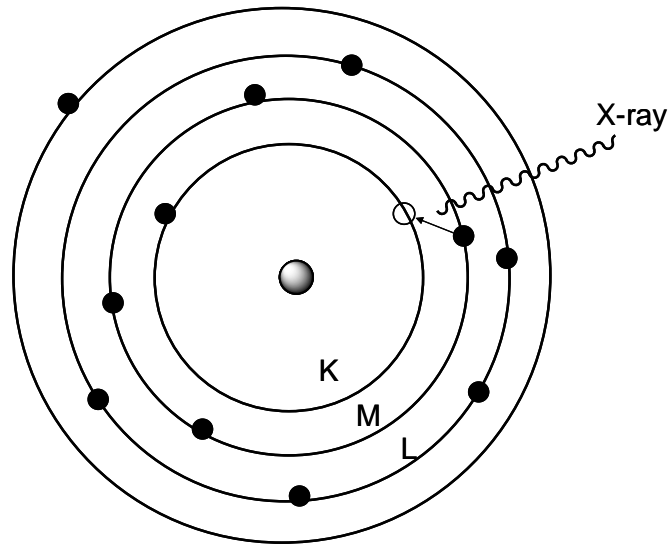


Figure 2.2 Schematic illustration of the formation of an X-ray as an M shell electron drops down to the vacancy in the K shell level, which was left by an ionized K shell electron (adapted from West²).

In a typical PXRD experiment, the monochromatic X-rays are partially scattered by the surface crystal planes at an equal angle to the incident angle and the rest are transmitted to succeeding planes for subsequent scattering. The diffracted X-rays interfere with each other either destructively or constructively. Bragg's law is one commonly used approach to treat diffraction, and is illustrated in Figure 2.3.

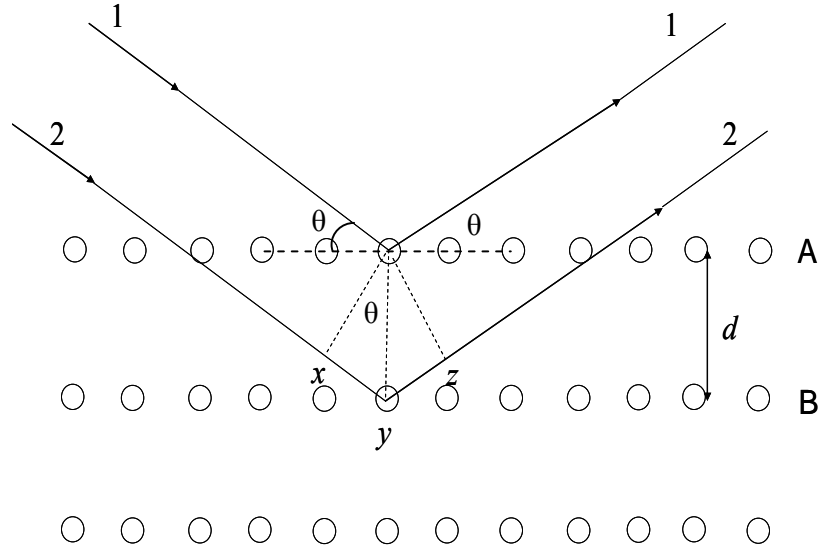


Figure 2.3 Schematic illustration of the diffraction of X-rays by crystal planes (Bragg's law, adapted from West²).

A and B represent two adjacent planes of atoms separated by a perpendicular distance d (d -spacing). 1 and 2 are two incoming X-ray waves that are diffracted by plane A and B, respectively. Wave 1 and 2 are in phase and interfere constructively when the extra traveled distance by wave 2 (xyz) is equal to an integral number of X-ray wavelengths (Equation 2.1). Then the mathematic relationship between the extra distance (xyz), the d -spacing, d , and the angle of incidence, θ can be calculated by Equation 2.2

$$xyz = n\lambda \quad (2.1)$$

$$xyz = 2d\sin\theta \quad (2.2)$$

Then, $2d\sin\theta = n\lambda$ (Bragg's law) (2.3)

Therefore, the reflected beams are in phase and constructive interference occurs when Bragg's law is satisfied. For a crystalline homogenous powder, the lattice planes are present in all possible orientations, leading to diffraction in all direction. When a PXRD experiment is conducted, the diffractometer collects beams from all directions and records the intensity of each beam as a function of 2θ to establish the whole diffraction pattern of the sample. Several structural parameters decide the diffraction pattern. The size and shape of the unit cell decides the peak positions (2θ); whereas the atomic number and position of the atoms in the cell determines peak intensities.² Additionally, peak broadness is related to the crystallinity of a material. A bulk crystalline sample has long range order of lattice planes, therefore complete cancellation of destructive interference can be achieved, leading to narrow peaks in the PXRD pattern. In contrast, a nanocrystalline material has an insufficient number of lattice planes to cancel out all the partially constructive interferences due to its nanoscale particle size, resulting in broadening of the peaks in the diffraction pattern. The broadness of the peak is related to the crystallite size of a nanomaterial and can be calculated by the Debye-Scherrer equation (Equation 2.4),

$$t = 0.9 \lambda / \beta \cos\theta \quad (2.4)$$

where t is the crystallite size; λ is 1.54\AA , the wavelength of K_α radiation if the X-ray source is Cu; 0.9 is a constant for instrumental correction; β is the full width (in radians) at half maximum of the peak at 2θ .

In this dissertation study, PXRD measurements were conducted on a Rigaku RU 200B X-ray diffractometer with a Cu K α rotating anode source. Diffraction patterns were collected from 15-75° (2 θ) at a voltage of 40 kV and current of 150 mA. Powder samples were deposited on a zero background quartz holder with a thin layer of grease. X-ray diffraction patterns were identified by comparison to the phases in the International Centre for Diffraction Data (ICDD) powder diffraction file (PDF) database (release 2000).

2.3.2 Electron Microscopy

Electron microscopy (EM) is another routinely used technique in materials science. In analogy to optical microscopes that use light, electron microscopes utilize highly accelerated electron beams to image specimens. A key difference relative to optical microscopes is that the electron microscope can achieve very high resolution (< 1 nm) because electrons have wavelengths on the ångstrom scale, making them 5,000 times shorter than visible light of 500 nm wavelength. As electrons embody the concept of wave-particle duality, in EM, the wave-like property is used for imaging a specimen, while the particle-like property is used for the transport of characteristic chemical information after the interaction with the specimen.¹¹⁹ Figure 2.4 illustrates several possible processes that occur when highly accelerated electron beams bombard a specimen. Many of these produce electrons as products.

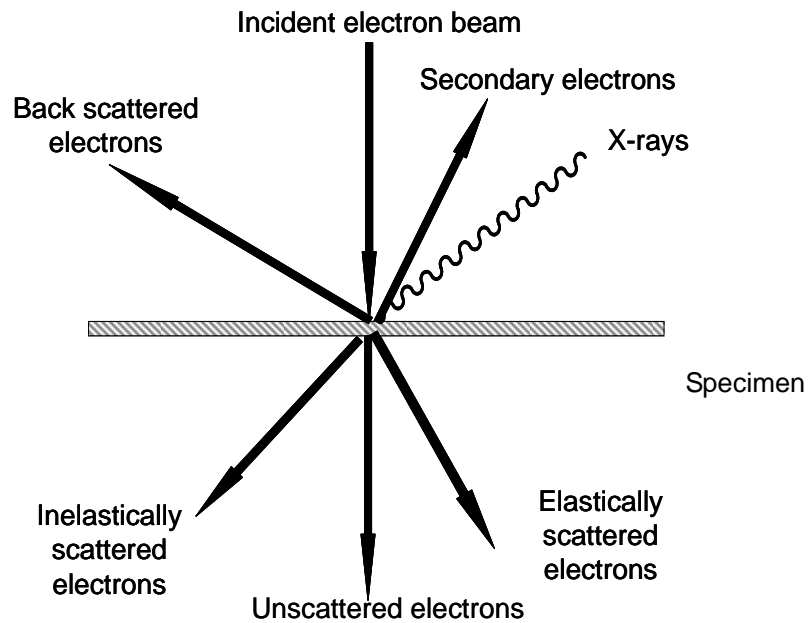


Figure 2.4 Schematic illustration of possible processes when an incident electron beam interacts with a specimen.

Each post-interaction electron beam is related to a specific EM technique. Among EM techniques, scanning electron microscopy (SEM) and transmission electron microscopy (TEM) are two prominent techniques in nanomaterial science. In SEM, the incident electron beam scans across a specimen and the instrument collects the emitted secondary electrons and/or backscattered electrons from the surface of the specimen to form live images of the selected sample areas. SEM is typically used to obtain surface texture and topological information on a specimen. In TEM, transmitted electrons are collected (elastically and inelastically scattered electrons) and amplified to yield detailed information including sample morphology (particle size and shape) as well as crystallographic information due to

diffraction phenomena.¹¹⁹ Additionally, many SEM and TEM instruments are equipped with an energy dispersive spectrometer (EDS), which collects emitted X-rays from the surface of a specimen to yield an X-ray spectrum characteristic of the chemical composition.

2.3.2.1 Transmission Electron Microscopy (TEM)

TEM collects transmitted electrons through ultra thin specimens to investigate the microstructure of materials. The transmission of an electron beams through a sample is ensured when two basic requirements are met: (1) the incident electron beam should be energized by a high accelerating voltage (120 keV to 400 keV); (2) the specimen must be thin enough to facilitate the transmission of the electron beam, thereby the maximum thickness should be in the range of 250 ~ 500 nm. In a typical TEM experiment, the accelerated electron beam is first focused by series of condenser lenses and condenser lens apertures into a thin and coherent beam that is subsequently focused onto the sample by an objective lens. The transmitted electron beam from the sample is then expanded by a projector lens onto a fluorescent screen. The images can be captured by a digital camera. All the lens systems are installed in a high vacuum system to ensure travel of the electron beam in an inert environment with zero resistance.¹¹⁹

There are two basic operation modes in TEM for imaging specimens: bright field and dark field images. Bright field mode is the most common imaging method in TEM. Under this condition, TEM collects either both the directly transmitted incident beam and the diffracted beam or only the incident beam (by blocking the diffracted beam). The dark areas in an image are the regions with thicker samples or with larger atomic number. Whereas, the bright areas are the regions with thin or no sample.¹¹⁹ The dark field mode operates under

diffraction contrast conditions where only selected diffraction beams are collected to form an image. In this technique, the diffracted electron beam in the preferred direction can be selected by using objective aperture, therefore, only those sample areas that cause that preferred direction diffraction will be imaged. The rest of the areas with no sample or sample that can not cause that specific diffraction will appear dark.¹¹⁹ Therefore, the bright field images generally provide morphology information (e.g. particle size and shape), while dark field images are used for obtaining crystallographic information.

In this dissertation study, the TEM analysis was performed in bright field mode by using a JEOL FasTEM 2010 HR analytical electron microscope operating at a 200 kV acceleration voltage. Finely powdered aerogel samples were dispersed in acetone followed by sonication. For nanocrystals, samples were dispersed and sonicated in their dispersion solution. One drop of the sample solution was added onto a carbon-coated copper TEM grid and the solvent was allowed to evaporate prior to introduction to the instrument.

2.3.2.2 Scanning Electron Microscopy (SEM)

SEM detects the energy of secondary electrons that are ejected from the surface of a specimen during the interaction between the incident electron beam and the specimen. In a SEM, the incident beam is accelerated by a voltage of 25- 50 keV in a vacuum system and focused by pairs of condenser lenses with apertures before exposure to the specimen. When the incident beam bombards the specimen, electrons lose energy by random scattering and absorption by the surface of the specimen.¹¹⁹ Normal imaging in the SEM uses secondary electrons. Secondary electrons are emitted by inelastic scattering interactions between the incident electron beam and the conduction band electrons of metals, or valence band

electrons of semiconductors and insulators, which are weakly bound. The electrons of the sample absorb the energy and escape from the sample surface. However, since the energy transfer in this process is inefficient, secondary electrons have low kinetic energies (~5 eV). The positively charged detector collects these secondary electrons and converts them into a signal to form images. Because these secondary electrons are caused by random inelastic scattering, they are emitted from all directions related to the topology of the sample surface. Therefore, SEM is particularly useful for obtaining topological and surface feature information on a material. Because surface charge can easily build up, induced by the electron beam, SEM specimens must be conductive or semiconductive. Non-conductive (e.g. polymers) samples need to be sputtered with a thin layer of conductive material (e.g. gold) prior to SEM analysis.¹¹⁹ A conventional SEM can achieve the highest resolution in the range of 1 nm ~ 20 nm. Compared to TEM, the resolution of SEM is lower, but samples do not have to be ultra thin.

2.3.2.3 Energy Dispersive Spectroscopy (EDS)

Many conventional SEM and TEM instruments are equipped with an EDS detector, which analyzes X-rays emitted from the surface of a specimen during the interaction of the incident electron beam and the sample.¹¹⁹ Similar to the X-ray generation process described in the previous section for PXRD (Section 2.3.1), the generation of X-rays in Electron Microscopy is caused by the ionization of inner shell electrons of the atoms and subsequent transitions between outer shell electrons and inner shell holes. Each of the electron transitions between orbitals in an element has a specific energy, such that the emitted X-ray has a characteristic wavelength (energy). Hence, by probing the energy of X-rays emitted, the

elemental composition of the sample is determined. Further, by recording the intensity of the X-rays as a function of energy, the relative amount of each element can be detected. Therefore, EDS is routinely used to obtain information about elemental composition of a sample.¹¹⁹ SEM/EDS is commonly used to analyze elements heavier than sodium, due to the relative high background noise in the low energy region, which makes detection of lighter elements more problematic. Moreover, some of the K shell X-rays (which are at a higher energy compared to L shell X-rays) can not be detected because of the low accelerating voltage in the SEM. In contrast, TEM/EDS can overcome these shortages owing to its high accelerating voltage and the low background noise in the low energy region.

In this dissertation study, elemental compositions of nanocrystals and aerogels were determined by using an *in situ* energy dispersive spectroscopy unit (EDAX Inc.) within SEM/EDS or TEM/EDS instruments. For SEM/EDS, a small amount of powder sample was sprinkled on carbon tape attached to an aluminum sample holder and data were collected on a Hitachi S-2400 operating at 25 kV. For TEM/EDS, sample preparation and operation of the TEM is the same as that for TEM imaging (see Section 2.3.2.1). EDS data were analyzed by using the EDAX Genesis software.

2.3.3 X-Ray Photoelectron Spectroscopy (XPS)

XPS is a technique used for obtaining the surface chemical and elemental information of a material. In a typical XPS experiment, high energy X-rays bombard the surface of a specimen, photoelectrons are ejected from either a valence electron shell or an inner core electron shell of the surface atoms (to a depth of a few nanometers) and must overcome the work function to escape.¹¹⁹ The kinetic energy (E_k) of the photoelectrons is mathematically

related to the binding energy (E_b) of the photoelectrons, the energy of incident X-rays ($h\nu$) and the work function (Φ) of the material, as shown by Equation 2.5,

$$E_k = h\nu - E_b - \Phi. \quad (2.5)$$

Therefore, if the kinetic energy can be measured and the energy of the incident photons is known, the binding energy of the ejected photoelectrons can be determined. The binding energy is characteristic of a specific element, and thus by integrating peak intensity, the elemental composition of the surface of the material can be determined. Additionally, depending on the oxidation state of an element, the binding energy shifts slightly. Therefore, by comparing the shift of the binding energy to the reference value, one can determine the oxidation state of the elements present in a material.

In this dissertation study, a Perkin Elmer PHI 5500 ESCA spectrometer was employed to record the XPS spectra by using monochromatic Al K α radiation (1486.6 eV). For sample analysis, a small amount of aerogel was pressed onto a piece of indium foil ($\sim 1 \text{ cm}^2$). Indium foil was chosen as the support material because it is conductive, preventing specimen charging, and because it is soft, enabling good contact and acting as an adhesive for the specimen.¹²⁰ All the collected XPS peak positions were calibrated against the “adventitious” carbon (1 s) binding energy (284.6 eV) by curve fitting the measured carbon 1s peak. The ratio of the peak areas of Se²⁻ and SeO₂ was used to evaluate the relative extent of oxidation in as-prepared, heated and pyridine-washed aerogels. The peak areas were obtained by fitting each of the peaks using the Gaussian/Lorentzian curve fitting program from the RBD analysis suite.

2.3.4 Surface Area and Porosimetry Analysis

Gases or vapors tend to be adsorbed by the cooled free surface of a solid and can be further condensed within pores if the solid has a porous structure. Therefore, the gas or vapor adsorption process can be used to extract information about the surface area, and the pore structure of the solid can be determined by evacuation of the gas or the vapor adsorption process.¹²¹ In general, adsorption of gases by solids can be caused by chemical bond formation (chemisorption) or driven by van der Waals forces (physisorption) between gas molecules (adsorbates) and the surface atoms or ions of solids (adsorbents).¹²¹ Chemisorption changes the electronic structure of the surface of a solid, whereas the process of physisorption is reversible and non-destructive due to the weak intermolecular interactions.

In practice, when an experiment is conducted on a surface area and porosimetry analysis instrument, a solid sample is placed in a sealed sample holder (e.g. a glass tube) and loaded in the degassing unit of the instrument. The degassing step is performed by pre-heating the sample either under high vacuum or under flow of a chemically inert gas (e.g. N₂ or He) to remove contaminants (e.g. water or small organic molecules) from the surface of the sample. Once the sample is sufficiently degassed, it is transferred to the analysis unit of the instrument and cooled to cryogenic temperature, e.g. 77.2 K by application of a liquid N₂ bath. A small amount of adsorbate is then introduced in steps into the sample tube. If a chemically inert gas (e.g. N₂ or He) is used as the adsorbate, the gas molecules are physisorbed on the surface of the sample, resulting in a decrease in the gas pressure and an increase in the sample mass. Once the sample surface is saturated, the gas pressure in the sample tube reaches equilibrium. The amount of the adsorbed gas can be calculated from the pressure change by using gas laws, supposing the volume of the sample tube and mass of the

sample is known.¹²¹ At constant temperature, the quantity of the adsorbed gas is related to several parameters (the nature of the gas and solid, mass of the sample, and the pressure of the gas) and can be calculated as a function of relative pressure if the rest of parameters are fixed, as shown in Equation 2.6,

$$n = f(p/p_o)_{T, \text{ gas, solid}} \quad (2.6)$$

where n is the quantity of adsorbed gas, which can be expressed in several ways, e.g. volume of gas adsorbed (cm^3/g); P/P_o is the relative pressure, where P and P_o are the equilibrium and saturation pressure of the gas. Therefore, an adsorption isotherm can be obtained by plotting volume of gas adsorbed (cm^3/g) vs. the relative pressure (P/P_o).¹²¹ In practice, both adsorption and desorption isotherms are recorded.

The shape of the adsorption/desorption isotherm depends on the adsorption/desorption process in the sample. Generally, the adsorption of gas molecules by a sample can be monolayer adsorption, multilayer adsorption, capillary condensation or a combination of these processes, depending on the porosity and pore structure of the sample. At low relative pressure, monolayer adsorption first occurs on the sample surface, leading to the filling of micro-size ($< 2 \text{ nm}$) pores. As the pressure is increased, multilayer adsorption starts to take place, resulting in the filling of meso- (2-50 nm) to macro-size ($> 50 \text{ nm}$) pores. When the pressure is further increased to saturation pressure, gas molecules start to condense into liquid by the force of capillary condensation, which results in a hysteresis loop in the adsorption/desorption isotherm due to the difference in the rates of filling and withdrawing the adsorbates in and out of the pores.¹²¹ The adsorption/desorption isotherms can be

therefore classified into 6 major types (type I-VI) by the shape of the isotherm (Figure 2.5). The hysteresis loops are categorized into 4 types (type H1-H4) depending on the shape of the pores (cylindrical, slit-shaped, etc).

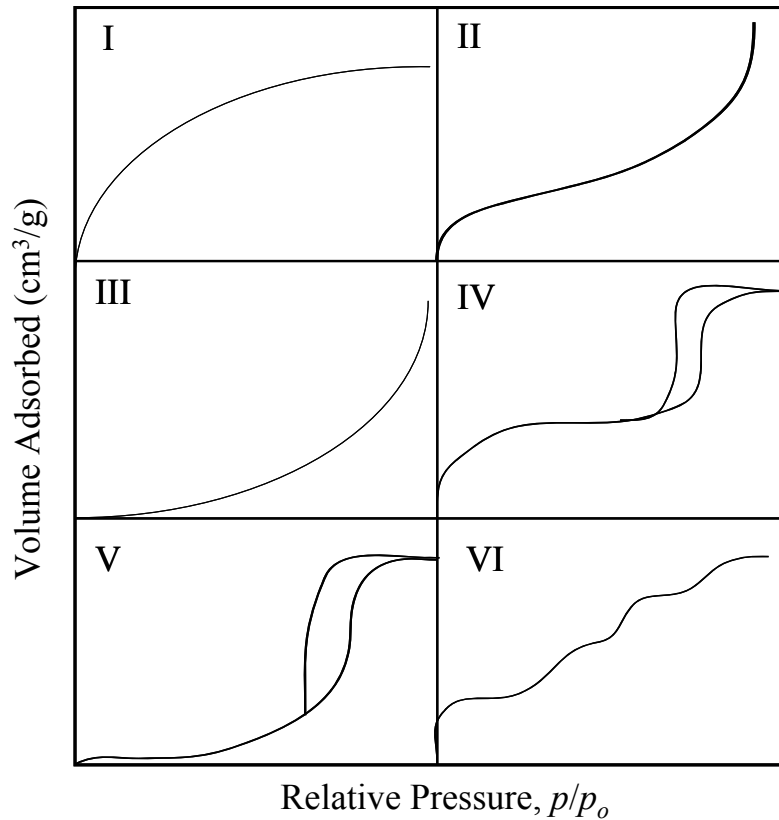


Figure 2.5 Six basic types of adsorption/desorption isotherms, adapted from Gregg.¹²¹

Surface area and porosity information can be extracted by applying theoretical models to the adsorption/desorption isotherms. Langmuir theory is generally employed for monolayer adsorption where chemisorption takes place. As an extension of Langmuir theory, Brunauer, Emmett, and Teller (BET) theory considers multiple layer adsorptions by physical

forces, assuming no interactions between layers, therefore it is suitable for analyzing the surface areas of mesoporous materials.¹²¹ The BET theory calculates the surface area of a sample by using the BET equation (Equation 2.7) which treats the low relative pressure region in the adsorption isotherm (monolayer coverage)

$$\frac{P}{V_a(P_o - P)} = \frac{1}{V_m C} + \frac{C - 1}{V_m C} \frac{P}{P_o} \quad (2.7)$$

where P and P_o are the equilibrium and saturation pressure of the adsorptive gas; V_a is the quantity of gas adsorbed at pressure P ; V_m is the quantity of gas adsorbed when a monolayer coverage is achieved; and C is a constant. By plotting $P/[V_a(P_o - P)]$ vs. P/P_o , a straight line is produced with slope and intercept equal to $(C-1)/V_m C$ and $1/V_m C$, respectively. The quantity of the adsorbed gas expressed in moles per gram of sample can be calculated by conversion from the volume of adsorbed gas in monolayer (V_m).¹²² The total surface area of the sample can then be obtained from the amount of adsorbed gas molecules (moles per gram of sample) and the surface area occupied by a single adsorptive gas molecule (e.g. 16.2 \AA^2 for a molecule of N_2).¹²²

The information about porosity of a sample, including pore size, pore size distribution and cumulative pore volume, can be extracted from the adsorption/desorption isotherm by applying Barrett, Joyner, and Halenda (BJH) theory or density functional theory (DFT).¹²² The BJH theory is commonly used to model cylindrical pores in a solid sample, whereas the DFT model assumes that the pores have slit geometry. The BJH theory collects information mainly from the region of the isotherm where critical condensation pressure is reached, which corresponds to pore filling/emptying of meso- and macro-porous materials. The BJH

model uses the Kelvin equation (Equation 2.8) to calculate the pore size distribution assuming the filling (removal) of condensed adsorbates in the pores is in a stepwise manner as the relative pressure increases (decreases).¹²² In the Kelvin equation, P^* and P_o are the critical condensation and saturation pressure; γ is the surface tension of the liquid;

$$\ln \left[\frac{P^*}{P_o} \right] = - \left[\frac{2\gamma v \cos \theta}{R T r_m} \right] \quad (2.8)$$

v is the molar volume of the condensed adsorbate; θ is the contact angle of the solid and the condensed phase; r_m is the mean radius of curvature of the liquid; R is the ideal gas constant and T is the absolute temperature.¹²² For example, as the pressure decreases (desorption branch), the quantity of adsorbates removed from the pores in each step is related to the core volumes of pores emptied in that step. If the thickness (t) of the adsorbed layer remaining on the pore walls is considered, the Kelvin equation is modified by substitution of $(r-t)$ for r_m . The thickness can be mathematically obtained by the thickness equation (Equation 2.9).

$$t = \left[\frac{A}{B - \log_{10}(P/P_o)} \right]^{1/2} \quad (2.9)$$

$$\log \left[\frac{P}{P_o} \right] = B - \frac{A}{V_a^2} \quad (2.10)$$

where A and B are constants and that are obtained by the Harkins-Jura equation (Equation 2.10), as the slope and intercept, respectively, in the plot of $\log(p/p_o)$ vs. $1/V_a^2$. Therefore, the value of r can be computed by using Equations 2.8 to 2.10. By repeating the above

calculations for each step, a pore size distribution for the solid can be obtained. Knowing the radius (r) and assuming the geometry of pores is cylindrical (a key assumption of the BJH model), the total length of the cylinder can be calculated by measuring the volume of adsorbed gas in each step using the general equation for the volume of regular cylinder ($V = \pi r^2 L$). The cumulative pore volume can then be calculated as the sum of the volume of each step.¹²²

In this dissertation study, an ASAP 2010 surface area and porosimetry analyzer from Micromeritics was used to obtain nitrogen adsorption and desorption isotherms at 77 K for powdered aerogel samples. The BET model was applied to the isotherms to determine the surface areas of the aerogels. The BJH model was used to generate a pore-size distribution plot and calculate the average pore diameter and cumulative pore volume. CdSe and CdTe aerogel samples were degassed under high vacuum at 100°C for 48 hours before analysis whereas ion-exchanged aerogels (prepared in the dissertation research of Chapter 4) are degassed at 50°C for 48 hours.

2.3.5 UV-Visible Absorption Spectroscopy (UV-Vis)

UV-visible absorption spectroscopy is a widely used spectroscopic technique for studying the absorption properties of materials in UV-Visible region (200 ~ 800 nm). The energies of light in the UV-visible region often correspond to the required energies for many types of electronic transitions, such as pi bonding orbital to pi anti-bonding orbital ($\pi \rightarrow \pi^*$), nonbonding orbital to pi anti-bonding orbital ($n \rightarrow \pi^*$) and some transitions between d orbitals in transition metal complexes. Substances that exhibit these types of electronic transitions are said to be or contain chromophores.¹²³ In a UV-Vis experiment, when incident

light is shone on the solution of a material containing one or more chromophores, part of the light is absorbed by the solution, and the resultant transmitted light is detected, producing a spectrum with absorption bands. The absorption bands are usually broad due to the presence of vibrational and rotational states between the electronic energy states.

In semiconducting materials, the absorption of light excites electrons from the valence band to the conduction band, resulting in an absorption edge in the optical spectra. The energy of the absorbed photons is equal to the band gap energy of the material. In semiconducting nanomaterials, the quantum confinement effect results in an increase of the band gap energy relative to bulk counterparts, as discussed in Section 1.1 of Chapter 1. The blue shift of the band gap energy (ΔE) can be calculated by using the effective mass approximation model (Equation 1.1), which shows ΔE to be approximately inversely proportional to the size of the semiconductor nanocrystals.⁶ However, the calculated chromophore size of nanocrystals by UV-Vis is sometimes quite different from the particle size obtained from PXRD or TEM, due to errors in the effective masses of electrons and holes, the use of bulk dielectric constant values and the fact that ignoring coupling of electronic states and surface states is not accounted for in the effective mass approximation model.

In this dissertation study, the UV-Vis absorption properties of nanocrystal solutions were evaluated with a Hewlett-Packard (HP) 8453 spectrophotometer. Nanocrystal solutions were prepared by diluting the original solution ten fold. UV-Vis spectra were scanned in the range of 400 – 800 nm against a blank solution of the solvent used. The band gap values of the nanoparticles were estimated from the absorption onsets, which were determined by extrapolating the linear portion of the absorption curve to the baseline of the absorption

spectrum for each of the samples. The errors in the measurement are estimated to be no more than 0.01 eV (12 nm). However, the values represent only an average, as there is always some degree of polydispersity in the samples.

2.3.6 Diffuse Reflectance UV-Visible Spectroscopy (DRS)

Diffuse reflectance UV-Vis spectroscopy is a useful spectroscopic technique that collects reflected radiation from samples. Unlike transmittance spectroscopy in which samples should be transparent, DRS is specifically designed for measuring the reflectance that is related to the absorption properties of non-transparent or solid samples.¹²⁴ When incident light reaches the sample, two types of reflection processes can take place. One type of reflected radiation is that due to surface reflection, where light is directly reflected off the surface of the sample and does not contain optical information for the sample. The other type of reflection comes from the diffuse reflectance. In the process of diffuse reflectance, incident light penetrates into the particles of the sample and while part of the light is scattered off, the rest of the light is transmitted through the particles to other particles in the sample. During transmission, some light can be absorbed by the particles if there is a transition of appropriate energy. The scattering, transmission and absorption processes can occur multiple times in the sample media. Eventually, light is returned back to the surface of the sample carrying optical information for the sample.¹²⁴ The diffuse reflectance is mathematically related with the absorbance of light by the sample, and the relationship can be described by Kubelka-Munk equation (Equation 2.11),

$$(1 - R)^2/2R = k/s \quad (2.11)$$

where R is the percentage reflectance; k is the absorption coefficient; and s is the scattering coefficient. Therefore, absorbance can be obtained from reflectance data by conversion using the Kubelka-Munk model.¹²⁴

In practice, a DRS instrument does not measure the absolute reflectance of a sample; instead, the relative reflectance is measured against a white standard material (e.g. MgO or BaSO₄) which has k equal to 0 and R_{std} equal to 1.¹²⁵ A spherical mirror coated with a 100% reflecting material is used to reflect and collect radiation from all sample orientations to ensure all the radiation is focused onto the detector. The detector scans the wavelength and records the spectrum with the y axis as reflectance and the x axis as wavelength. By plotting $(1 - R)^2/2R$ vs. wavelength (λ), one can obtain the absorption spectra of the material and determine the band gap energy of a semiconductor from the onset value of the absorption plot.

In this dissertation study, a Jasco V-570 UV/VIS/NIR spectrophotometer equipped with an integrating sphere was used to measure the optical diffuse reflectance of samples of nanoparticles and aerogels. A small amount of powder was spread evenly on the sample holder and measured from 1000 to 200 nm (1.24 eV ~ 6.20 eV). The baseline was corrected by a reflectance standard (BaSO₄). The reflectance data was converted to absorption to yield the optical absorption spectra according to the Kubelka-Munk equation.¹²⁶ The band gap values of the aerogels and precursor nanoparticles were estimated from the absorption onsets.

2.3.7 Photoluminescence Spectroscopy (PL)

Photoluminescence spectroscopy is a routinely employed spectroscopic technique for

studying the emission properties of semiconducting nanomaterials. PL can be classified into two categories: fluorescence and phosphorescence. Fluorescence takes place when electrons drop down from singlet excited states to singlet ground states and excess energy is released as photons.¹²⁷ Phosphorescence occurs when electrons relax from triplet excited states to singlet ground states via a radiation pathway. Fluorescence has a short life time (10^{-5} - 10^{-8} s) but high intensity due to its high probability of occurrence, whereas phosphorescence has a long life time (10^{-4} – 10^4 s) but is generally weak because it is less probable. Semiconducting nanomaterials exhibit size-dependent photoluminescence properties. When an excitation light source shines on the material absorption occurs promoting an electron to the conduction band, and then excited electrons in the conduction band relax to the valence band via emission processes.

In the dissertation research, a Cary Eclipse (Varian, Inc.) fluorescence spectrometer was used for studying emission properties of nanoparticles and aerogels and collecting static and kinetic data during the gas sensing experiments. Nanoparticle solutions were loaded in a 1 cm quartz fluorescence cell and analyses were conducted under ambient conditions. Powder aerogel samples were sealed in evacuated quartz tubes and analyses were conducted at liquid nitrogen temperature. A 1 cm quartz cell with a screw cap and embedded septum was used as the sample holder for sensing study.

2.3.8 Infrared Spectroscopy (IR)

Infrared spectroscopy is a commonly used spectroscopic technique that measures IR frequencies of chemical functional groups of a sample by positioning the sample in the optical path of an incident IR light.¹²³ Light in the IR region of the spectrum has

wavenumbers (frequencies) spanning from 13,000 to 10 cm^{-1} . IR frequencies often correspond to the vibration frequencies of atoms in molecules. However, only those vibrations that correspond to changes in the dipole moment will result in IR activity, resulting in an absorption band in the IR spectrum. The most interesting IR region for chemical analysis ranges from 4,000 to 400 cm^{-1} , which corresponds to the vibration frequencies of many organic functional groups of chemicals.

In this dissertation study, a Varian FTS 3000 MX FTIR spectrometer was employed to evaluate the type and estimate the quantity of surface functional groups present in the aerogel samples. To prepare samples for analysis, 120 mg of KBr powder and 10 mg of aerogel were ground together in a mortar and pestle then pressed into a transparent pellet in a 13 mm diameter die using a Carver hydraulic pellet press.

2.3.9 Atomic Absorption Spectroscopy (AAS)

Atomic absorption spectroscopy is a routinely used analytical technique for determination of analyte concentration in solution. In AAS, when a photon of incident radiation has a specific energy that is equal to the difference between the ground state and excited state of a free atom in a gaseous sample, this energy can be absorbed. The intensity of absorbance is therefore related to the number of atoms present in the gaseous sample.¹²³

Two common methods are used in today's AAS instruments for the atomization of elements in sample solutions into free atoms in the gaseous states: flame atomization and electrothermal atomization. In flame atomization, small droplets of sample solution are aspirated into a spray chamber by a nebulizer assembly and mixed with combustion gases in the spray chamber. The sample is then delivered to the burner and converted into a dry

aerosol and further volatilized into vapors, which contain solid particles, such as molecular species, ionic species and free atoms. The combustion gas is a mixture of fuel and oxidant gases, such as air-acetylene or nitrous oxide-acetylene. The former is used for elements that need low thermal energy for atomization whereas the latter is used for elements that require high thermal energy to be atomized.¹²³ Proper alignment of the burner within the optical path of the instrument is necessary in an AAS experiment to ensure the absorbance of light by the sample.

In the electrothermal atomization method, a graphite furnace consisting of a graphite tube with an optically transparent window is commonly used as the atomizer. A small amount of sample is injected into the graphite tube and atomized by the thermal energy provided as a result of resistive heating of the graphite tube. Compared to the flame atomization method, the electrothermal atomization method improves sensitivity around 1000 times by trapping the sample in a small tube, but the reproducibility is relatively low due to the difficulty in controlling the atomization efficiency.

A hollow cathode lamp (HCL) consisting of a cathode and an anode within a glass tube is commonly used as the radiation source in an AAS instrument. When a potential is applied to the electrodes, the filled inert gas in the HCL is ionized and collides with the cathode surface. Some “sputtered” atoms in excited energy states emit radiation with a wavelength characteristic of the metal that the HCL cathode is manufactured from.¹²³ In an AAS experiment, the HCL lamp is selected by matching the metal of the HCL cathode with the metallic substance of interest in an analyte sample. By this means, the HCL lamp can produce radiation with photon energies that can be absorbed by the analyte. In an AAS measurement, the Beer-Lambert law can be applied, but nonlinear calibration curves are

usually produced due to instrumental limitations. Therefore, in practice, an accurate measurement is predicated on measurement of a series of standard solutions of the interested metal ions of to obtain a calibration curve that can be applied to determine the concentration of the analyte metals.

In this dissertation study, a Perkin Elmer AAnalyst 700 atomic absorption spectrometer equipped with flame and graphite furnace atomizers was employed for determination of Cd concentration, $[Cd^{2+}]$, in solutions of nanocrystal and aerogel samples. Sample solutions were diluted in 2 vol% HNO_3 solution with sonication prior to the AAS measurement. The air-acetylene flame technique was used. The $[Cd^{2+}]$ of five standard solutions was measured to establish a calibration curve and a 2 vol% HNO_3 blank solution was used to correct the background signal.

CHAPTER 3

POROUS CADMIUM TELLURIDE NANOCRYSTAL ASSEMBLIES: LIGATION EFFECTS ON THE GELATION PROCESS AND THE PROPERTIES OF THE RESULTANT AEROGELS

3.1 Introduction

This chapter is focused on a detailed study of the assembly of CdTe nanocrystals into porous gels and aerogels. The main objective of the study is to extend the metal chalcogenide aerogel family to tellurides (specifically CdTe) and evaluate the consequences of oxidative gelation of semiconducting telluride nanoparticles into 3-D architectures on the optical properties. Herein, we report the 3-D assembly of CdTe nanocrystals capped with thiolate or nonthiolate (trioctylphosphine oxide) ligands via a two-step sol-gel synthetic strategy followed by supercritical CO₂ drying. The structure, morphology, surface area, porosity, and optical properties of the resultant aerogels will be characterized and compared to each other and to a recent report of CdTe gels in the literature.¹⁰⁸

3.2 Experimental Section

All the chemicals used in this chapter are listed in Section 2.1 of Chapter 2.

3.2.1 Synthesis of TOPO-Capped CdTe Nanocrystals

TOPO-capped CdTe nanocrystals were prepared by Peng et al's method¹²⁸ with slight modification. A typical synthesis procedure occurs as follows. A mixture of CdO powder (0.0514 g), TDPA (0.1116 g) and TOPO (3.7768 g) was loaded in a 250 mL Schlenk flask and slowly heated to 320 °C under argon flow to obtain a clear solution. The

temperature of the reaction solution was reduced to 270 °C and a tellurium precursor (0.0664 g of tellurium powder dissolved in 2.4 mL of TOP) was quickly injected. The reaction solution was cooled down to 100 °C immediately after the injection and then slowly heated back to 240 °C (10 °C per 10 min) where it was left for 1 hour and then allowed to cool to room temperature. The resultant CdTe nanocrystals were dispersed in toluene and precipitated with methanol. After centrifugation, the precipitate of CdTe nanocrystals was redispersed in toluene and the resultant CdTe sol containing insoluble species was centrifuged one more time to remove the byproducts and impurities. The subsequent CdTe sol was induced to precipitate with methanol to obtain the purified TOPO-capped CdTe nanocrystals. These were either subjected to direct gelation or the thiolate ligand exchange procedure. Prior to gelation of TOPO-capped CdTe nanocrystals, the purified nanocrystals were redispersed in toluene and reprecipitated by methanol twice more before final dispersion in 16 mL of toluene.

3.2.2 MHA-Capping of CdTe Nanocrystals

MHA-capping of CdTe nanocrystals was achieved by following a modification of the method reported by Aldana *et al.*¹²⁹ Briefly, 0.5770 g of MHA was dissolved in 10 mL of methanol and the pH was adjusted to > 10 using TMAH. In the absence of light, the resulting solution was added to TOPO-capped CdTe nanocrystals prepared from one batch of the reaction described in the proceeding section and shaken vigorously to assure that the CdTe nanocrystals were dispersed completely. The resultant MHA-capped CdTe nanocrystals were precipitated by ethyl acetate and dispersed in methanol. Ethyl acetate was used to wash the

nanocrystals two times to remove excess MHA and other byproducts. The purified MHA-capped CdTe nanocrystals were dispersed in 16 mL methanol for gelation.

3.2.3 Gelation of MHA-Capped and TOPO-Capped CdTe Nanocrystals

Gelation of a MHA capped CdTe sol was generally achieved by addition of 0.05 mL of a 0.3 vol% tetranitromethane (TNM) methanolic solution to 4mL aliquots ($[Cd^{2+}] = 0.012M$) of the MHA-capped CdTe sol.¹³⁰ The subsequent solution was shaken vigorously to obtain a homogeneous mixture. Typically, gelation was observed 3-4 hours after mixing. Alternatively, gelation can be achieved by photochemical methods, in which the MHA capped CdTe sol is illuminated by a mercury lamp for 9 hours. The resultant gels are allowed to age 7-10 days under ambient conditions.

Gelation of a TOPO capped CdTe sol was performed by addition of 0.05mL 0.3 vol% TNM methanolic solution to 4 mL of the TOPO-capped CdTe sol ($[Cd^{2+}] = 0.011M$). Gelation was observed 3-4 days after mixing with oxidant. The resultant wet gel was aged for 2-3 weeks under ambient conditions prior to drying.

3.2.4 Production of TOPO-Capped and MHA-Capped CdTe Aerogels

TOPO-capped and MHA-capped CdTe aerogels were obtained by exchange of the wet gels from Section 3.2.3 with acetone 4 ~ 5 times per day over two days, followed by supercritical CO₂ drying with a SPI-DRY model critical point dryer. The typical drying process follows the procedure that was described in Chapter 2, Section 2.2.3.

3.2.5 Dispersion Studies

Thiolate solutions of MHA were prepared for dispersion studies by dissolving 0.1443g of MHA in 5 mL of methanol followed by addition of TMAH to drive the pH to >10. TOPO-capped CdTe aerogel (~10 mg) was dispersed in the above MHA solution. Ethyl acetate was used to precipitate the dispersed nanocrystals. The resultant nanocrystals were washed with ethyl acetate once more to remove excess thiolates and dispersed in 4 mL of methanol to obtain a nanocrystal sol for TEM evaluation.

3.3 Results

3.3.1 Synthesis and Assembly of CdTe Nanocrystals

The precursor trioctylphosphine oxide (TOPO)- capped CdTe nanocrystals were prepared by arrested precipitation using a literature method¹⁰ and the phase was confirmed to be that of hexagonal CdTe by powder X-ray diffraction pattern (PXRD) (Figure 3.1). The crystallite size was calculated to be 4.4 nm from the application of the Scherrer Equation to the peak at 39° (2θ). A portion of the nanocrystals was subjected to surface exchange with thiolate ligands under basic conditions (pH>10). Intriguingly, our standard thiol, employed in exchange, 11-mercaptoundecanoic acid (MUA), resulted in transformation of the (red) sol into a black precipitate identified as crystalline Te by PXRD (Fig 3.2) when added to the TOPO capped CdTe nanocrystal solutions. Accordingly, a longer chain thiol, 16-mercapohexadecanoic acid (MHA) was explored and found to yield stable thiolate-capped sols. Gelation of the MHA-capped CdTe nanocrystals was achieved via oxidative removal of the surface thiolate groups by use of a chemical oxidizing agent (tetranitromethane, TNM). Use of 0.025 mL of 3 vol% of TNM methanol solution (resulting in the concentration ratio of

TNM to Cd^{2+} equal to 1:8¹³¹) led to gelation, but this was accompanied by bleaching, resulting in a white gel. In contrast, 0.05 mL of 0.3 vol% TNM ($[\text{TNM}]: [\text{Cd}^{2+}] = 1:40$) led to slow gelation over 3-4 hours with no loss of color. The resultant wet gel was aged for 7 days under ambient conditions to obtain a robust monolithic wet gel. For comparison, photo-oxidation of a CdTe nanocrystal sol under mercury lamp illumination was explored for gelation.

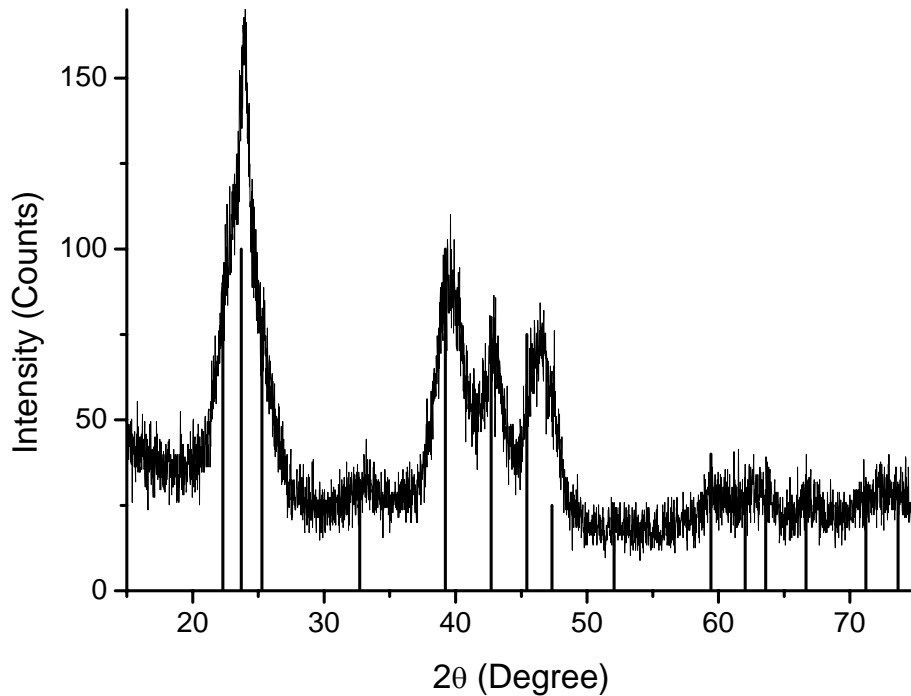


Figure 3.1 PXR D pattern of TOPO-capped CdTe nanocrystals. The ICDD-PDF overlay of hexagonal CdTe (PDF # 19-0193, solid lines) is shown as vertical lines

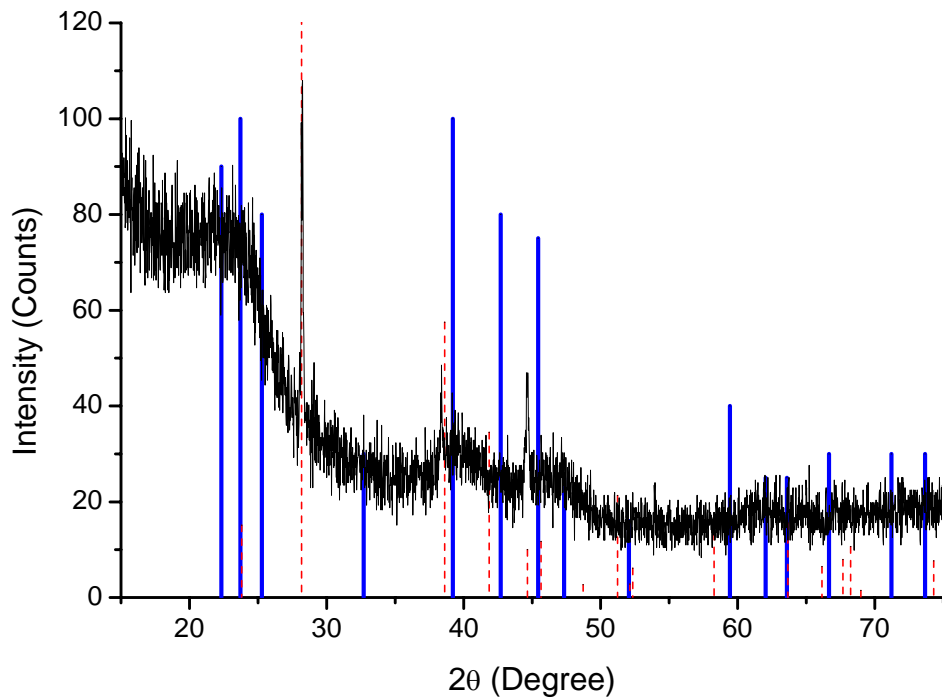


Figure 3.2 PXRD pattern of MUA exchanged CdTe nanocrystals. The ICDD-PDF overlays of hexagonal CdTe (PDF # 19-0193, solid lines) and hexagonal Te (PDF # 85-0557, dotted lines) are shown as vertical lines

TOPO-capped CdTe Nanocrystals have been found to be capable of direct assembly into gels without first undergoing surface exchange with thiolate. This was achieved by redispersing the as-prepared nanocrystals with toluene and reprecipitating them with methanol two times prior to addition of TNM. The dispersion/reprecipitation process was found to be critical for the gelation process. If nanocrystals are not dispersed/reprecipitated or this is done only once, gelation of the nanocrystal sol is not observed after mixing with oxidant. In contrast, if nanocrystals are dispersed/reprecipitated more than two times, or a

stronger TOPO solubilizing solvent (i.e., chloroform) is used, the nanocrystals can not be dispersed to form a sol. As for the TOPO-capped CdTe gelation, 0.05 mL of 0.3 vol% TNM was applied to 4 mL of TOPO-capped nanocrystal sol to achieve the concentration ratio of $[\text{TNM}]:[\text{Cd}^{2+}]$ to be 1:40. The first sign of gelation (viscosity change) was observed in 3 to 4 days and complete gelation (clear supernatant) required 3 weeks.

3.3.2 Structure and Porosity of CdTe Aerogels

As shown in Figure 3.3, the PXRD pattern of the aerogels resulting from TOPO-capped or MHA capped CdTe nanocrystals are identical and consistent with the hexagonal CdTe crystal structure of their primary TOPO capped CdTe nanocrystals, and the peak breadths are essentially identical for all materials studied, suggesting the crystallite size has not changed. The small peak at 27.9° in the PXRD of TOPO-capped aerogel is attributed to a small amount of crystalline Te, while the broad peak at 30° might be due to amorphous component produced during the depassivation process in the synthesis of the TOPO-capped aerogel.

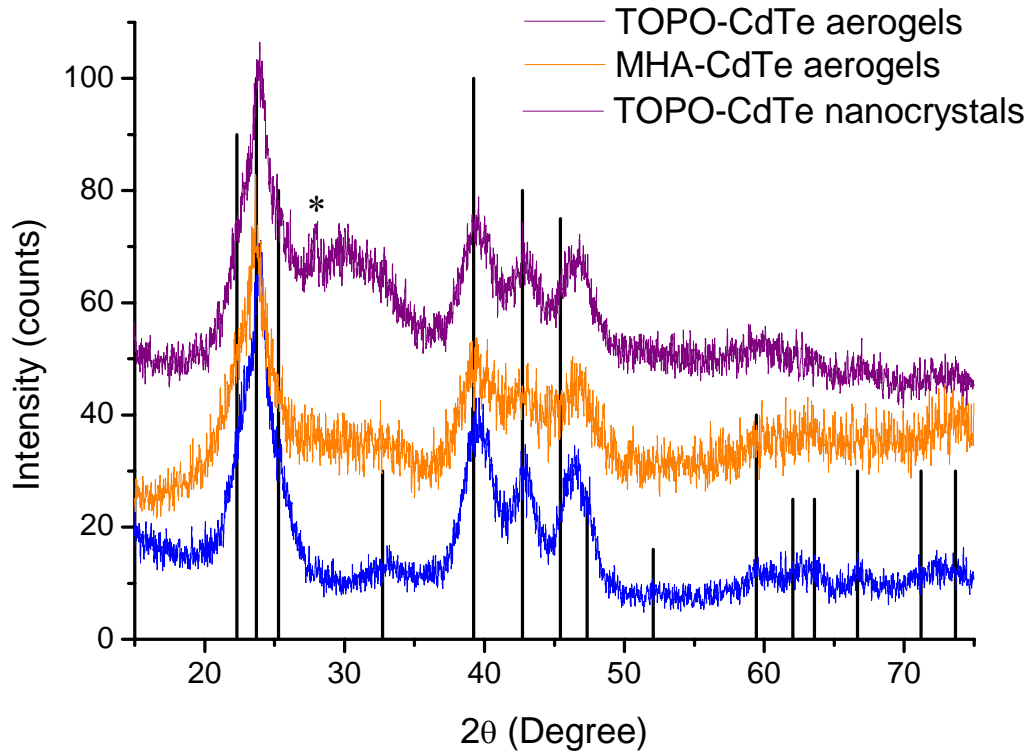


Figure 3.3. PXRD pattern of TOPO-capped and MHA-capped aerogels and of TOPO capped CdTe nanocrystals. The ICDD-PDF overlay of hexagonal CdTe (PDF # 19-0193) is shown as vertical lines. * indicates the most intense reflection of crystalline Te.

Transmission electron microscopy was employed to study the morphology of the CdTe aerogels assembled from TOPO-capped and MHA-capped nanocrystals (Figure 3.4). The two aerogels exhibit similar colloidal morphologies with a broad range of pores extending from the micro (<2 nm), through meso- (2–50 nm), and into the macro (>50 nm)-porous regime. HRTEM images of the two aerogels demonstrate the presence of

interconnected networks composed of nearly spherical nanocrystals. Lattice fringes clearly show the nanoscale building blocks to be highly crystalline. These can be indexed to hexagonal CdTe in both aerogels.

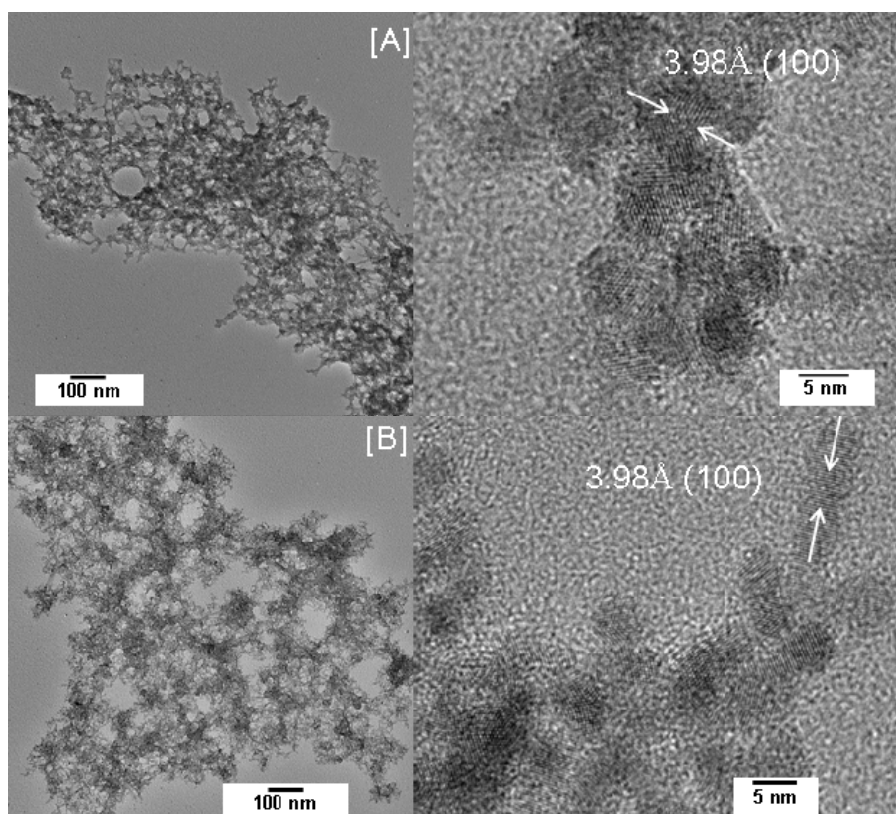


Figure 3.4 TEM images of MHA-capped [A] and TOPO-capped [B] aerogels (left, low resolution; right, high resolution). Groups of lattice fringes, and their corresponding d-spacing and indices, are shown in the high resolution images

Elemental compositions of the precursor nanocrystals and TOPO-capped and MHA-capped CdTe aerogels are shown in Table 3.1. The ratio of Cd to Te is approximately 1:1 in the primary nanocrystals and the assembled forms, consistent with the formulation of

CdTe. The P content of the twice toluene dispersed/reprecipitated TOPO-capped nanocrystals was decreased to 7.3% from 12.2% in the as-prepared nanocrystals due to the partial removal of TOPO ligands during the dispersion/reprecipitation process. This value is further reduced to 5.9% in the aerogel, presumably due to loss of even more TOPO from the particle surface during the oxidation process. In the case of thiolate-capped systems, a substantially decreased P content confirmed that the majority of the TOPO ligands were replaced by MHA capping groups. A small amount of S was still observed in the MHA-capped CdTe aerogel, attributed to the presence of residual thiolate functionalities on the surface of the building blocks.

Table 3.1 EDS data of CdTe nanocrystals and aerogels

Sample	Elemental Composition				Atomic ratio
	Cd (%)	Te (%)	P (%)	S (%)	
TOPO-capped CdTe nanocrystal	42.8	40.2	17.0	ND	Cd:Te:P 1:0.93:0.40
dispersed/reprecipitated TOPO-capped CdTe nanocrystal	46.5	46.2	7.3	ND	Cd:Te:P 1:0.99:0.16
TOPO-capped CdTe aerogel	48.2	45.9	5.9	ND	Cd:Te:P 1:0.95:0.12
MHA-capped CdTe nanocrystals	39.3	35.8	6.5	18.4	Cd:Te:P:S 1:0.91:0.16:0.46
MHA-capped CdTe aerogel	47.2	45.8	1.0	6.0	Cd:Te:P:S 1:0.97:0.02:0.13

Porosimetry characteristics of the prepared aerogels were determined by N₂ adsorption/desorption isotherms. The adsorption and desorption isotherms of the aerogels from MHA-capped and TOPO-capped CdTe nanocrystals demonstrate a type IV curve, which is characteristic of a mesoporous material, and are similar in shape (Figure 3.5). The calculated BET surface areas of the TOPO-capped and MHA-capped CdTe aerogel are comparable to a “traditional” silica aerogel (600 m²/g) when converted to silica equivalence by normalization for density differences (Table 3.2). A broad pore size distribution is consistent with meso- to macro- porosity in both of the aerogel materials (Figure 3.5), consistent with a lighty electron micrograph images (Figure 3.4). The TOPO-capped aerogel has a slightly larger average pore diameter and a higher cumulative pore volume than the MHA-capped aerogel.

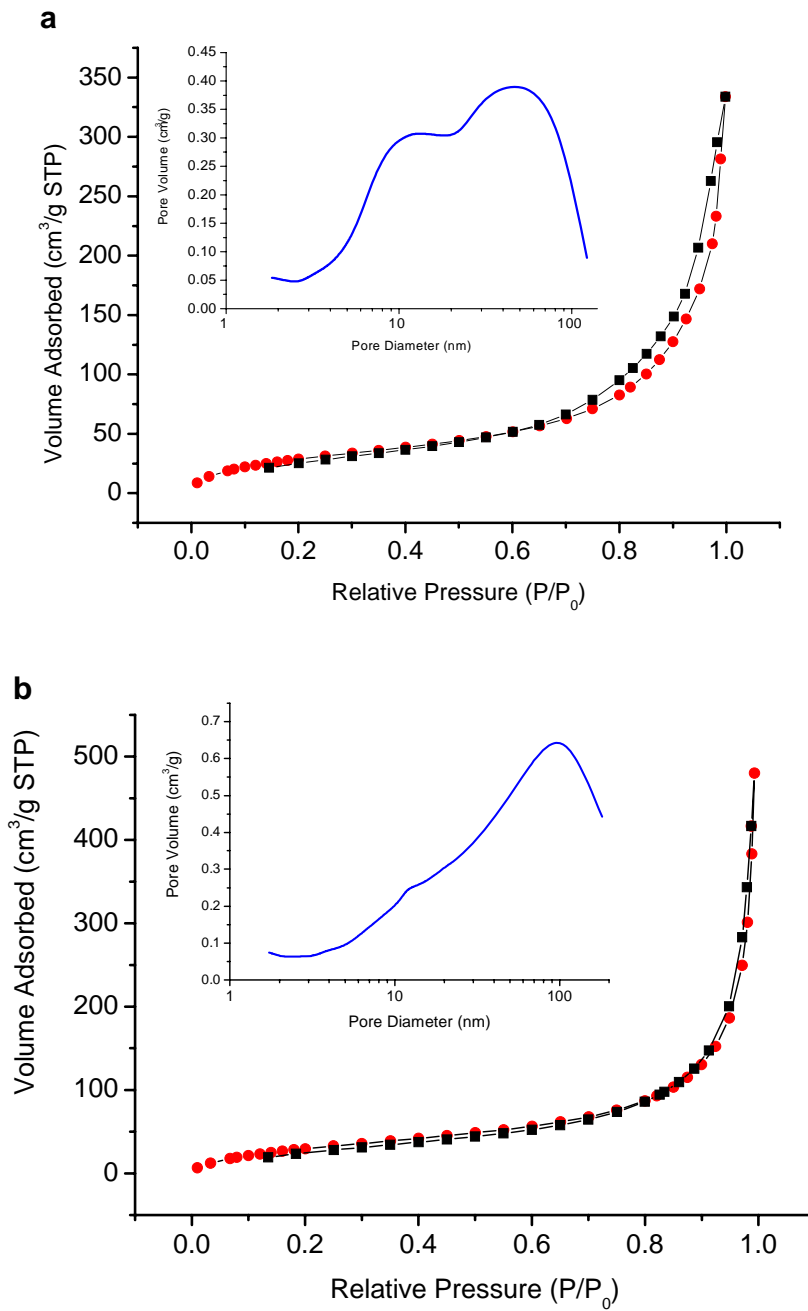


Figure 3.5. N_2 adsorption (filled circles) /desorption (filled squares) isotherm of TOPO-capped (a) and MHA-capped CdTe aerogel; the inset shows the BJH pore size distribution

Table 3.2. Porosimetry data for CdTe aerogels

Sample	BET surface area (m ² /g)	Silica equivalence BET surface area (m ² /g) ^a	BJH average pore diameter (nm)	BJH cumulative pore volume (cm ³ /g)
TOPO-CdTe aerogel	126	502	12.2	0.74
MHA-CdTe aerogel	115	458	11.3	0.52

^a Silica equivalence surface areas were computed by converting the BET surface area for 1 mol of CdTe aerogel into that for 1 mol of SiO₂ using respective compound formula masses.

3.3.3 Optical Properties of TOPO-capped and MHA-capped CdTe Aerogels

The energy band gap values of CdTe aerogels were measured as the onsets of the optical absorption spectra converted from diffuse reflectance measurements (Figure 3.6). The TOPO-capped and MHA-capped aerogels exhibit identical band gaps at 1.92 eV, a value which is significantly higher than that of bulk CdTe, 1.50 eV, demonstrating that the aerogels are effectively quantum confined. These band gap energy values are slightly red shifted compared to the energy value (1.95 eV) of the nanocrystal precursor.

In an effort to assess the effect of gelation strategy, chemical vs photo-oxidation, on photo-physical properties, the band gap of a photo-oxidized MHA-capped aerogel was also evaluated (Figure 3.6). The obtained band gap was 2.02 eV, which is considerably larger than that for TNM oxidized MHA-capped aerogel (1.92 eV) or for the precursor nanocrystals (1.95 eV). Moreover, there is a pronounced absorbance tail into the red.

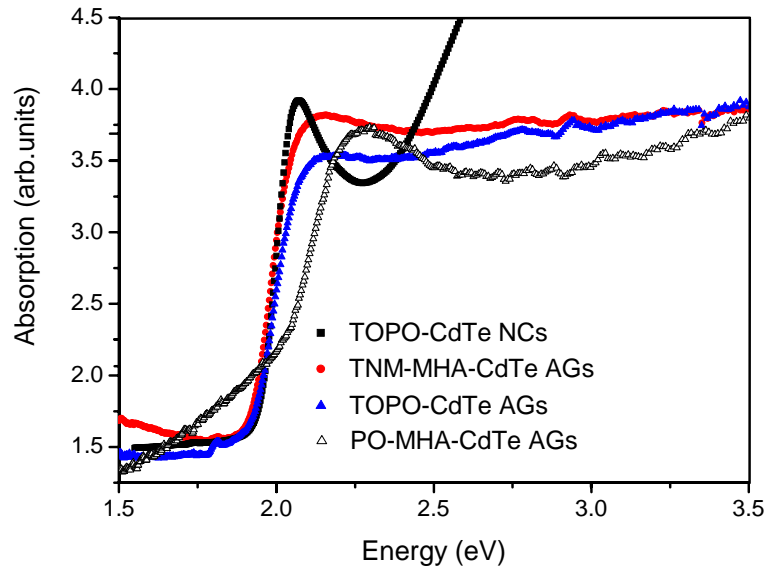


Figure 3.6 Optical absorption (data converted from diffuse reflectance) spectra of TOPO-capped nanocrystals (TOPO-CdTe NCs) (black squares), and TNM oxidized MHA-capped aerogels (TNM-MHA-CdTe AGs) (red circles), TOPO-capped aerogel (TOPO-CdTe AGs) (blue triangles) and photo-oxidized MHA-capped aerogels (PO-MHA-CdTe AGs) (white triangles)

Photoluminescence studies on the as-prepared TOPO-capped CdTe nanocrystals reveal a sharp band-edge emission at 610 nm (Figure 3.7). This is retained in the MHA-capped nanocrystal products but with a decreased relative intensity and the addition of a broad peak centered at 680 nm (Figure 3.7). This new peak is attributed to the presence of surface hole-traps induced by thiolate capping functionalities (Figure 3.7). In contrast, the TNM oxidized MHA-capped CdTe aerogels exhibit fully quenched band-edge luminescence. However, upon heating the TNM oxidized MHA-capped CdTe aerogels at 100°C under high vacuum, a small portion of band-edge emission can be recovered (Figure 3.7). The

photoluminescence of photo-oxidized MHA-capped CdTe aerogels was measured to compare to that of the TNM oxidized MHA-capped aerogels. As Figure 3.7 shows, photo-oxidized aerogels do exhibit a small band-edge emission, in contrast to the as-prepared TNM oxidized aerogel. Since thiolate capping groups are known to be effective hole-traps on the aerogel surface,¹³² the TOPO-capped aerogels were expected to show better luminescence intensity as there is no thiolate present. However, the aerogel prepared from TOPO-capped nanocrystals also shows entirely quenched luminescence (Figure 3.7).

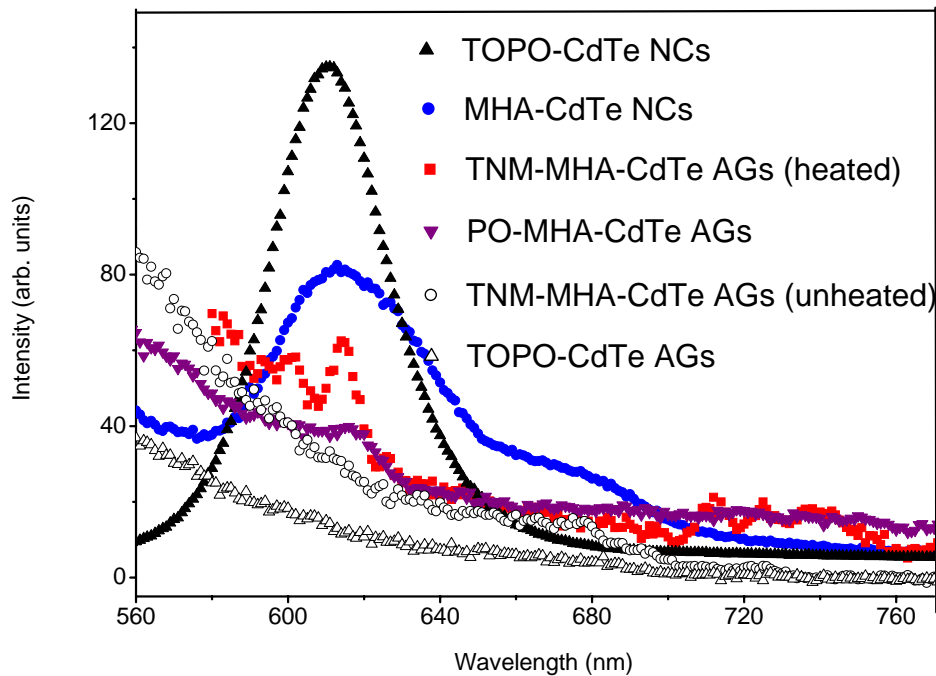


Figure 3.7 Photoluminescence spectra of TOPO-capped (black triangles) and MHA-capped (blue circles) CdTe nanocrystals, and heated TNM oxidized MHA-capped CdTe aerogels (red squares), photo-oxidized MHA-capped CdTe aerogels (purple triangles), unheated TNM oxidized MHA-capped CdTe aerogels (white circles) and TOPO-capped CdTe aerogels (white triangles).

3.3.4 Dispersion Studies

Dispersion studies were conducted by addition of a methanolic solution of MHA/TMAH ($\text{pH} > 10$) to the TOPO capped CdTe aerogels. The recovered nanocrystal sols were visually identical to the primary nanocrystal sol. Evaluation of the product by TEM revealed that the gels had been converted to finely dispersed nanocrystals (Figure 3.8).

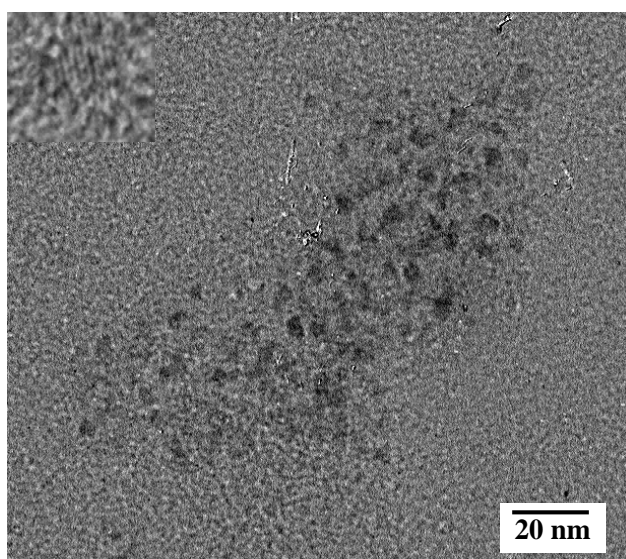


Figure 3.8. TEM image of a dispersed TOPO-capped CdTe aerogel solution. The inset shows a high resolution TEM image of a single nanocrystal of CdTe.

3.4 Discussion

3.4.1 Comparison of CdTe Aerogels to CdS and CdSe Aerogels

Typically, formation of CdS or CdSe aerogels involves (1) preparation of trioctylphosphine oxide capped nanocrystals; (2) surface exchange with thiolate capping ligands; (3) oxidative loss of thiolate ligands; (4) oxidative gelation of nanocrystals. The thiol

of choice is MUA because the relative long chain acts as a good stabilizer, making the surface less accessible to oxygen and hence resistant to spontaneous photo-induced aggregation. The relatively stable sol can then be transformed to a gel when ready by addition of chemical oxidants.

A key difference in the preparation of CdTe AGs relative to CdSe and CdS AGs is the amount and concentration of oxidants used for gelation of the MHA capped CdTe Nanocrystals relative to that for MUA capped CdS and CdSe Nanocrystals. When the same concentration ratio of TNM to nanocrystals (1:8), used for gelation of CdS and CdSe Nanocrystals was initially applied to the CdTe nanocrystal solution, a compact and white colored gel was formed. The shrinkage of the gel network indicates the oxidizer to thiolate ratio ($x=[\text{TNM}]/[\text{MHA}]$), which controls the number of reactive surface sites, as proposed by Gacoin et al,³² is too big. The presence of excess oxidant causes formation of new interparticle bonds after gelation, due to the presence of excess reactive sites, thus leading ultimately to shrinkage of the gel network. In contrast, decrease ratio ($[\text{TNM}]/[\text{Cd}^{2+}]=1/40$) was found to efficiently lead to slow and controlled gelation after 3-4 hours. The fact that the same relative concentration of TNM successfully used for CdS and CdSe with minimal syneresis ($\text{Volume}_{\text{gel}}/\text{Volume}_{\text{sol}}=\text{ca.}60\sim80\%$) causes significant CdTe gel shrinkage ($\text{Volume}_{\text{gel}}/\text{Volume}_{\text{sol}}=\text{ca.}10\sim20\%$) may be explained by the lower redox potential for Te^{2-} relative to Se^{2-} and S^{2-} , leading to a greater number of bonds formed between particles. The bleaching phenomenon (observation of a white colored gel from a red sol) was not mentioned in Gacoin et al.'s study³² of CdS, even when the oxidant concentration was high ($x>0.8$). However, Eychmüller and co-workers¹⁰⁸ did observe similar bleaching of CdTe gels at high oxidant concentration. The color change is likely due to formation of tellurates (TeO_4^{2-}) due

to the oxidation of surface telluride by TNM; tellurates are reported to form upon reaction of telluride or tellurium with oxidizing agents (e.g. H_2O_2 , or chromic acid).¹³³ Again, observation is consistent with more facile oxidation of Te^{2-} to S^{2-} or Se^{2-} .

Another difference in the synthesis of CdTe AGs relative to CdS and CdSe AGs is that MHA is used as the thiolate stabilizer for surface exchange of TOPO-capped CdTe Nanocrystals instead of MUA, as is used for CdS and CdSe Nanocrystals. The latter was found to yield elemental Te (as revealed by PXRD) when combined with the TOPO-capped CdTe sol. While the origin of this phenomenon is not clear, it is possible that an adventitious oxidant is introduced with MUA. This is also consistent with a greater susceptibility to oxidation on the part of CdTe relative to CdS and CdSe where no such problems were encountered during MUA capping.

3.4.2 Effect of Capping Ligand on Gelation and Properties of the Resultant Aerogels

In addition to the gelation by our standard route (decomplexation of thiolate-capped nanocrystals), we also evaluated the gelation of TOPO capped CdTe Nanocrystals. A critical step is removal of a portion of the surface groups to expose Te^{2-} for oxidation. This is achieved by two cycles of dispersion with toluene followed by reprecipitation with methanol of the nanocrystals to obtain a moderately depassivated nanocrystal surface, followed by the chemical oxidation reaction. It was found that a single dispersion/reprecipitation step yielded a sol that was resistant to gelation, while dispersion/reprecipitation more than 2 times, or when a strong TOPO solubilizing solvents produced precipitates (i.e., the precursor particles could not be redispersed to form a sol); the former suggests an insufficient depassivation on

the nanocrystal surface, and the latter indicates a near complete decomplexation of the capping ligands from particle surface.

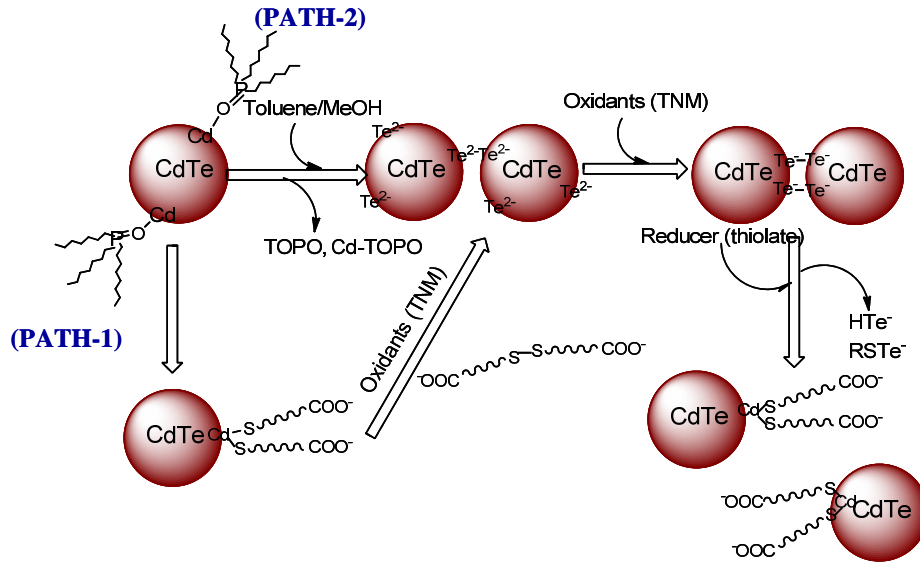
Whereas MHA capped CdTe nanocrystal sols start to gel in 3-4 hours and form a stable monolith after a further 7-10 days of aging, the TOPO capped nanocrystals require 3-4 days before an apparent viscosity change is even observed, and subsequent aging is generally performed over 3 weeks to obtain complete gelation (clear supernatant). The slower process of TOPO capped CdTe gel formation suggests the gelation process for TOPO-capped CdTe Nanocrystals is not as efficient as that for MHA-capped nanocrystals. In the latter case, the presence of an oxidant during ligand (thiolate) removal enables exposed CdTe surface to immediately react, whereas oxidant was added as a separate step after ligand removal in the gelation of TOPO-capped nanocrystal sol, perhaps leading to some kind of surface chemical rearrangement or reaction that makes the particles less susceptible to gelation. However, when comparing all the collected data on the characterization of as-prepared TOPO capped and MHA capped AGs, the physicochemical properties of both of the materials are found to be nearly identical in terms of structure, morphology, crystallinity, quantum confinement effect, surface area and porosimetry. One difference is the observation of crystalline Te and small amount of amorphous phase in the PXRD of the TOPO-capped CdTe aerogel. This is likely due to over oxidation resulting in phase separation of elemental Te in the final aerogel product. The amorphous phase could be due to residual TOPO that was not washed away completely after the depassivation process or to an amorphous oxidation product. Over all, the similarity of the properties of TOPO-capped and MHA-capped CdTe AGs indicates that ligation on the nanocrystal surface does not have a major effect on the gelation process as long as proper depassivation of the particle surface is achieved, consistent with the finding in

the proposed mechanism study⁹⁶ for gelation of CdSe Nanocrystals, where surface thiolate groups are oxidatively removed first but oxidation of the subsequently exposed surface chalcogenides is the step responsible for network formation. Moreover, these data suggest that the gelation itself can not involve any thiolate linkages, as was observed in the TGA-Cd gels prepared by Eychmüller and co-workers.¹⁰⁹

3.4.3 Proposed Mechanism for Gelation of TOPO Capped CdTe Nanocrystals Based on Dispersion Studies

Based on the data presented above, we propose a similar mechanism to that responsible for gelation of CdSe is occurring in the MHA-capped and TOPO-capped nanocrystals, as shown in Scheme 3.1. Partial depassivation of TOPO-capped CdTe nanocrystals is achieved either by oxidative removal of surface thiolate capping groups after exchange with thiolates (Scheme 3.1, PATH-1) or by dispersion with toluene/precipitation with methanol two times to remove surface TOPO ligands and/or Cd-TOPO species (Scheme 3.1, PATH-2). Both of the actions are expected to lead to a Te-rich surface. Upon oxidation, Te^{2-} is then oxidized to $\text{Te}^{\cdot-}$ species which can combine with species on other particles to form $(\text{Te}_2)^{2-}$ or $(\text{Te}_n)^{2-}$ between particles, leading to gelation. As shown with the dispersion studies, these $(\text{Te}_n)^{2-}$ linkages can be reduced by thiolate, re-forming the sol.

Scheme 3.1. Proposed mechanism of TOPO capped and MHA-capped CdTe oxidative gelation and reductive dispersion



3.4.4 Comparison of Current Results to Previous Studies on CdTe Assembly

Compared to previous studies on 1D or 2D assembly of thiolate-capped CdTe nanocrystals by Kotov *et al.*^{54, 56} and 3D assembly of thiolate-capped CdTe nanocrystals by Gaponik *et al.*,¹⁰⁸ the current study showed that CdTe gels can be assembled not only from thiolate capped CdTe nanocrystals but also from their phosphine oxide capped precursor by simple chemical oxidation of the primary nanocrystal sol. The TEM study revealed that the prepared CdTe aerogels in this study exhibit similar pearl-necklace assembly morphology to networks in previous studies. However, the luminescence properties of the CdTe aerogels presented here are poor relative to the nanowires and sheets of Kotov's studies^{54, 56} or the gels of Eychmüller's study.¹⁰⁸ Comparing the synthesis method of the present study to these

former studies, the present method used oxidizing agent to induce slow aggregation of nanocrystals in methanol (MHA-capped nanocrystals) and toluene (TOPO-capped nanocrystals); whereas, Kotov's luminescent nanowires or sheets were prepared in aqueous solution under light-free conditions, suggesting photo-oxidation is not operative in this case. It is not clear whether there is a different assembly mechanism or some adventitious oxidant present in the system that is responsible for the network formation in this case.

Eychmüller and co-workers' study produced aerogels by chemical oxidation methods that are similar to our findings. Specifically, they observed PL quenching for the H_2O_2 oxidized AGs and bleaching phenomenon when H_2O_2 concentration is high. However, their UV-light illuminated (photo-oxidized) AGs were found to be highly photoluminescent. Therefore, we performed a study on the effect of chemical vs. photo-oxidative gelation on the photo-physical properties of aerogels. However, our photo-oxidized aerogel exhibit actually has a wider gap than the precursor nanocrystals, suggesting surface etching or oxidation (i.e., smaller chromophore size). While peaks due to band-edge PL are discernible, the PL is weak and not evident to the naked eye, as is the case for the gels produced by Eychmüller and co-workers. The exhibited poor PL properties of the prepared CdTe AGs in this study might be due to over oxidation the CdTe Nanocrystals either by over exposure of the CdTe Nanocrystals to TNM or $h\nu/O_2$ during the gelation and aging process or the oxidants strength being too high (in the case of TNM). Indeed, the study by Eychmüller and co-workers found that if slow centrifugation was employed after the first sign of gelation in both H_2O_2 oxidation and photo-oxidation gelation processes, a higher degree of PL was observed. In the former case, centrifugation was used to enhance coagulation and remove unreacted H_2O_2 hence avoiding over oxidation of nanocrystals. In the latter case, centrifugation followed by

immediate washing was used to facilitate interparticle networking to shorten the photo-oxidation time (again effectively limiting oxidizing equivalents). These approaches, while rendering useful optical properties, are likely to result in sedimentation/compaction of the gel, reducing surface areas. As Gaponik et al. have not performed surface area analysis, no direct comparison can be made.

3.5 Conclusions

Overall, the present study has shown that CdTe Nanocrystals can be assembled into highly porous gels and aerogels, regardless of the surface ligation (i.e. thiolate capping is not obligatory). The aerogels exhibited similar structural, morphological and porosimetry properties, suggesting the surface ligation has no major effect on the gelation process and the resultant aerogel properties. Based on this statement, we expect a similar synthetic mechanism is operable for the tellurides as found for sulfide and selenide nanocrystal assembly. While the aerogels remain quantum confined, the PL is highly quenched. The origin is not clear, but is most likely related to oxidation. Future work will focus on maintaining the high surface area achieved by oxidation induce gelation while minimizing surface oxidation to preserve PL.

CHAPTER 4

CATION EXCHANGE REACTIONS IN METAL CHALCOGENIDE AEROGELS: SILVER SELENIDE, LEAD SELENIDE AND COPPER SELENIDE GELS AND AEROGELS

4.1 Introduction

In this chapter, a general synthetic method for metal chalcogenide gels and aerogels via cation-exchange reactions of primary wet gels is described. This work is undertaken in order to extend the accessible compositions, physical properties and thus applications of the existing members of the chalcogenide aerogel family by an approach that is synthetically complementary to the nanocrystal assembly route. Herein, we report the synthesis of Ag_2Se , PbSe and CuSe gels and aerogels by cation-exchange reactions of CdSe wet gels. Elemental composition analysis and optical spectroscopy are employed to monitor the exchange process. The structure, morphology and pore characteristics of the resultant materials are evaluated and compared to the primary CdSe aerogels. Additionally, a process of partial cation exchange for production of macroscopic heterostructures will be presented and discussed.

4.2 Experimental Section

All the chemicals used in this chapter are listed in Section 2.1 of Chapter 2.

4.2.1 Synthesis of CdSe Nanoparticles, Gels and Aerogels

TOPO-capped CdSe nanoparticles were synthesized by a literature method¹⁰ with a small modification. A typical synthesis is as follows. A mixture of CdO powder (0.0514 g), TDPA (0.1116 g) and TOPO (3.7768 g) was loaded in a 100 mL Schlenk flask and slowly

heated to 320 °C under argon flow to obtain a clear solution. The temperature of the reaction solution was reduced to 280 °C and a selenium precursor (0.0316 g of selenium powder dissolved in 2.4 mL of TOP) was quickly injected. The reaction solution was cooled down to 150 °C immediately after the injection and slowly heated back to 250 °C (10 °C per 10 min). The CdSe nanoparticles were grown at 250 °C for 4 hours. The resultant CdSe nanoparticles were dispersed in toluene and precipitated with methanol.

MUA-capping CdSe nanoparticles was performed following a modification of the method reported by Aldana *et al.*¹²⁹ Briefly, 0.4360 g of MUA (targeting a Cd²⁺: MUA molar ratio of 1:5) was dissolved in 10 mL of methanol and the pH was adjusted to ~ 10 using TMAH. In the absence of light, the resulting solution was added to TOPO-capped CdSe nanoparticles and shaken vigorously to assure CdSe nanoparticles were dispersed completely. The resultant MUA-capped CdSe nanoparticles were precipitated with ethyl acetate and redispersed in 10 mL of methanol. Ethyl acetate was used to wash the nanoparticles twice more to remove excess MUA and other by-products. The purified MUA-capped CdSe nanoparticles were then dispersed in 16 mL of methanol for gelation.

Gelation was conducted by addition of 0.05 mL of 3 % TNM methanolic solution to 4 mL aliquots of the above MUA-capped CdSe sol according to our standard procedure.³⁴ The subsequent solution was shaken vigorously and allowed to sit on the bench top under ambient fluorescent light for 1 week without disturbance to yield a monolithic CdSe wet gel. The aged monolithic wet gel was subjected to supercritical drying or cation-exchange reactions.

CdSe aerogels were obtained by exchange of the wet gel with acetone 4 ~ 5 times per day for two days followed by supercritical CO₂ drying. The drying process followed the procedure that was described in Chapter 2, Section 2.1.3.

4.2.2 Synthesis of Ag₂Se Gels and Aerogels

Ag₂Se gels were prepared by cation-exchange reactions of CdSe wet gels with Ag⁺. Typically, 4 mL of 0.15 M (6 times the nominal Cd²⁺ amount) AgNO₃ methanolic solution was added to a vial of a CdSe wet gel (assembled from 4 mL of CdSe sol ([Cd²⁺] 0.025 M)). The addition of the Ag⁺ ion solution to the CdSe wet gel was performed cautiously to assure no disturbance of the monolithic shape of the gel framework. The resultant wet gel was allowed to sit on the bench top for 12 hours to yield the Ag₂Se wet gel. 4mL of methanol was subsequently used to wash the obtained Ag₂Se wet gel 4-5 times per day for two days to remove excess Ag⁺ ions and Cd²⁺ ions that diffused out from the initial CdSe gel. The purified Ag₂Se wet gel was exchanged with acetone and then dried with supercritical CO₂ to yield a Ag₂Se aerogel. The drying process followed the procedure described for the CdSe aerogel (Chapter 2, Section 2.2.3).

4.2.3 Synthesis of PbSe and CuSe Gels and Aerogels

PbSe and CuSe gels and aerogels were prepared similarly to Ag₂Se with the following differences: Pb(NO₃)₂ and Cu(NO₃)₂ methanolic solutions were used for the corresponding ion-exchange reactions and exchange was conducted for up to 24 hours. PbSe gels were washed using a methanol/water mixture (2:1 v/v). CuSe gels were washed with pure methanol.

4.3 Results and Discussion

4.3.1 Synthesis of Ag₂Se, PbSe and CuSe aerogels

CdSe nanoparticles, thiolate-exchanged nanoparticles, and wet gels resulting from

oxidative decomplexation were synthesized according to literature methods.³⁴ The ion exchange reaction was conducted by adding a methanolic solution of AgNO_3 to a monolithic CdSe wet gel without disturbance of the gel framework. The orange color of the CdSe gel turned black immediately upon adding the Ag^+ solution. After a few hours, the exchanged wet gel was solvent exchanged with methanol to remove excess Ag^+ ions and exchanged Cd^{2+} ions and then with acetone. The acetone-infused gel was then subjected to supercritical CO_2 drying. As shown in Figure 4.1, the monolithic wet gel framework (left) was retained all through the exchange (middle) and drying (right) processes, suggesting the dominant process in the exchange is limited to diffusion of cations through the anion sublattice of the individual nanoparticle building blocks. The subsequent supercritical drying process allows solvent (liquid CO_2) to be removed from the pores without collapse, thereby producing a dry gel of similar volume and monolithic shape to the wet gel (i.e., an aerogel).

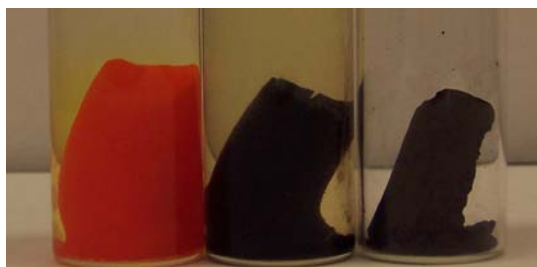


Figure 4.1 Photograph of initial CdSe wet gel (left), Ag^+ exchanged CdSe wet gel (middle), and resultant Ag_2Se aerogel (right). Reproduced with permission from ref ¹³¹. Copyright 2009 American Chemical Society.

Cation-exchange reactions of CdSe wet gels with Pb^{2+} and Cu^{2+} take longer time than that required for the Ag^+ exchange reaction as it has been observed the ion-exchange

processes for PbSe and CuSe gels were much slower than the case for Ag₂Se gels. Similar monolithic shape was retained all through the exchange and drying process of PbSe and CuSe gels as was observed in Ag₂Se gels, indicating similar diffusion mechanism govern these cation exchange reactions.

4.3.2 Physicochemical Properties of Ag₂Se, PbSe and CuSe Aerogels

4.3.2.1 Crystal Structure

The phase and crystallinity of the exchanged products were analyzed by powder X-ray diffraction (PXRD). When compared to the corresponding CdSe aerogel (Figure 4.2, A), the synthesized Ag₂Se aerogel adopts a body-centered cubic phase (α -phase) with Ag⁺ distributed over tetrahedral interstitial sites (Figure 4.2, B), distinct from the hexagonal CdSe precursor. The crystallite size of the Ag₂Se aerogel is calculated to be 3.6 nm (peak at 44°) by using the Scherrer equation, suggesting only modest crystallite growth has occurred relative to the corresponding CdSe aerogel, 2.8 nm (peak at 35°). The formation of α -Ag₂Se is notable because orthorhombic β -Ag₂Se is the thermodynamically stable form at room temperature. The intrinsic disordered cation lattice in α -Ag₂Se is associated with superionic conductivity,¹³⁴ which has precipitated efforts to stabilize this form at room temperature for potential battery applications. This intrinsic structural disorder may explain the breadth of the peak at 36° for the Ag₂Se aerogel, which is consistent with an amorphous component, and is also seen for Ag₂Se nanoparticles made from ion exchange of CdSe nanoparticles.⁴⁸

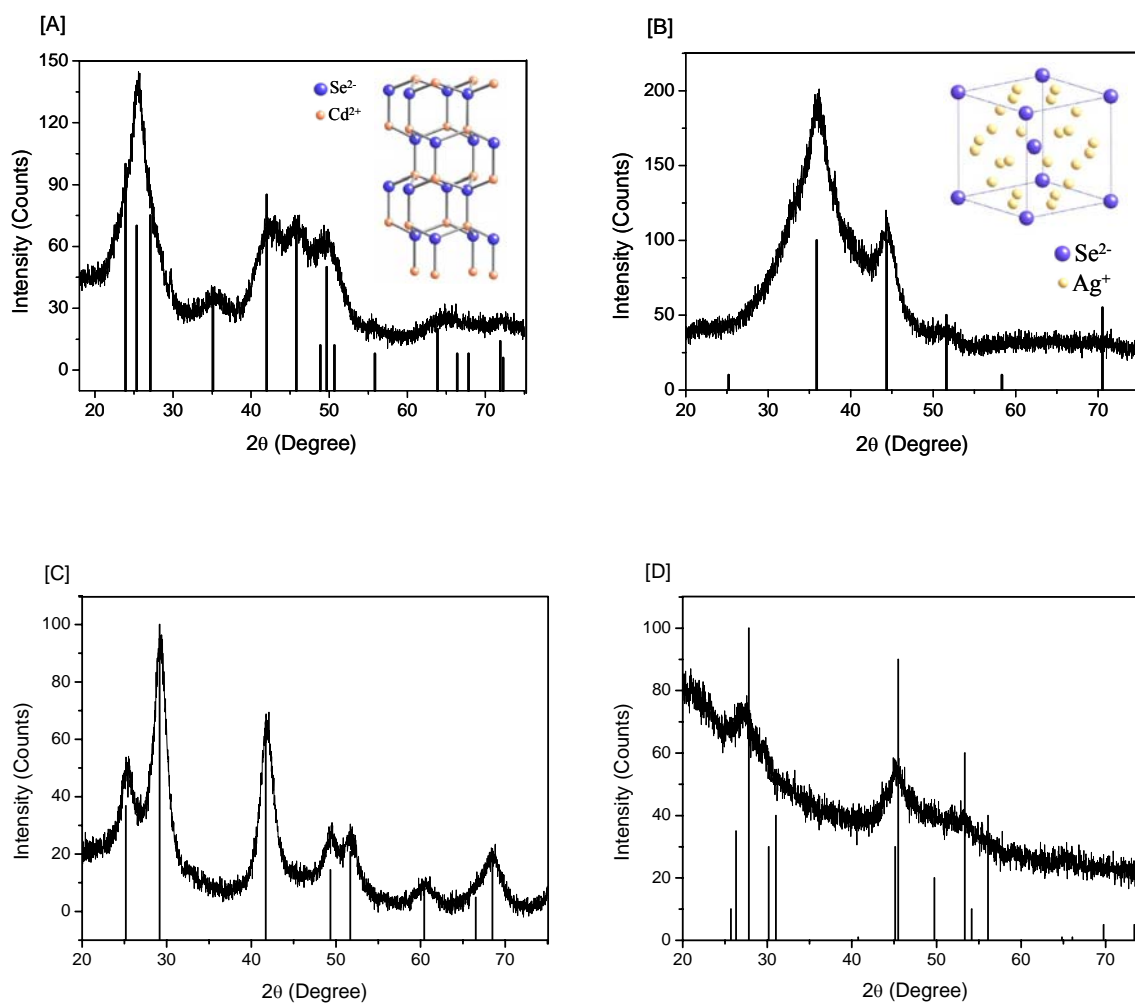


Figure 4.2 PXRD pattern of the CdSe aerogel [A], Ag_2Se aerogel [B], PbSe aerogel [C] and CuSe aerogel [D]. The ICDD-PDF overlays of hexagonal CdSe (PDF # 08-0459), cubic Ag_2Se (PDF # 27-0619), cubic PbSe (PDF # 78-1903) and hexagonal CuSe (PDF # 27-0185) are shown as lines in [A] through [D], respectively. The inset images show the crystal structure of hexagonal CdSe [A] and cubic Ag_2Se (cation sites partially occupied) [B]. Reproduced with permission from ref¹³¹. Copyright 2009 American Chemical Society.

In contrast, Pb^{2+} and Cu^{2+} exchange leads to the thermodynamic product in each case. The synthesized PbSe aerogel is highly crystalline and exhibits the cubic structure (Figure 4.2, C). The crystallite size of the PbSe aerogel was calculated to be 4.6 nm (peak at 42°), suggesting similar crystallite growth to that seen for Ag_2Se has taken place during Pb^{2+} exchange when compared to the primary CdSe system. The prepared CuSe aerogel adopts the hexagonal crystal structure (Figure 4.2, D). The crystallite size was not calculated because of the low intensity and high breadth of the reflections, but this material is clearly poorly crystalline.

4.3.2.2 Elemental Composition and Optical Characteristics

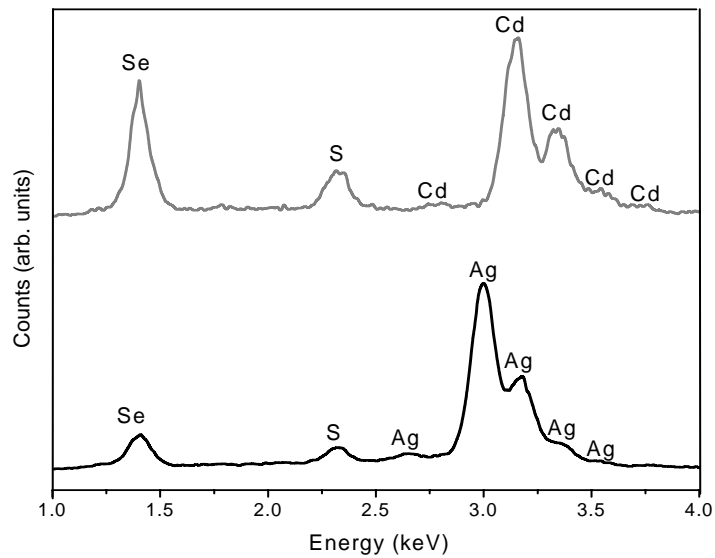
The completion of the ion-exchange process is confirmed by energy dispersive spectroscopy (EDS), UV/Vis/NIR absorption (converted from reflectance), and photoluminescence spectroscopy. EDS spectra of aerogels produced from supercritical drying of Ag^+ exchanged CdSe wet gels exhibit three dominant peaks corresponding to Ag, Se, and S. No Cd peak is observed (Figure 4.3). The atomic ratio of Ag/Se is 2:1, consistent with the formulation Ag_2Se (Table 4.1). A small amount of S is present, which we attribute to residual (i.e., unreacted) thiolate surface groups present in the gel (Table 4.1). The exchanged aerogel shows no absorption or emission of light in the range 500 to 800 nm, where the corresponding CdSe aerogels are optically active (Figure 4.4). Full exchange was also observed in PbSe and CuSe aerogels (Figure 4.3) with the atomic ratio of Pb/Se and Cu/Se determined to be 1: 1 in each case, consistent with the formulation of PbSe and CuSe, respectively (Table 4.1).

Table 4.1 Atomic ratios of CdSe, Ag₂Se, CuSe and PbSe aerogels obtained by EDS.

Sample	Atomic Ratio
CdSe	Cd : Se : S = 42.5 : 41.8 : 15.7
Ag ₂ Se	Ag : Se : S = 60.9 : 31.8 : 7.3
CuSe	Cu : Se : S = 44.4 : 38.9 : 16.9
PbSe ^a	Pb : Se = 50.8 : 49.2

^a Pb-L (10.550eV) and Se-K (11.220eV) lines were used for calculating the atomic ratio of Pb to Se in the PbSe aerogels. The content of S was not included in the calculation of atomic ratio due to the overlap of the S-K (2.307eV) line and the Pb-M (2.342eV) line.

[A



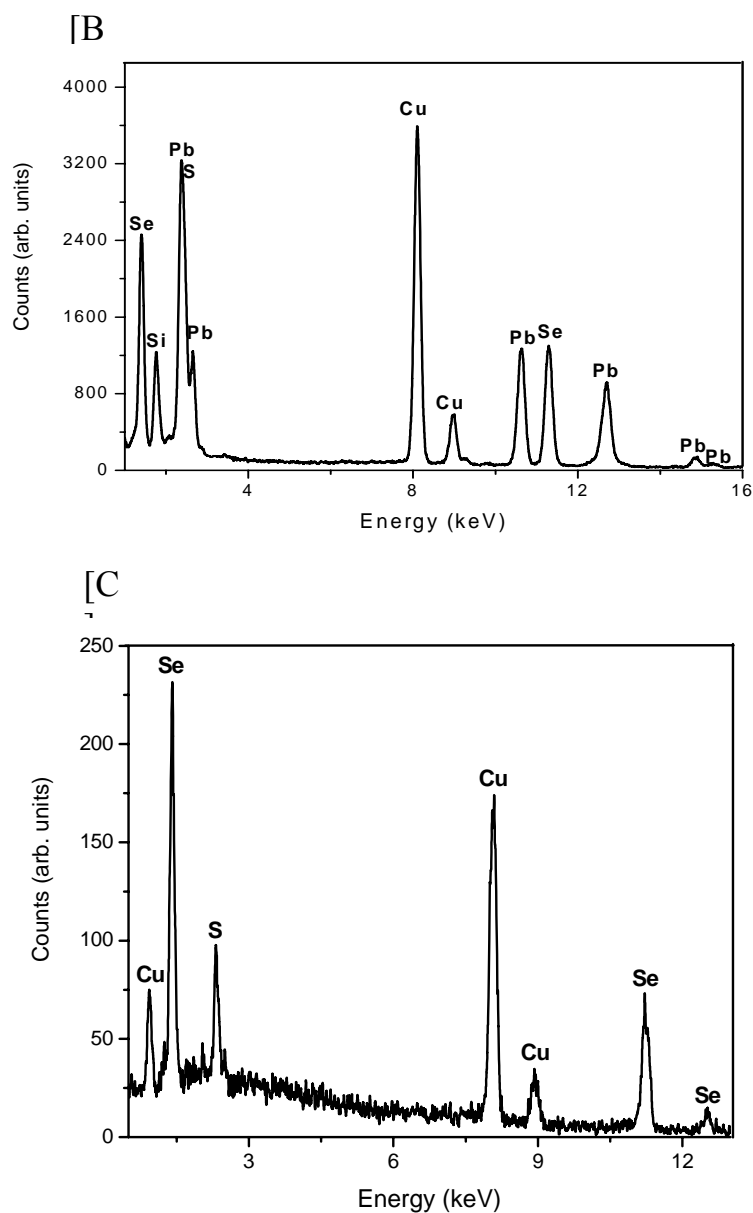


Figure 4.3 EDS spectra of aerogels of CdSe [A, top], Ag₂Se [A, bottom], PbSe [B] and CuSe [C]. EDS of PbSe was acquired by TEM/EDS, the rest of aerogels were analyzed by SEM/EDS. The presence of Si in the PbSe aerogel [B] is attributed adventitious dust and Cu is due to the copper grid upon which the PbSe sample was deposited for TEM measurements. Reproduced with permission from ref¹³¹. Copyright 2009 American Chemical Society.

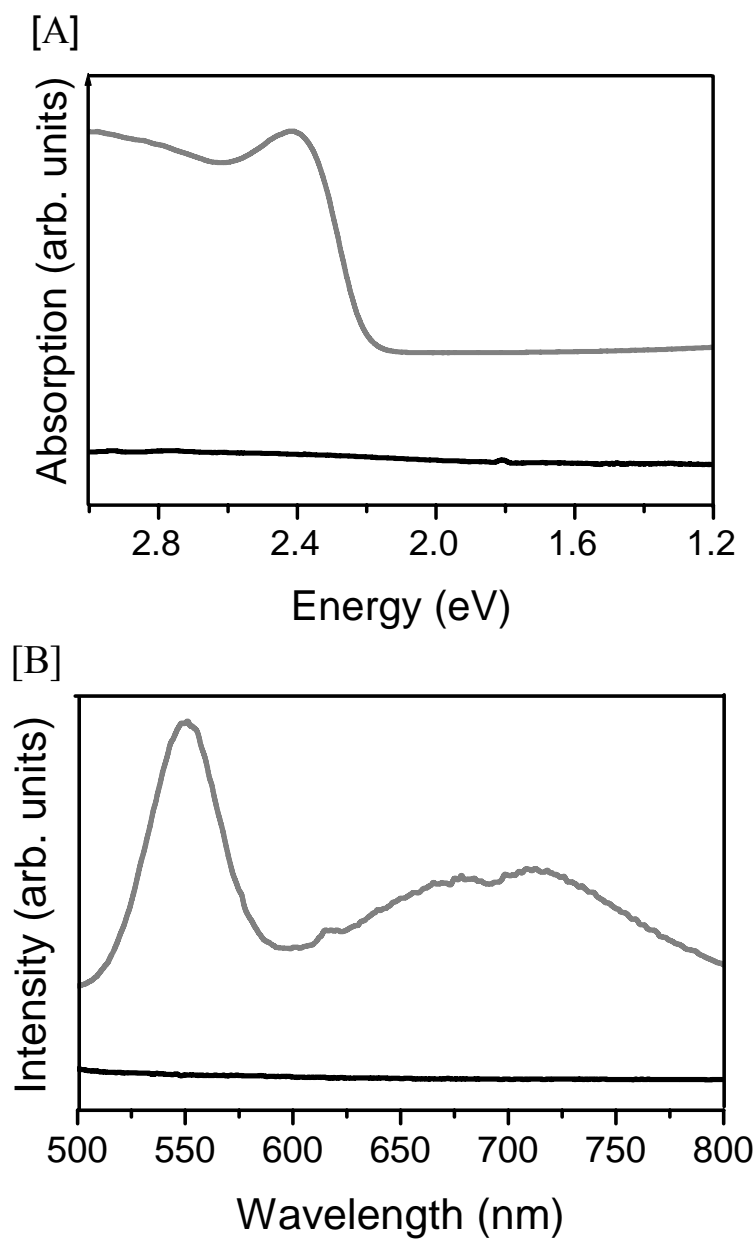


Figure 4.4 Optical absorption [A] (data converted from diffuse reflectance) and photoluminescence spectra [B] of the initial CdSe aerogel (top, grey) and Ag₂Se aerogel (bottom, black). Reproduced with permission from ref ¹³¹. Copyright 2009 American Chemical Society.

4.3.2.3 Morphology

The morphology of the cation-exchanged aerogels was studied by transmission electron microscopy (TEM) (Figure 4.5). The typical pearl-necklace morphology of colloidal aerogels is observed in all of the prepared aerogels. The primary nanoscale particles are clearly evident, and all aerogels exhibit a broad range of pores extending from the meso- (2-50 nm) into the macro- (>50 nm) porous regime.

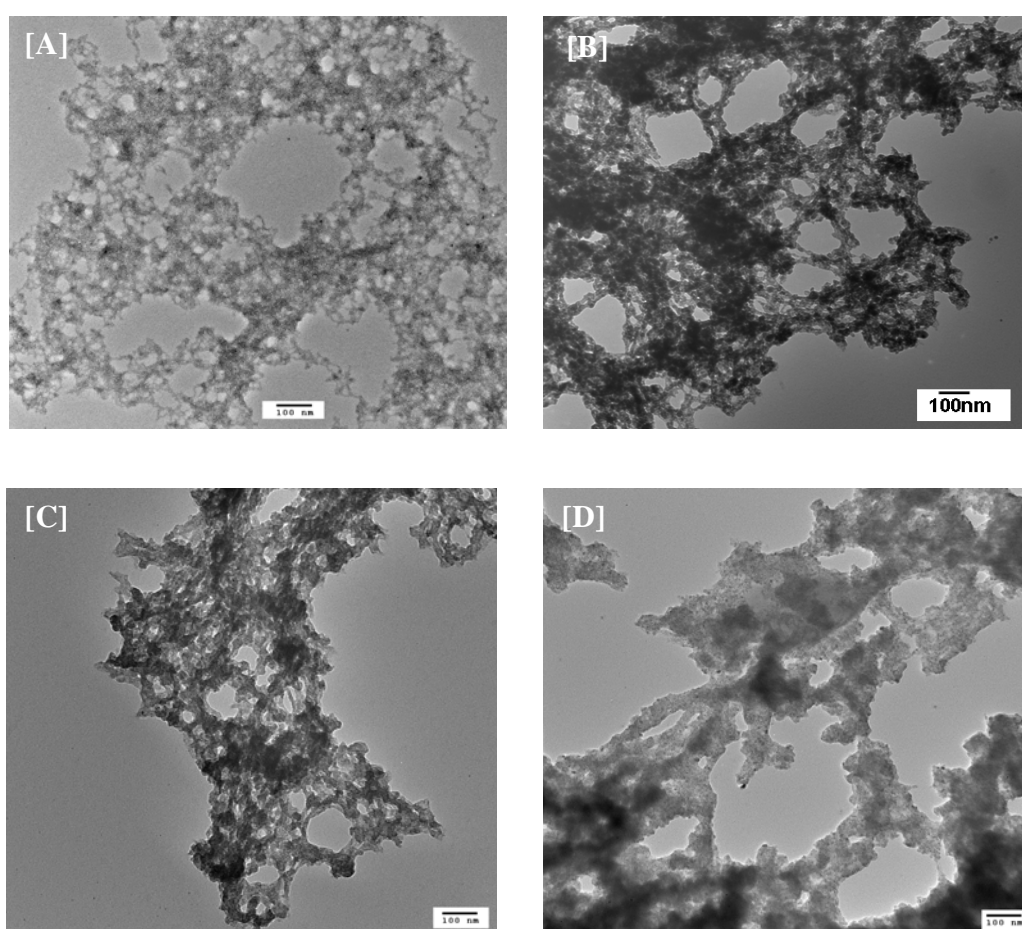


Figure 4.5 Transmission electron micrographs of CdSe [A], Ag₂Se [B], CuSe [C] and PbSe [D] aerogels. Reproduced with permission from ref ¹³¹. Copyright 2009 American Chemical Society.

4.3.2.4 Surface Area and Porosimetry Profile

The surface area and pore size distribution for Ag₂Se aerogels were determined by N₂ adsorption/desorption isotherms (Figure 4.6). The isotherms are similar to those previously observed for CdSe aerogels¹³⁰ as is the pore-size distribution (BJH) plot, which suggests a characteristically broad range of pores (2-120 nm), with a somewhat higher average pore diameter (Table 4.2).

Table 4.2 Porosimetry data for CdSe and Ag₂Se aerogel. Reproduced with permission from ref¹³¹. Copyright 2009 American Chemical Society.

Sample	BET surface area (m ² /g)	Silica equivalence BET surface area (m ² /g) ^a	BJH average pore diameter (nm)	BJH cumulative pore volume (cm ³ /g)
CdSe aerogel	133.1	423.9	16.0	0.58
Ag ₂ Se aerogel	111.7	547.8	22.4	0.69

^asilica equivalence surface areas were computed by converting the BET surface area for 1 mol of CdSe or Ag₂Se aerogel into that for 1 mol of SiO₂ using the respective compound formula masses.

The relatively low surface area for Ag₂Se compared to CdSe actually translates to a higher per mole surface area. This is shown when the equivalent surface area of silica (a “standard” aerogel phase) is computed for Ag₂Se and CdSe by considering the relative formula masses. Generally, in nanoparticle systems, smaller particles with higher surface/volume ratios give larger surface areas. However, the obtained Ag₂Se aerogel has larger per mol basis surface area than that of the CdSe aerogel even though the calculated

primary particle size of the Ag₂Se aerogel is larger than that for CdSe (3.6 nm vs. 2.8 nm). This can be explained by contributions from the pore structure of the gel network.

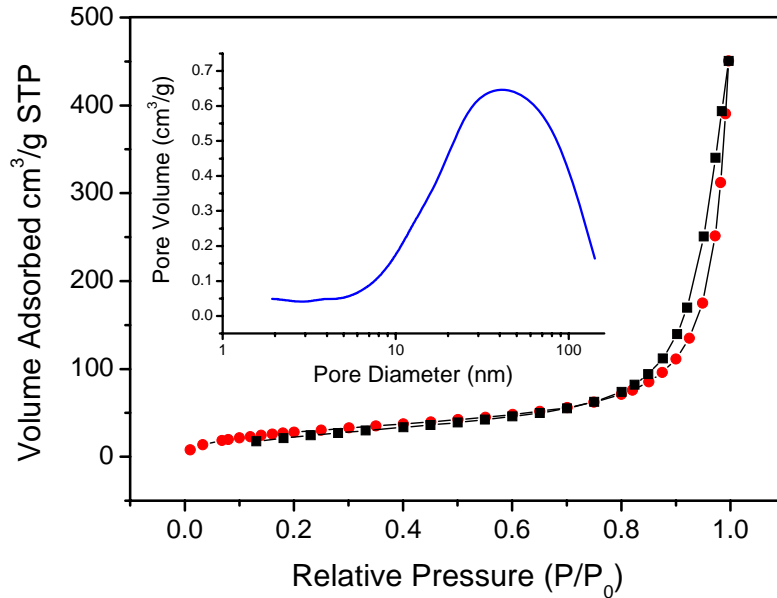


Figure 4.6 N₂ adsorption (filled circles)/desorption (filled squares) isotherms of an Ag₂Se aerogel. The inset shows the corresponding BJH modeled pore size distribution. Reproduced with permission from ref ¹³¹. Copyright 2009 American Chemical Society.

4.3.3 Partial Cation Exchange Reactions of CdSe Wet Gels

As mentioned in Section 1.3.4 of Chapter 1, cation-exchange reactions in nanoscale systems are not only thermodynamically favored, but also kinetically fast due to their substantially decreased activation energy barrier. In the exchange of CdSe gel by Ag⁺ ions, the cation exchange reaction is driven by a large thermodynamical force with a large difference in solubility (e.g., $K_{sp}=1.0 \times 10^{-33}$ and 3.1×10^{-65} for CdSe and Ag₂Se,

respectively). Additionally, by taking the advantage of the nanostructure property of the primary CdSe gel, Ag⁺-exchange reactions occur within seconds. Intriguingly, it was found this rapid exchange also enables exquisite control of composition on the macroscale, governed by the diffusion process through the gel network. Instead of exchanging just the surface of individual nanoparticle components, rapid and complete exchange is obtained within the diffusion zone. By control of the amount of exchanging ion added, partial cation exchange can be achieved, as shown in Figure 4.7, in which the outer surface of the gel body is transformed into Ag₂Se (black), while the core is still CdSe (orange).

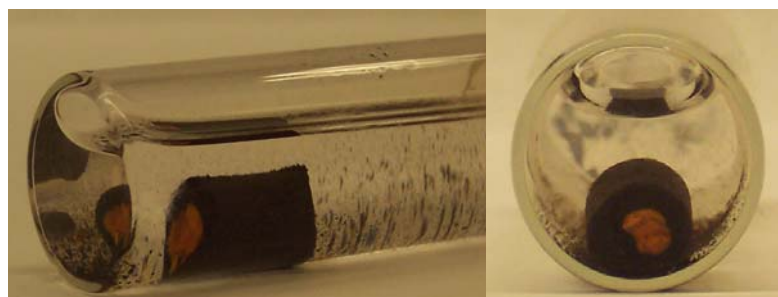


Figure 4.7 Photograph of a partially exchanged CdSe wet gel, sliced in two. Reproduced with permission from ref ¹³¹. Copyright 2009 American Chemical Society.

4.4 Conclusions

The present study shows that the cation-exchange reaction is a simple and efficient way to prepare Ag₂Se, PbSe and CuSe wet gels and aerogels from CdSe gel precursors. The striking similarity in crystallite size, morphology, and surface area characteristics supports a mechanism in which the bonding within the gel network remains globally unchanged, even as the structural attributes of the nanoparticle components are undergoing a dramatic

transformation. The obtained fully converted Ag_2Se aerogel has potential applications in batteries and electronic sensors, considering that $\alpha\text{-Ag}_2\text{Se}$ exhibits superionic conductivity,¹³⁴ and these can be expected to benefit from a nanostructured formulation with a large interfacial surface area. The newly prepared PbSe and CuSe aerogels have potential applications in solar cells, IR detectors and photovoltaic absorbers. The partial ion-exchange mechanism opens the door to making heterogeneous composite aerogels that may be useful for applications requiring hierarchical nanostructured architectures.

CHAPTER 5

OPTICAL SENSING OF TRIETHYLAMINE USING CADMIUM SELENIDE AEROGELS

5.1 Introduction

In this chapter, we exploit the unique characteristics of chalcogenide aerogels for optical sensing by employing CdSe aerogels as the sensor and TEA as the analyte. TEA was chosen to enable direct comparison to prior work using CdSe nanoparticles.¹³⁵ Further, we show that freshly-prepared CdSe aerogels exhibit a linear concentration-dependent PL intensity response to triethylamine; whereas previously tested aerogels exhibit saturation behavior that can be modeled based on a Langmuir adsorption isotherm model. Additionally, we will show that the magnitude of response depends sensitively on the surface characteristics of the aerogel. Finally, we conclude with a discussion of insights achieved through the sensing experiments into the behavior of chalcogenide aerogels.

5.2 Experimental Section

All the chemicals used in this chapter are listed in Section 2.1 of Chapter 2.

5.2.1 Synthesis of CdSe Aerogels

The experimental procedures employed in the synthesis of CdSe aerogels followed the method previously developed by our group³⁴ and were described in Section 4.2.1 of Chapter 4. The method involves TOPO/TDPA capped CdSe nanoparticle synthesis followed by a thiolate-ligand exchange process to form MUA-capped CdSe nanoparticles. Wet gels are obtained via partial removal of thiolate groups by TNM oxidization, an acetone exchange

process is employed to remove the byproducts of the oxidation, and monolithic aerogels are produced by CO₂ supercritical drying of wet gels.

Surface modified aerogels were prepared by heating the as-prepared monolithic aerogel in vacuum or by pyridine washing of the wet gel surface prior to CO₂ supercritical drying. For the thermal ligand desorption, the as-prepared monolithic CdSe aerogel was loaded in a 1 cm diameter fused silica tube between thin layers of glass wool and heated under high vacuum at 100°C for 4 hours. The fused silica tube was then cooled to room temperature and sealed with parafilm in a glove box prior to performing the sensing experiment. Pyridine-washed aerogels were prepared by exchanging the solvent of the monolithic wet gel with pyridine 8-12 times over 4-5 days to remove the bulk of the residual thiolate surface groups. The resulting gel was exchanged with acetone before supercritical drying.

5.2.2 Gas Sensing Set-up

The experimental set-up for gas detection is shown in Figure 5.1. A 1 cm quartz cell with a screw cap was used as the sample holder for as-prepared and py-washed aerogels, whereas the vacuum-heated sample was analyzed directly in the fused silica tube in which ligand desorption was conducted. A monolithic CdSe aerogel, sandwiched between thin layers of glass wool to avoid gel movement upon introduction and switching of the gas, was placed in the cell. The sensing experiment was conducted by recording the change in fluorescence intensity at λ_{max} (determined independently for each aerogel sample) as a function of time when switching between argon and an argon/TEA mixture. The aerogel sample was purged with argon for one hour prior to the sensing experiment to obtain a stable

baseline. The experiments were carried out under ambient conditions (atmospheric pressure, room temperature). The TEA partial pressure equals the product of the fractional TEA flow rate and the TEA saturated vapor pressure at ambient conditions (0.075 atm). The total flow rate for all the measurements was controlled in the range of 50-100 mL/min. The percentage of the intensity change was calculated by dividing the intensity change observed for the analyte by the argon reference intensity level and multiplying by 100. After sensing, aerogels were re-examined by TEM, EDS, porosimetry, PXRD, XPS and IR to assess any changes in the material as a consequence of TEA introduction and removal.

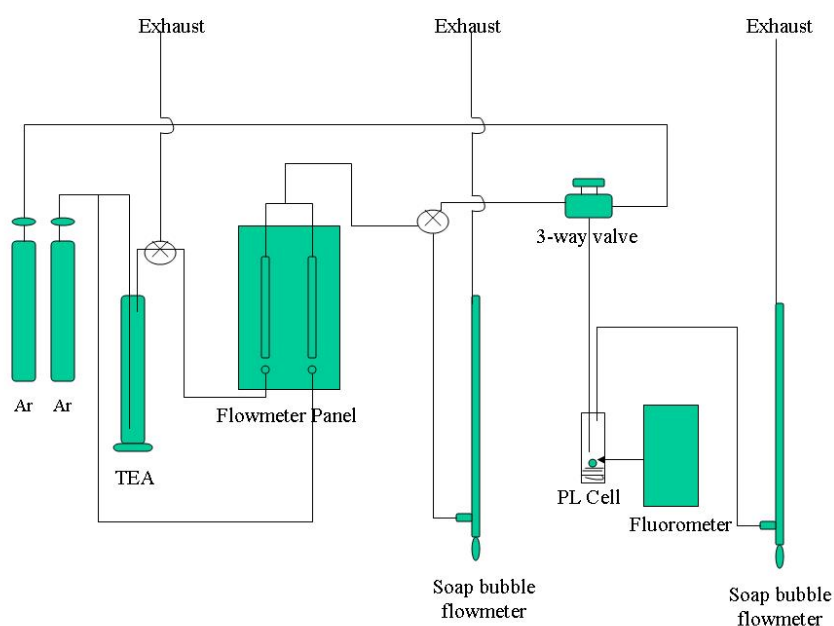


Figure 5.1. Experimental set-up for probing TEA sensing by CdSe aerogels. Reproduced with permission from ref¹³⁶. Copyright 2010 IOP.

5.3 Results and Discussion

5.3.1 Synthesis and Characterization of CdSe Nanoparticle Precursors and Aerogels

Spherical CdSe nanoparticle precursors capped with trioctylphosphine oxide (TOPO) and tetradecylphosphonic acid (TDPA) were prepared by a high temperature route following a published procedure¹³⁷ and the surface ligands were exchanged with 11-mercaptoundecanoic acid (MUA) under basic conditions. Aerogels were prepared by controlled oxidative decomplexation of surface thiolate ligands from the MUA-capped CdSe nanoparticles to yield a gel, followed by CO₂ supercritical drying to yield the aerogel.³⁴ The structural and optical properties of the CdSe nanoparticle precursors and aerogels are summarized in Table 5.1, and the surface area and average pore size for the aerogels is presented in Table 5.2.

PXRD analysis clearly shows that the aerogels retain the hexagonal CdSe phase of the nanoparticle precursors and that aerogel formation occurs without significant crystallite growth (Figure 5.2, Table 5.1). EDS spectroscopy conducted in the SEM yields compositional data for the nanoparticles and aerogel that are consistent with the expected stoichiometry (1:1) for CdSe (Table 5.1). The presence of sulfur (~17%) in the aerogel is attributed to the residual thiolate functionalities (MUA) on the aerogel surface after gelation, and the small amount of residual phosphorus (<2%) is attributed to TOPO/TDPA left over from the ligand exchange process (reduced from 20.0% in the as-prepared nanoparticles).

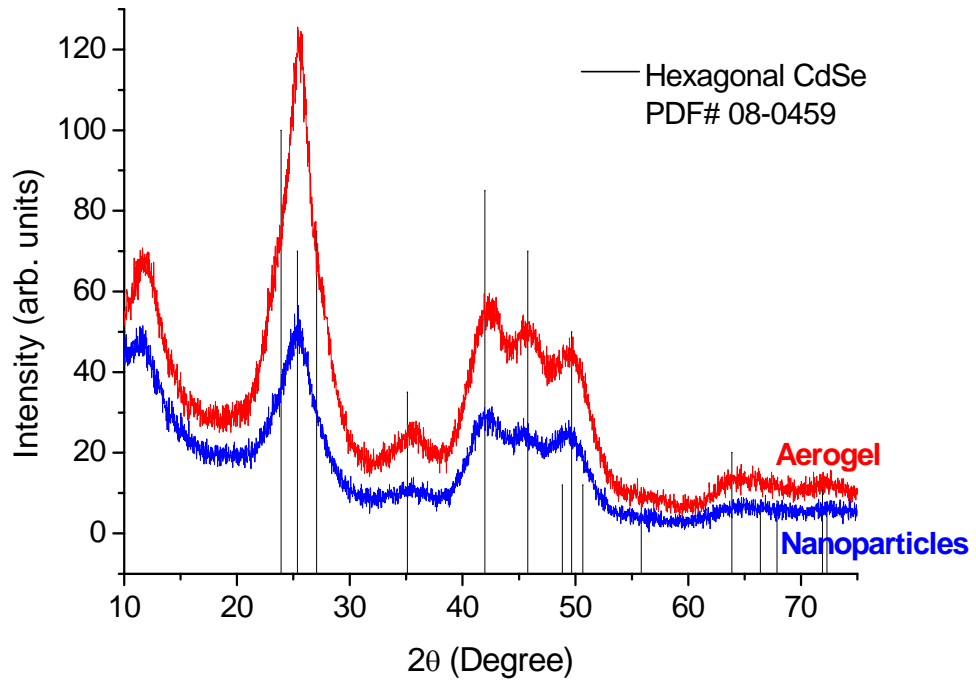


Figure 5.2. PXRD pattern of the CdSe nanoparticle precursor and resultant aerogels. The ICDD-PDF overlay of hexagonal CdSe (PDF # 08-0459) is shown as vertical lines. Reproduced with permission from ref¹³⁶. Copyright 2010 IOP

Table 5.1. Structure, crystallite size, elemental composition and optical properties of CdSe nanoparticle precursor and aerogel. Reproduced with permission from ref ¹³⁶. Copyright 2010 IOP

Material	TOPO/TDPA Capped CdSe Nanoparticle Precursor	CdSe Aerogel
Structure	Hexagonal CdSe	Hexagonal CdSe
Crystallite size (PXRD) ^a	3.9 ±0.3 nm	4.0 ±0.3 nm
Elemental composition in atomicpercentages (SEM/EDS) ^b	Cd 40.9	Cd 40.1
	Se 39.1	Se 40.8
	P 20.0	P 1.6
		S 17.5
Absorption band onset	561 nm	556 nm
Chromophore size ^c	5.2 nm	5.1 nm
Band-edge emission	537 nm	548 nm
Trap-state emission		615 nm- 715 nm

^a Crystallite sizes were calculated by applying the modified Scherrer formula ¹³⁸ to the (110) peak of nanoparticles and aerogels. The value represents an average from three independent samples and the error is the standard deviation.

^b Cd-L, Se-L, S-K, and P-K lines were used for calculating the atomic ratio in the nanoparticles and aerogels.

^c The chromophore size was calculated from the absorption band onset using the mass approximation model.¹³⁹

The band gap values of the aerogel and precursor nanoparticles are 2.23 eV and 2.21 eV, respectively, estimated from the absorption onsets (figures available in supplementary data), and both are significantly higher than that of bulk CdSe (1.74 eV) consistent with quantum confinement. Based on these values, the particle chromophore size can be computed from the mass approximation model¹³⁹ yielding sizes that are slightly larger (~25%) than indicated by application of a modified Scherrer equation¹³⁸ to PXRD data (Table 5.1). This is attributed to inaccuracy in the dielectric constant employed in the mass approximation model as well as the fact that this model does not take into account surface structure and electronic state coupling.¹⁴⁰ However, the Scherrer equation may underestimate average crystallite size if the sample is polydisperse or strain plays a role.¹⁴¹ Nevertheless, previous data on CdSe aerogels wherein TEM data were also analyzed suggest that the Scherrer equation is a better approximation to the actual crystallite size for CdSe aerogels.³⁴ Both nanoparticles and aerogels show a sharp peak in the PL near the absorption onset (Figure 5.3) attributed to band edge emission.^{34, 142} The presence of a broad trap state emission in the aerogel is ascribed to the residual thiolate capping ligands on the the aerogel surface acting as hole traps.¹⁴³ The surface area and the pore size distribution of the CdSe aerogels obtained from nitrogen adsorption/desorption isotherms (Figure 5.4) indicate the as-prepared CdSe aerogel has a high surface area and a broad range of pores extending from the meso- (2 – 50 nm diameter) into the macro (> 50 nm diameter) - regime, as expected for the aerogel architecture, with an average pore size of ca 16 nm.

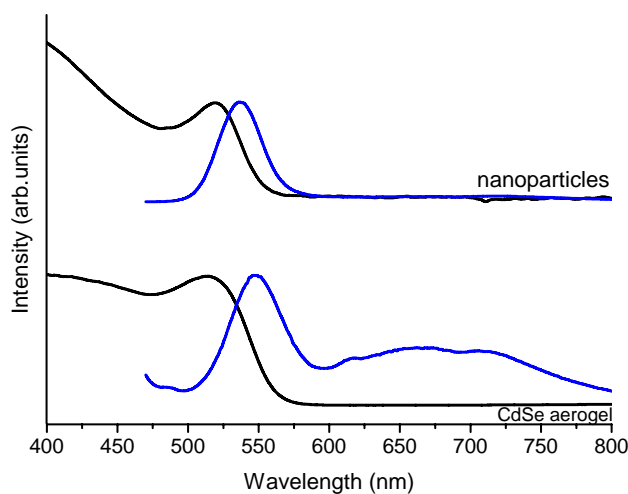


Figure 5.3 Optical absorption and photoluminescence spectra of CdSe nanoparticles (TOPO-capped) and the corresponding aerogel (excitation wavelength: 450 nm). Reproduced with permission from ref ¹³⁶. Copyright 2010 IOP

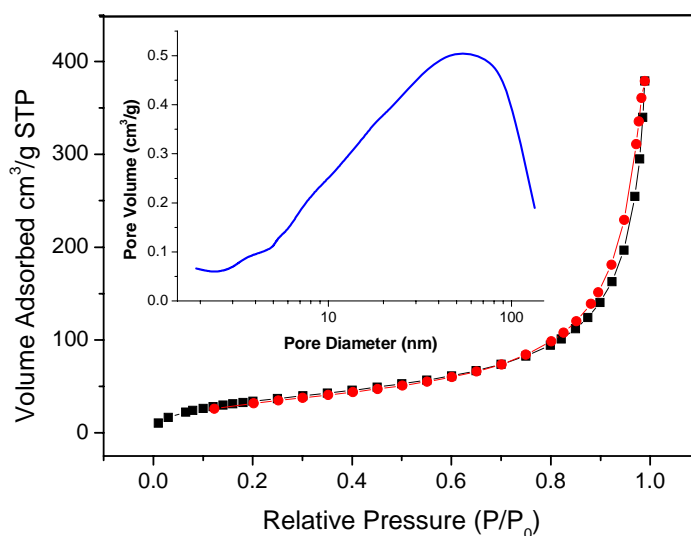


Figure 5.4 N₂ adsorption (filled circles)/desorption (filled squares) isotherms of a typical CdSe aerogel. The inset shows the BJH modeled pore size distribution. Reproduced with permission from ref ¹³⁶. Copyright 2010 IOP

5.3.2 PL Response of CdSe Aerogels to TEA

The PL response of CdSe aerogels to vapor-phase TEA was investigated in both static and kinetic mode using a gas sensing setup (Figure 5.1). When the ambient surrounding the CdSe aerogel monolith is switched from argon to dilute TEA (partial pressure: 0.007 atm), the luminescence intensity increases significantly compared to the argon reference level (Figure 5.5a) and this increase occurs throughout the spectrum. Because the enhancement occurs in both band-edge and trap-state emission, the intensity change cannot be simply attributed to removal of mid-gap trap states by replacement of residual thiolate ligands on the aerogel surface. Instead, we presume the majority of the TEA is occupying “vacant” sites, or displacing physisorbed gas molecules (Ar in this case), leading to a decrease in the thickness of the non-emissive surface dead-layer or a decrease in the extent of band-bending at the nanoparticle surface,¹⁴⁴ and therefore resulting in a lower degree of non-radiative recombination. It is important to note that the presence or absence of an emissive dead layer (and/or extent of band-bending) is not expected to impact the extent of quantum confinement in the nanocrystal (i.e., the energy gap between valence band and conduction band), only the probability of radiative recombination events (i.e., the intensity of the emission). Our results are consistent with the data put forth by Meyer *et al.*, in which the degree of emission enhancement depends on the electron donating ability of the Lewis base analyte, and thus, the energy match between the donating levels of the ligand and the accepting levels of CdSe.¹⁴⁵ In addition to single crystals, this model has also been successfully applied to CdS nanoparticle-Lewis base interactions in solution.¹⁴⁶ In the present case, the replacement of Ar by TEA leads to a lower degree of perturbation of the electronic structure of the interface relative to the nanoparticle interior (i.e., the surface

behaves more like the bulk solid), reducing the band-bending at the surface, without otherwise affecting the energy of the emissive states.

Analysis in kinetic mode shows the >30% increase in intensity in the PL of CdSe aerogels when exposed to TEA is largely reversible, as shown in Figure 5.5b (monitoring at peak maximum: 538 nm), when the minor slope change in the background is taken into effect. The saturation and recovery requires several minutes. While this is relatively slow compared to other aerogel sensors,^{114, 115, 147, 148} it is comparable to the observation of Meyer *et al.* for trimethylamine (TMA) binding to CdSe single crystals and to Nazzal *et al.* for binding of TEA to photoactivated polymer-embedded CdSe nanocrystals. The slow response of CdSe (noted by Meyer *et al.*) towards TMA relative to ammonia or methylamine (which achieve saturation within seconds) has been attributed to steric effects, which can be expected to retard access of the analyte to available binding sites on the surface, particularly at high analyte concentrations.¹⁴⁵ In cases where the surface is not bare, the response is even slower. Thus, Nazzal *et al.* hypothesized that the more rapid response observed in photoactivated nanoparticles could be attributed to facilitated motion of TEA through the surface ligand monolayer by activating phonon modes.¹³⁵ Collectively, these data suggest that the response time for CdSe sensors, whether they are single crystals, nanoparticles, or aerogels, is fundamentally limited by the intrinsic sterics of the analyte. In the context of this observation, the response time to TEA of the CdSe aerogels is rapid and does not appear to be limited by the pore structure.

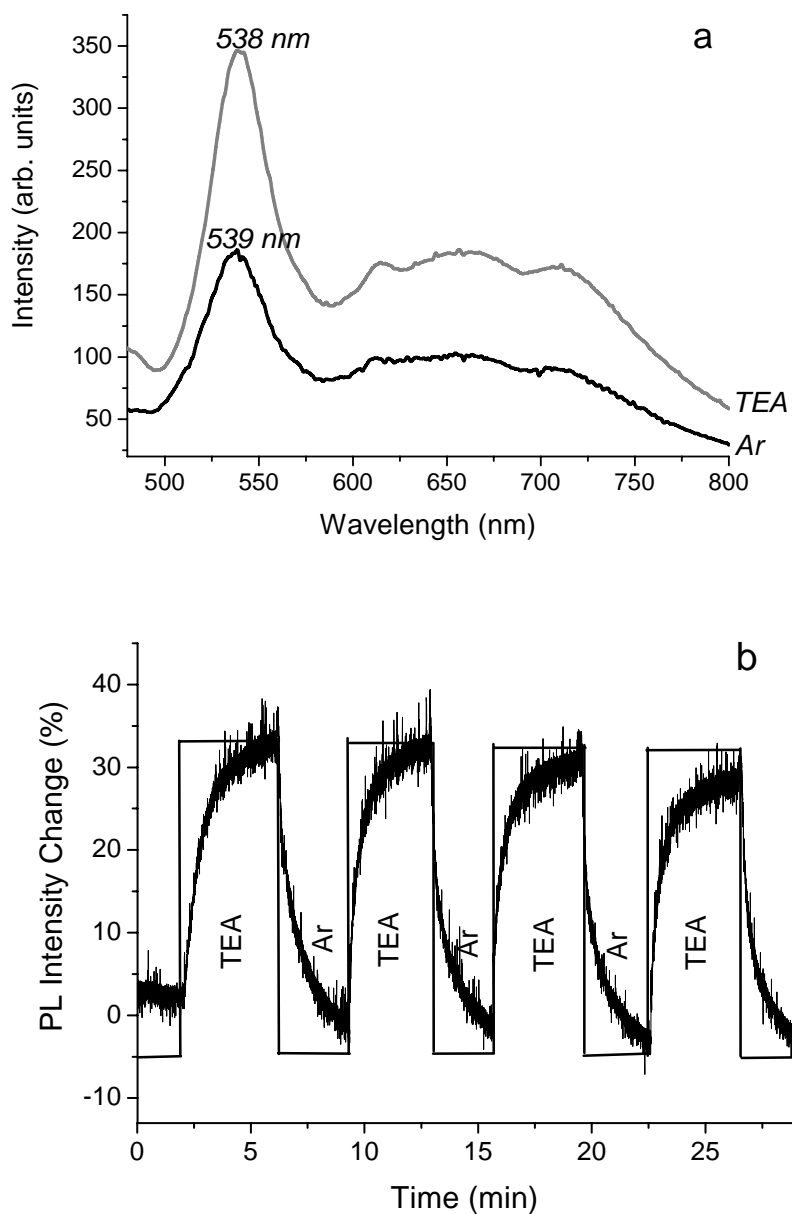


Figure 5.5 PL changes for as-prepared CdSe aerogels when alternating the exposure of aerogels to argon and TEA (a) static mode (b) kinetic mode. The sample was excited at 450 nm and the emission at 538 nm was monitored in the kinetic mode. The flow rate was 50 mL/min and the TEA partial pressure was 0.007 atm (TEA concentration: 7×10^3 ppm). Reproduced with permission from ref¹³⁶. Copyright 2010 IOP

5.3.3 Effect of Surface Treatment on Response

5.3.3.1 Thermal treatment.

As indicated above, thiolate capping groups are established hole-trapping agents for CdSe,¹³² introducing mid-gap trap states that result in a broad emission to the red and a concomitant decrease in the intensity of the band edge peak (Figure 5.5a). Concerned that the presence of the trap-state might reduce the sensitivity of the aerogel towards Lewis bases, we attempted to enhance the intrinsic band-edge PL by removing residual thiolate functionalities. In an attempt to thermally desorb residual capping groups (MUA), the aerogel sample was heated under high vacuum at 100°C for 4 hours. The PXRD of the heated aerogel is essentially identical to the as-prepared material (Figure 5.6); therefore heat treatment has no apparent impact on the structure or the crystallinity of the CdSe aerogel. EDS spectra of the heated CdSe aerogels reveal that the sulfur content is reduced from $17 \pm 0.4\%$ to $11 \pm 0.2\%$, suggesting partial loss of MUA from the gel surface during processing (Table 5.2). Moreover, the IR spectra of heated CdSe aerogels revealed a decrease in the intensity of the C-H stretching vibrations of the alkyl groups of MUA and the C-O-O⁻ stretching peak of the carboxylate group of MUA, compared to the as-prepared aerogels, confirming that MUA capping ligands were partially removed (Figure 5.7).

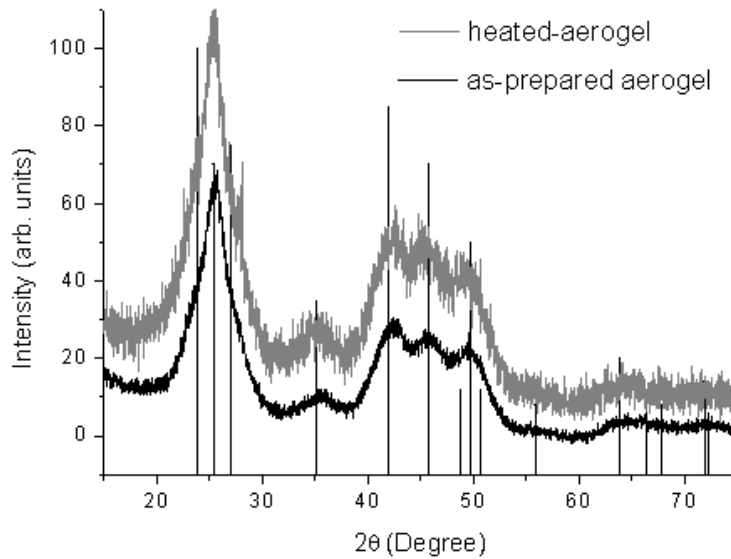


Figure 5.6 PXRD patterns of as-prepared and heated aerogels. The ICDD-PDF overlay of hexagonal CdSe (PDF # 08-0459) is shown as vertical lines.

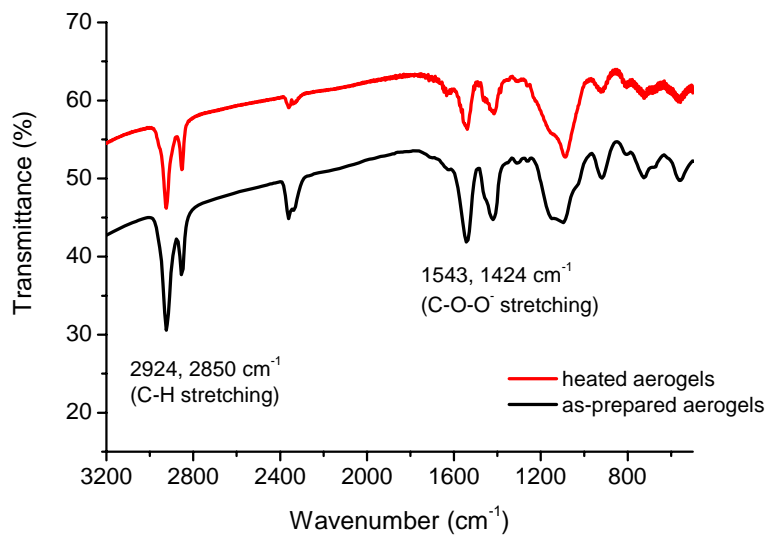


Figure 5.7 IR spectra of as-prepared (bottom) and heated (top) CdSe aerogels. Data were acquired using KBr pellets with identical weight percents of CdSe aerogel. Reproduced with permission from ref¹³⁶. Copyright 2010 IOP.

As demonstrated in Figure 5.8a, the heated aerogel sample demonstrates a significantly decreased PL intensity and a broadened band-edge peak relative to the as-prepared aerogel. Furthermore, the kinetic PL data (Figure 5.8b) shows no PL intensity change when alternating between TEA and argon, suggesting the thermal treatment has deactivated the sensor. While the origin of this effect is not clear, we hypothesize that after the thiolate capping groups were partially removed during heating, the exposed aerogel surface may have been more easily oxidized, possibly decreasing the amount of reaction sites on the surface for TEA bonding, and thereby passivating the surface. This suppressed PL intensity change phenomena was also observed in the discrete CdSe nanoparticles sensing study when the nanoparticles were preoxidized.¹³⁵

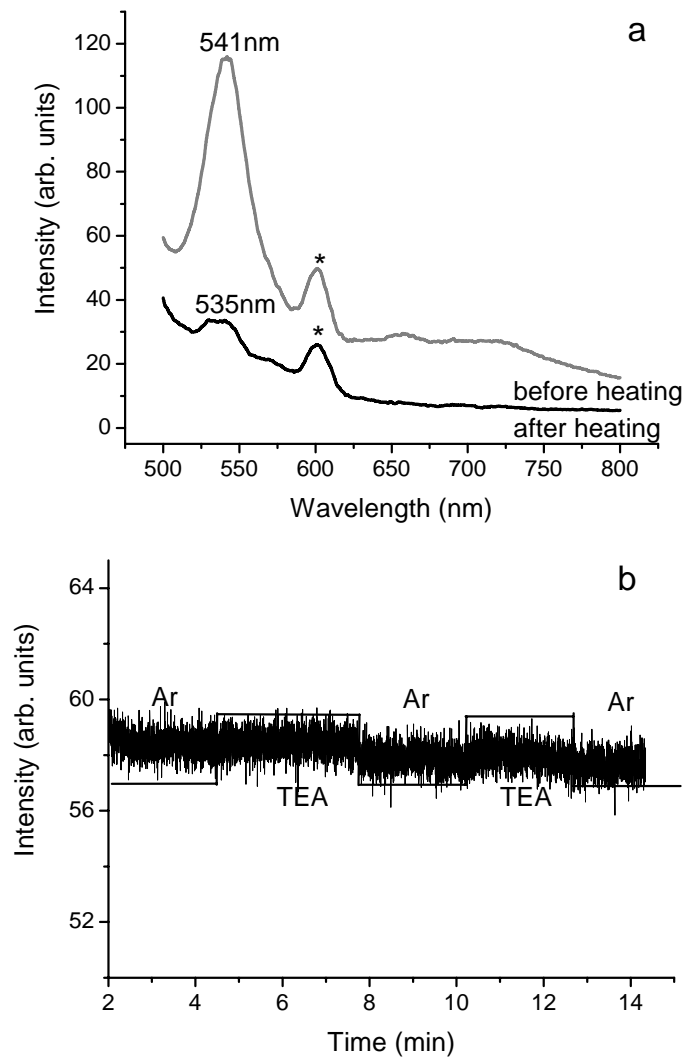


Figure 5.8 PL changes for vacuum annealed CdSe aerogels when alternating the exposure of aerogels to argon and TEA: (a) static mode, (b) kinetic mode. The peak at 600 nm in (a) marked with an * is due to the glass wool used to preclude movement of the aerogel sample during testing. The sample was excited at 450 nm and monitored at an emission wavelength of 541 nm in the kinetic mode. A flow rate of 100 mL/min and a TEA partial pressure of 0.075 atm (TEA concentration: 7.5×10^4 ppm) were employed. Reproduced with permission from ref¹³⁶. Copyright 2010 IOP

In order to assess whether oxidation occurs in the chalcogenide aerogel samples, XPS data were acquired on as-prepared and heated aerogels. Cd 3d spectra are identical for as-prepared and heated aerogels, with peaks at 405.3 eV ($3d_{5/2}$) and 412.0 eV ($3d_{3/2}$) corresponding nicely to the binding energy of a 3d Cd electron in CdSe (Figure 5.9a). There is no evidence of complex oxides containing Cd (e.g., CdSeO₃, expected to have a higher binding energy)¹⁴⁹ or CdO ($3d_{5/2}$ expected near 404 eV) in either sample. The Se 3d spectra likewise have a peak with a binding energy corresponding to Se²⁻ in CdSe (54.3 eV), but also have a small peak at 58.8 eV corresponding to SeO₂, and this is present in both samples (Figure 5.9b). The relative extent of oxidation in as-prepared and heated aerogels was assessed by measuring the areas of the peaks corresponding to SeO₂ and Se²⁻. The peak ratio of SeO₂ to Se²⁻ (0.062) in the heated samples was double that observed in as-prepared samples (0.031), suggesting a similar enhancement in oxide content. These data are consistent with a higher degree of surface oxide in heated samples, which may be responsible for the loss of sensor activity.

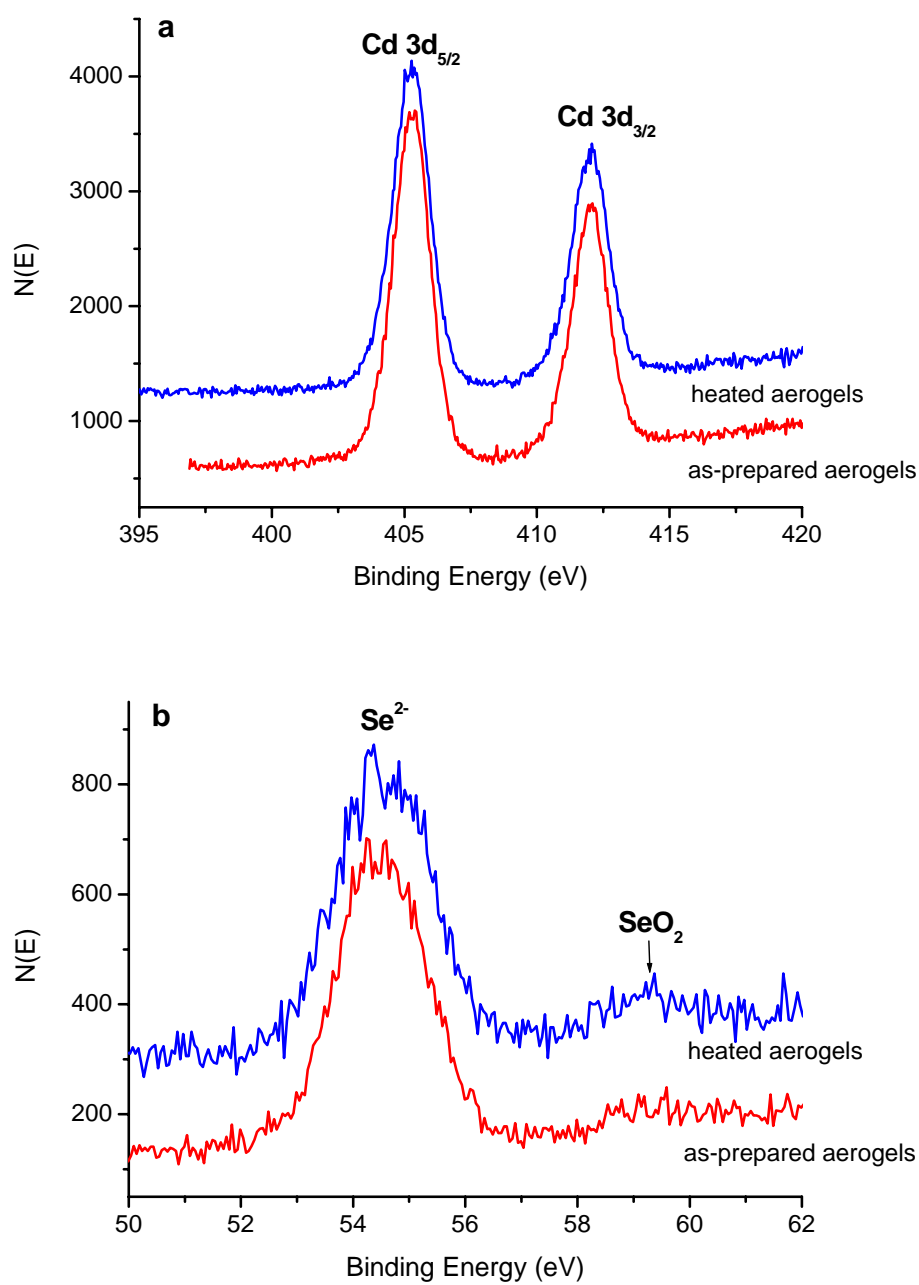


Figure 5.9 Cd and Se 3d regions of XPS spectra of as-prepared and heated CdSe aerogels.

Reproduced with permission from ref¹³⁶. Copyright 2010 IOP.

5.3.3.2. Pyridine Washing.

A previous study in our group demonstrated that pyridine washed aerogels show an increased ratio of band-edge to trap state PL intensity relative to as-prepared aerogels.³⁴ This is attributed to the fact that the pyridine washing process partially removes residual thiolates, which act as hole-traps. Additionally, if binding itself, pyridine is a good Lewis base that has a lower tendency to trap holes than thiolates.^{150, 151} Thus, we tested the PL response to TEA for pyridine washed aerogels to find out how the enhancement in band edge emission relative to trap state emission will impact the sensitivity to TEA.

As was the case for the heat-treated samples, PXRD analysis suggests the py-washed aerogel retains the same structure and crystallite size as the as-prepared aerogels (Figure 5.10). A reduction in sulfur content from $17 \pm 0.4\%$ to $8 \pm 0.3\%$ was found in the pyridine-washed CdSe aerogels by EDS measurement (Table 5.2), implying some loss of thiolate groups from the gel surface. Moreover, the IR spectra of pyridine washed CdSe aerogels show decreased C-H stretching and C-O-O⁻ stretching, also consistent with the loss of MUA (Figure 5.11).

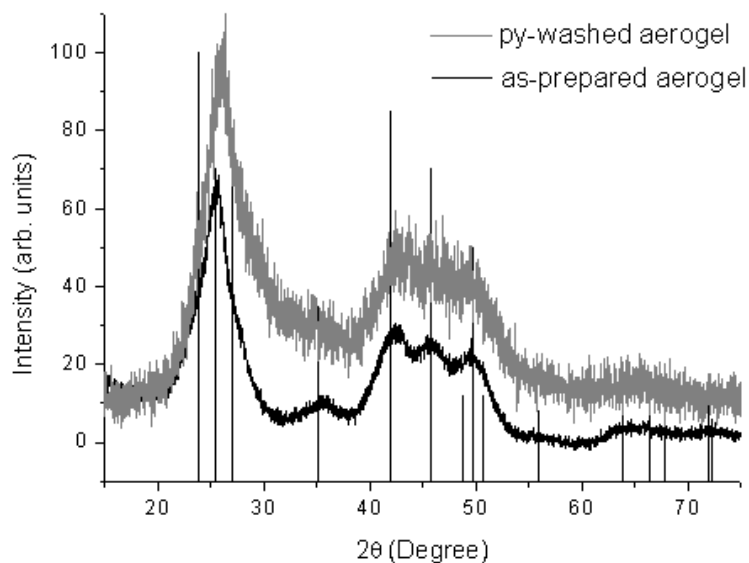


Figure 5.10 PXRD patterns of as-prepared and pyridine-washed aerogels. The ICDD-PDF overlays of hexagonal CdSe (PDF # 08-0459) are shown as vertical lines.

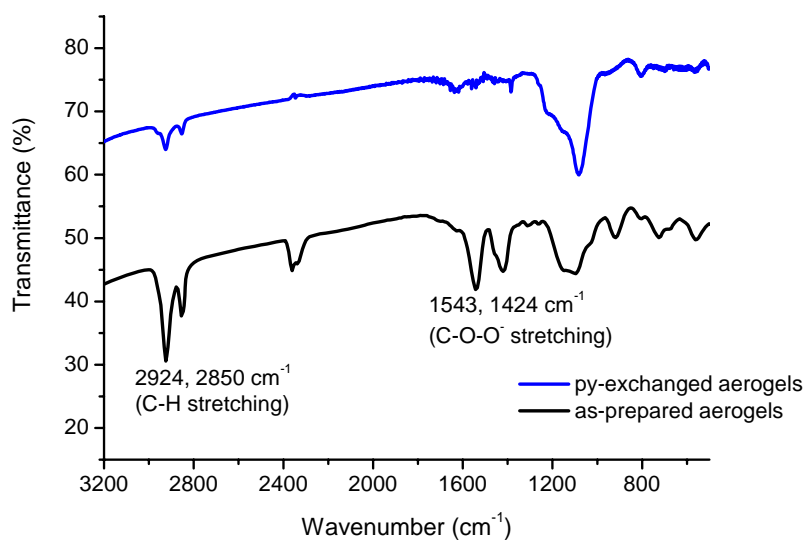


Figure 5.11 IR spectra of as-prepared (bottom) and pyridine-washed (top) CdSe aerogels. Data were acquired using KBr pellets with identical weight percents of CdSe aerogel. Reproduced with permission from ref¹³⁶. Copyright 2010 IOP.

As anticipated, the band-edge emission for the py-washed sample is enhanced. A significant blue shift of the peak position relative to the non-washed material was also observed in this work (Figure 5.12a). The blue-shifted emission may be due to the etching of the aerogel surface during the pyridine washing process or oxidation of the particle surface.^{135 150} Indeed, evaluation of EDS data suggests the materials are Cd deficient (Table 5.2) indicating Cd is etched in the pyridine washing process. Cd binding energy data suggests there is no inherent change in the Cd that is remaining (Figure 5.13a). However, an increase in the ratio of the SeO_2 peak to Se^{2-} in the pyridine washed materials (0.083) relative to as-prepared (0.031) (Figure 5.13b) indicates the surface selenide exposed from Cd loss is subject to oxidation. The kinetic studies (Figure 5.12b) show only a small (13.3%) but reversible change upon exposure to TEA, despite the fact that the partial pressure of TEA in this experiment is an order of magnitude larger than that used for the experiment in Figure 5.5. Given the fact that the basicity difference between TEA ($\text{pK}_b = 3.2$) and pyridine ($\text{pK}_b = 8.8$) is over 5 pK units, whereas TEA and MUA ($\text{pK}_b \sim 3$) are comparable, a more dramatic increase would be expected for the pyridine washed gels upon TEA introduction than for as-prepared aerogels with residual thiolates if the primary mechanism of sensing was by ligand displacement. Accordingly, the loss of sensitivity is instead attributed to a decrease in the number of available surface sites (Cd) for binding, either through etching or pyridine-binding, and/or an increase in the thickness of the surface dead layer due to oxidation.

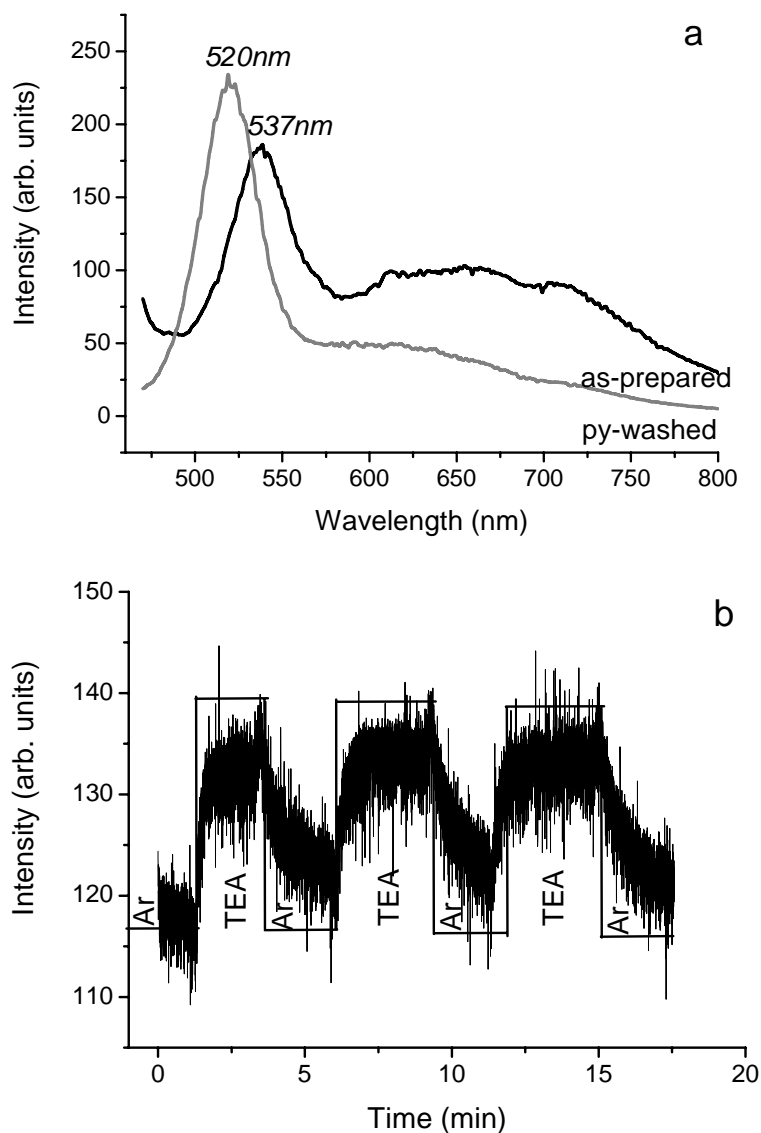


Figure 5.12 (a) PL spectra of the pyridine washed and as-prepared CdSe aerogel, (b) kinetic PL mode showing PL changes for the pyridine washed CdSe aerogels when alternating the exposure of aerogels to argon and TEA. The sample was excited at 450 nm and monitored at an emission wavelength of 520 nm. A flow rate of 100 mL/min and a TEA partial pressure of 0.075 atm (TEA concentration: 7.5×10^4 ppm) were employed. Reproduced with permission from ref¹³⁶. Copyright 2010 IOP.

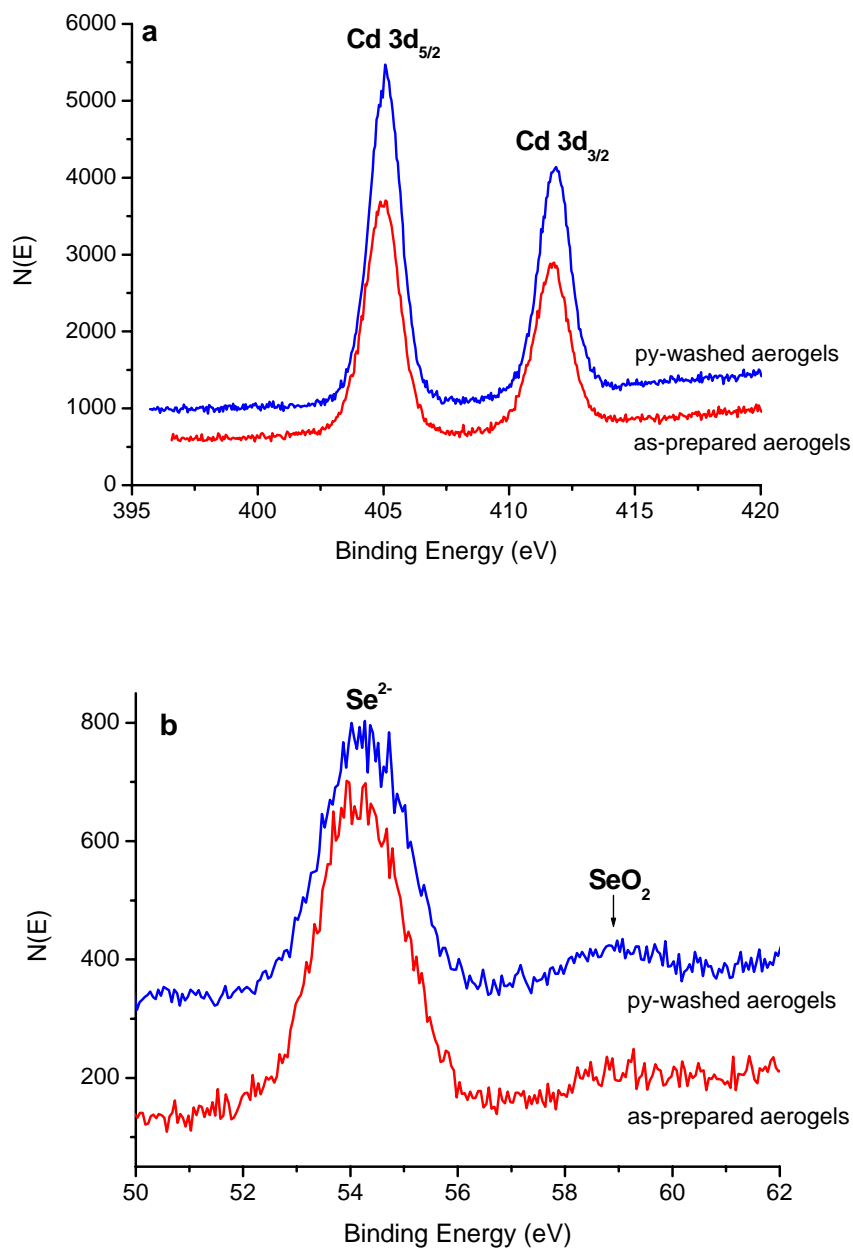


Figure 5.13 Se 3d regions of XPS spectra of as-prepared and pyridine-washed CdSe aerogels.

Reproduced with permission from ref¹³⁶. Copyright 2010 IOP.

Because the extent of oxidation in CdSe aerogels appears to be greater for the pyridine washed materials (which retain modest activity) than the heated materials (which are inactive), it is not possible to relate the activity simply to the extent of oxidation. Nor is the response proportional to the surface area of the aerogel (Table 5.2). Rather, the heat-treatment may enable formation of a uniform barrier layer by redistributing oxygen, leading to a uniform coverage of SeO_2 on a CdSe core, whereas pyridine washing and concomitant loss of Cd^{2+} ions may facilitate a patchwork of oxide that reduces, but does not eliminate, activity (i.e., some surface Cd^{2+} remains). Thus, the surface area measured by physisorption is not proportional to the “active” surface area (where chemisorption is the mechanism of operation).

5.3.4 Effect of Sensing Treatment on the Crystal Structure, Chemical Composition, Morphology and Porosity of CdSe Aerogels

The as-prepared, heated and pyridine-washed CdSe aerogels were characterized after sensing runs of one hour in order to evaluate the robustness of the aerogels to the sensing conditions. The crystallinity and structure by PXRD, morphology by TEM, extent of oxidation by XPS and ratio of Cd:Se (Table 5.2) is unaffected by the sensing process (please see Figure 5.14-16 for PXRD, TEM, and XPS Figures). However, key differences are observed in the S content, with losses relative to Cd of 20-25% (as-prepared and heated) and nearly 50% (pyridine washed), as shown in Table 5.2. Clearly, the process of treating the aerogel with TEA and/or Ar results in significant displacement of residual thiolates, although it is not clear whether this happens in the process of establishing a stable baseline (ca one hour under Ar) or continues during the sensing experiment (one hour under alternating Ar,

TEA).

Table 5.2. Elemental composition and porosimetry data for as-prepared, heated and pyridine-washed CdSe aerogels, pre- and post-sensing. Reproduced with permission from ref ¹³⁶. Copyright 2010 IOP.

CdSe aerogels	As-prepared		Heated		Pyridine-washed	
	pre-sensing	post-sensing	pre-sensing	post-sensing	pre-sensing	post-sensing
Elemental composition in atomic percentage (%) (TEM/EDS)	Cd 40.0	Cd 41.3	Cd 42.4	Cd 43.4	Cd 42.5	Cd 43.2
	Se 40.8	Se 42.1	Se 43.3	Se 42.5	Se 47.4	Se 48.0
	S 17.5	S 14.9	S 11.2	S 9.2	S 6.1	S 4.2
	P 1.6	P 2.1	P 3.5	P 4.9	P 4.1	P 4.6
BET surface area (m ² /g)	134	210	194	132	167	237
BJH average pore diameter (nm)	16.0	19.4	29.1	17.8	17.0	22.9
BJH cumulative pore volume (cm ³ /g)	0.58	0.94	1.35	0.63	0.67	2.1

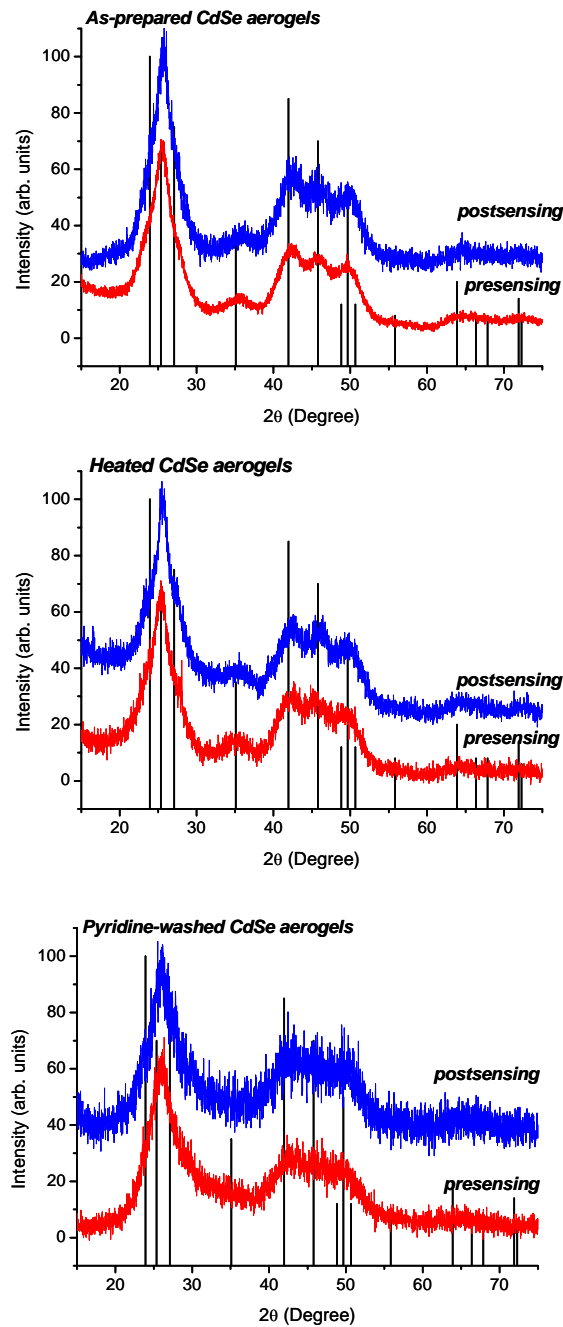


Figure 5.14 PXR D patterns of as-prepared, heated and pyridine-washed CdSe aerogels pre-sensing and post-sensing. The ICDD-PDF overlays of hexagonal CdSe (PDF # 08-0459) are shown as vertical lines. Reproduced with permission from ref¹³⁶. Copyright 2010 IOP.

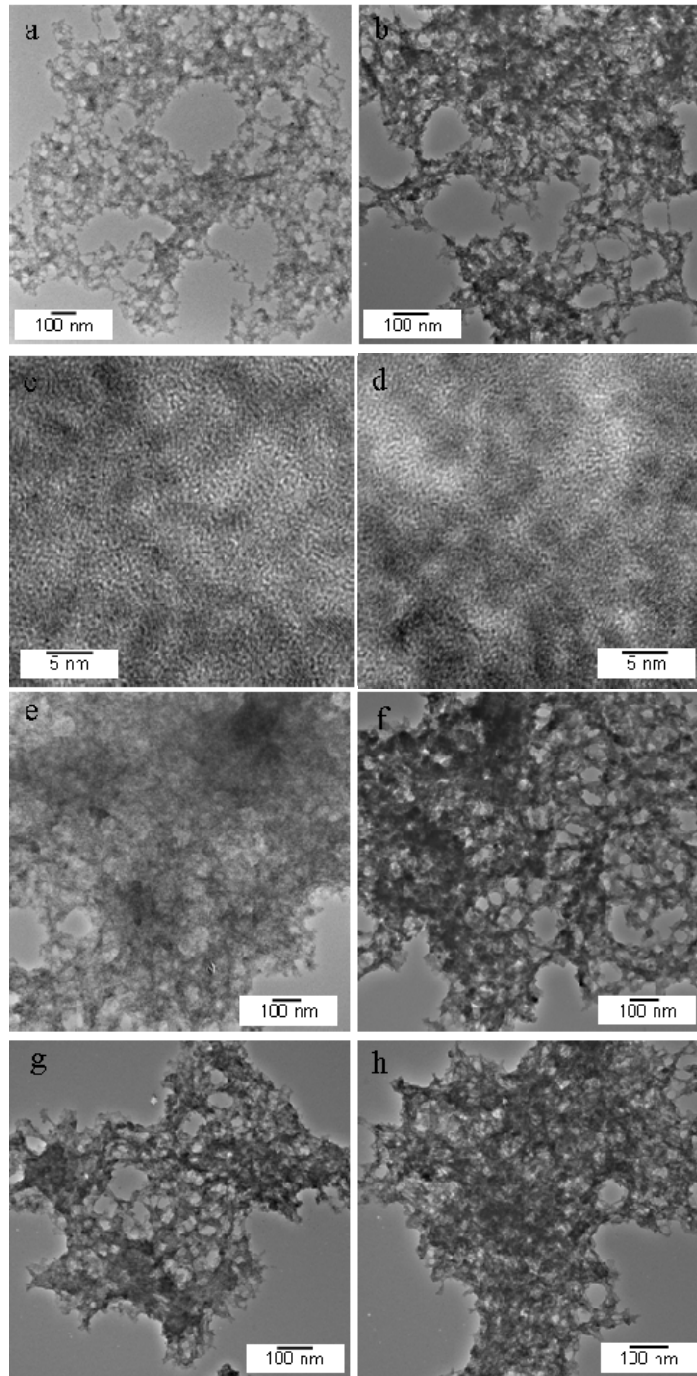


Figure 5.15 TEM micrographs of as-prepared (a, b, c, d), heated (e, f) and pyridine-washed (g, h) CdSe aerogels pre-sensing (a, c, e, g) and post-sensing (b, d, f, h). Reproduced with permission from ref¹³⁶. Copyright 2010 IOP.

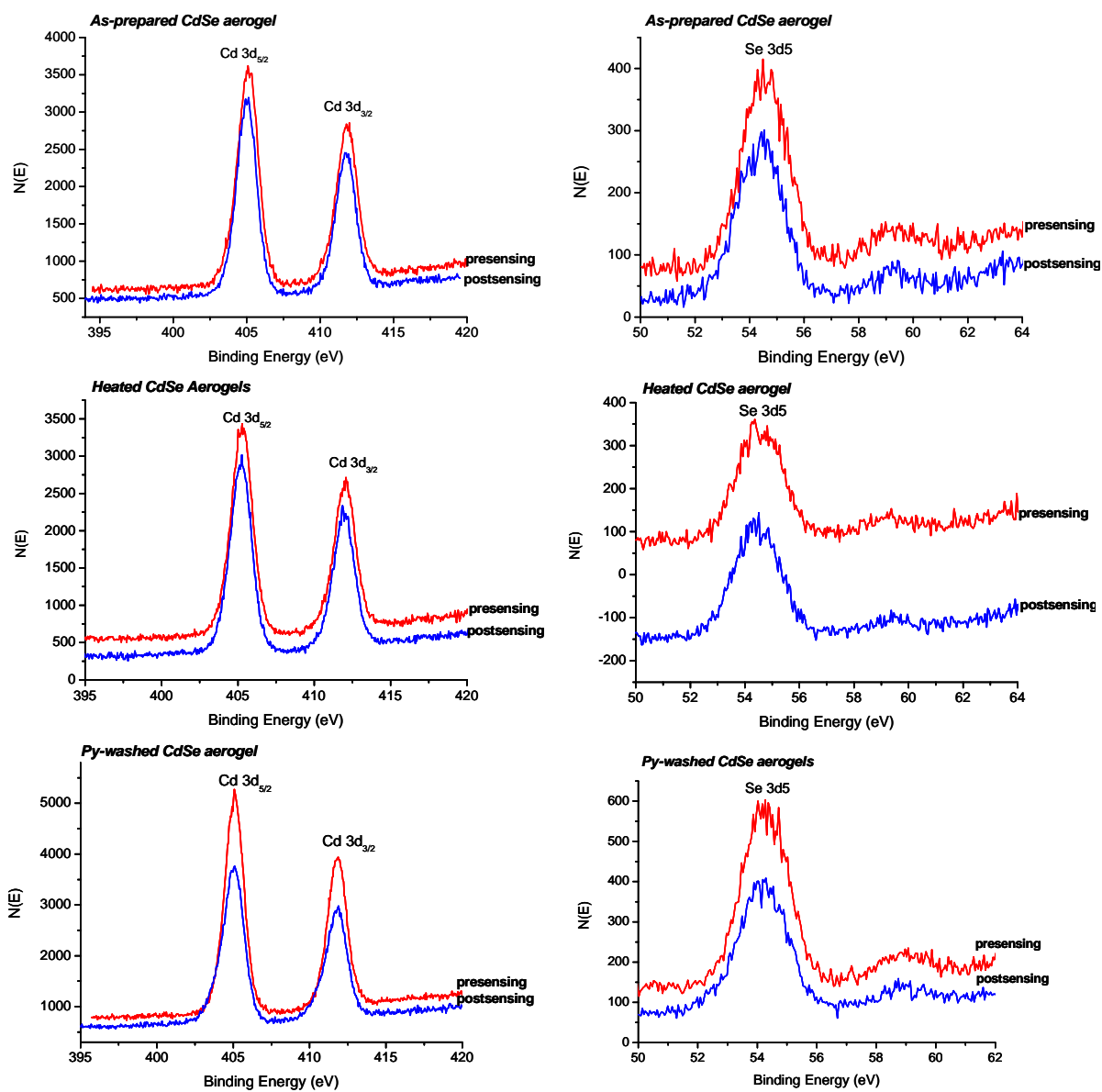


Figure 5.16 XPS spectra of as-prepared, heated and pyridine-washed CdSe aerogels pre- and post-sensing. The ionization at ca. 59 eV in the Se XPS corresponds to SeO₂. Reproduced with permission from ref¹³⁶. Copyright 2010 IOP.

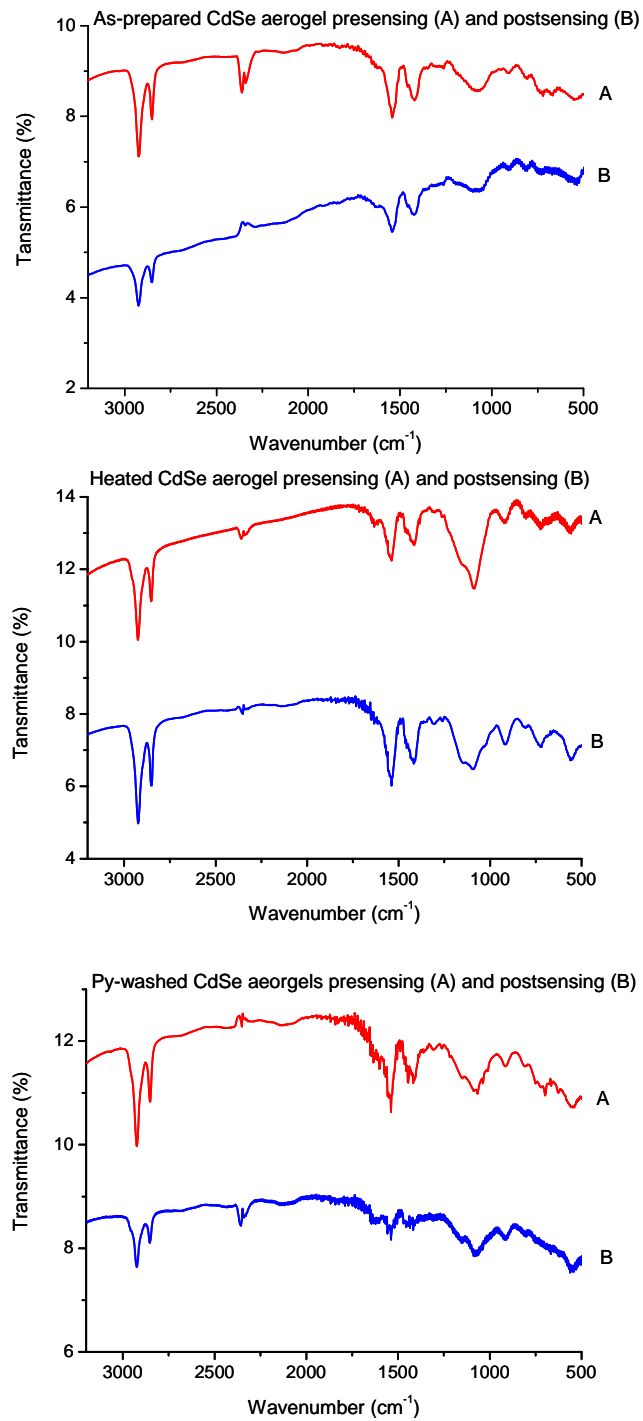


Figure 5.17 IR spectra of as-prepared, heated and pyridine-washed CdSe aerogels pre- and post-sensing. Reproduced with permission from ref ¹³⁶. Copyright 2010 IOP.

The loss of thiolates is also evident in the IR spectra of aerogels pre- and post-sensing (Figure 5.17) wherein decreases in the relative intensities of the C-H and C-O-O⁻ stretching are noted post-sensing. In the case of the as-prepared and pyridine-washed materials, the loss of thiolate results in a significant increase in surface area, arguing greater accessibility to the surface (Table 5.2). In contrast, the heated aerogel actually loses significant surface area in the sensing process. Presumably, the heat treatment, while removing residual ligands from the surface, also decreases the stability of the aerogel, so that addition and removal of TEA results in some degree of compaction.

5.3.5. Effect of TEA Concentration on PL Response

The TEA vapor pressure of 0.075 atm and a local ambient pressure of 1 atm produced a static concentration of 75,000 ppm. A series of TEA concentrations was obtained by online gas mixing experiments conducted by varying the relative flow rates of TEA/Ar and pure Ar. The PL intensity change as a function of TEA concentration is plotted in Figure 5.18a. The consistency of the aerogel response was tested by evaluating two independently prepared monolithic CdSe aerogels prepared under identical conditions (Sample A and B) in the range $4.7 \times 10^3 - 40 \times 10^3$ ppm (TEA partial pressure (P_{TEA}): 0.005–0.04 atm) and $4.7 \times 10^3 - 75 \times 10^3$ ppm (P_{TEA} : 0.005–0.075 atm), respectively. A linear change in PL intensity with TEA concentration was observed for both of the samples in the range tested. In the region where they overlap, the intensity change as a function of TEA concentration is nearly identical, showing the response is reproducible from sample to sample.

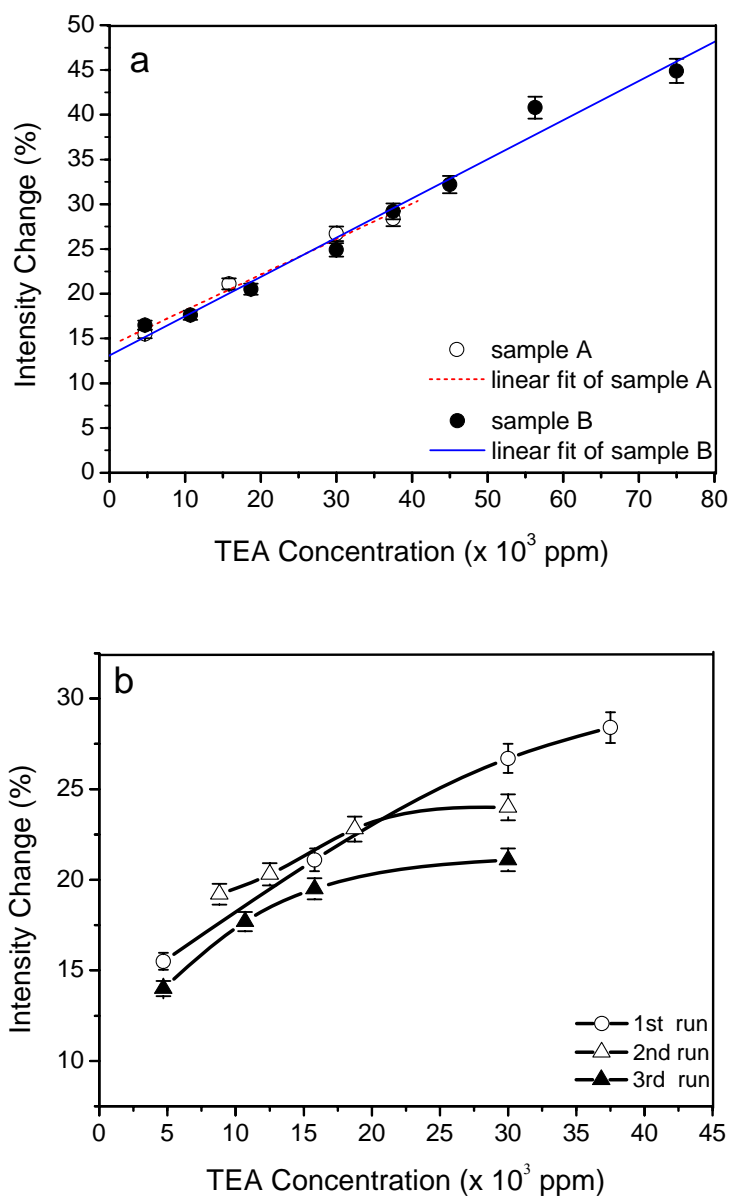


Figure 5.18 PL changes as a function of TEA concentration (a) for two independently prepared monolithic CdSe aerogels and (b) for the same monolithic aerogel sample (sample A) over three cycles. The flow rate was fixed at 100 mL/min. Reproduced with permission from ref¹³⁶. Copyright 2010 IOP.

However, we find that the sample history does affect the response. Thus, when sensing measurements were carried out twice more on the same monolithic aerogel (sample A) over the range 4.7×10^3 ppm - 40×10^3 ppm (P_{TEA} : 0.005 atm – 0.04 atm) (Figure 5.18b), we see a pronounced leveling as the concentration increases for subsequent runs relative to the fresh sample. This may indicate saturation of the adsorption sites on the aerogel surface. That is, despite the apparent reversibility of TEA adsorption, the process of adsorption and desorption does result in significant changes in the chemical nature of the interface over time, resulting in fewer active sites for TEA binding. Indeed, we know that the sensing experiment itself results in removal of residual thiolates (see IR spectra in Figure 5.17), thereby changing the response of the sensor over time.

5.3.6. Langmuir Adsorption Isotherms

In order to better understand the sensing process, we sought to model the data using Langmuir theory. The Langmuir theory applies to chemisorption situations and assumes only a monolayer formation of adsorbed molecules.¹²¹ The optical sensor used in our study is based on chemical interaction (chemisorption) between the aerogel surface and the Lewis base molecules, which is defined as adduct formation in this particular case. The observation of linear changes in PL with TEA partial pressure suggests that TEA molecule adsorption is confined to a monolayer. Therefore, for this preliminary investigation of CdSe aerogels as sensors, we hypothesize that Langmuir theory is applicable to the adsorption isotherm. and assume the fractional increase in PL intensity is proportional to the fraction of the surface covered by the amine, as described by Meyer *et al.*¹⁴⁵ This can be modeled using Equations 5.1 and 5.2

$$\theta = KP_A / (1 + KP_A) \quad (5.1)$$

$$1/\theta = 1 + 1/(KP_A) \quad (5.2)$$

where θ is the fraction of the surface covered by the amine, K is the equilibrium adsorption constant, and P_A is the partial pressure of the adsorbing gas. A linear double-reciprocal plot of θ^{-1} vs. P_A^{-1} should be obtained with a slope of K^{-1} , according to Equation 5.2.

Accordingly, Langmuir adsorption isotherms for multiply cycled sensors were constructed by plotting the fractional PL intensity increase (the individual intensity change normalized by the maximum intensity change at the highest TEA pressure) vs. TEA partial pressure. Figure 5.19 clearly shows the trend of adsorption saturation with cycling of the same sample, and the double reciprocal plots yield straight lines (correlation coefficients: 0.97-0.99), validating the choice of the Langmuir model. The adsorption equilibrium constant, K , can be computed from the slope and corresponds to the adduct formation constant. K values of 300 and 380 atm^{-1} are obtained for the 2nd and 3rd cycle, respectively. These adsorption constants for the CdSe aerogel sensor are around an order of magnitude larger than those observed in the CdSe single crystal study for NH_3 (15-30 atm^{-1}) and CH_3NH_2 (30-70 atm^{-1}).¹⁴⁵ This may be due in part to the relative basicities of the analytes investigated. Because NH_3 ($\text{pK}_b = 4.7$) and CH_3NH_2 ($\text{pK}_b = 3.4$) are less basic than TEA ($\text{pK}_b = 3.2$), a higher concentration of CdSe-adduct species may be expected to form in the latter case, reflected in the large equilibrium constant.

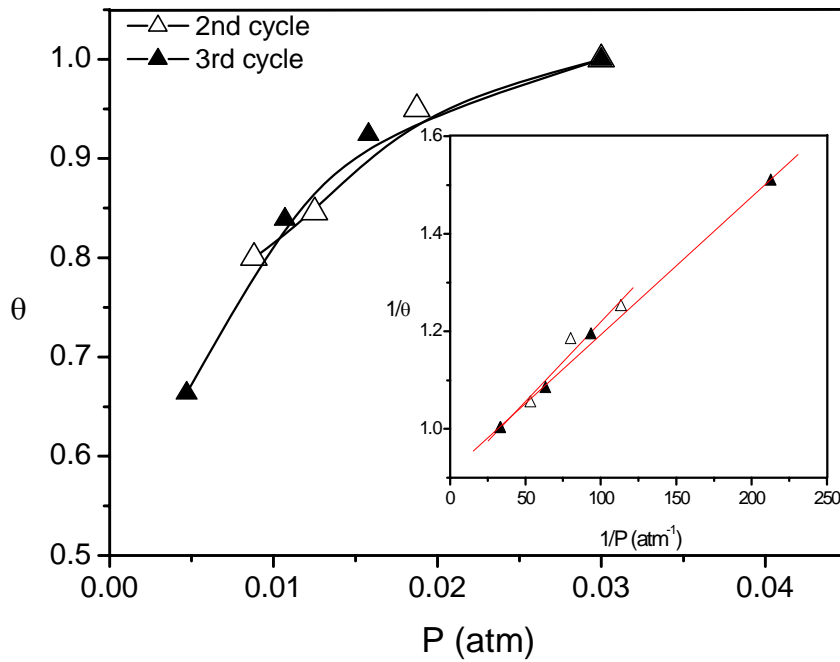


Figure 5.19 Langmuir adsorption isotherm for sample A for the 2nd and 3rd testing cycles; the lines serve to guide the eyes. The inset presents a double-reciprocal plot for the same data; the lines represent a linear fit of the data. Reproduced with permission from ref ¹³⁶. Copyright 2010 IOP.

5.4. Conclusions

For the first time, CdSe aerogels have been investigated for gas sensing applications. The sensing results show a significant and concentration-dependent luminescence intensity change when CdSe aerogels are exposed to the Lewis base triethylamine, and this response is largely reversible. In analogy to single-particle sensing experiments conducted previously with CdSe nanoparticles,¹³⁵ we show that sensing can be achieved by considering the aggregate PL response of a bulk monolith of particles. Furthermore, because individual nanoparticles exhibit variable responses, necessitating the averaging of data for a large number of particles in single-particle sensing studies, the sensing response of an aggregate is expected to be more reproducible than single-particle sensing, an expectation borne out by the two independently prepared samples tested here, as well as more suitable for conventional and portable sensing equipment.

CHAPTER 6

CONCLUSIONS AND PROSPECTUS

1D-, 2D- and 3D-assembled nanostructures are attracting considerable scientific attention due to their size and architecture-dependent physical properties. Among nanostructures, aerogels represent one class of porous materials consisting of a 3D solid framework assembled from primary nanoparticles without intervening ligands.^{67, 68, 75} The low dimensional solid network and interconnected pore space result in many unique physical properties, and hence has led to their utilization in a range of applications, such as catalysis, battery prototypes, and thermal/acoustic insulation.^{67, 68} However, aerogel research has been traditionally focused on insulating or wide band-gap metal oxides, thereby limiting the range of properties and applications for which they are suited. Semiconducting metal chalcogenide (ME, E = S, Se, Te) aerogels extend the range of aerogel properties by using direct band-gap semiconductors as the primary assembly unit, thereby covering the region in the spectrum from UV/Visible to near-IR.³¹ Hence, many interesting properties and applications which are not accessible with unmodified metal oxide aerogels can potentially be achieved with ME aerogels, such as photovoltaic and photoluminescent sensor devices. Our group has previously developed a systematic synthetic strategy for metal sulfide and selenide aerogels, including PbS, CdS, ZnS and CdSe, using sol-gel route involving (1) preparation of trioctylphosphine oxide capped nanocrystals; (2) surface exchange with thiolate capping ligands; (3) oxidative loss of thiolate ligands; (4) oxidative gelation of nanocrystals; (5) supercritical drying of resultant wet gels.^{31, 34, 110, 152}

This dissertation was mainly focused on synthesis, characterization and applications

of ME aerogels. The primary goals are to (1) explore the suitability of the sol-gel synthetic method developed for sulfides and selenides for high surface area tellurides (CdTe) and evaluate the validity of the proposed gelation mechanism for CdSe assembly for CdTe (2) study cation-exchange reactions of primary metal chalcogenide gels as a route to the synthesis of new compositions of aerogels; (3) investigate the suitability of CdSe aerogels as optical sensors to Lewis bases; study the sensitivity of the luminescence property of the aerogel to the change of surface characteristics and determine the accessibility of the metal chalcogenide aerogels to small molecules.

In the dissertation research, the synthesis of CdTe aerogels was explored by using primary CdTe nanocrystals with different surface ligation chemistry and the physicochemical properties of the resultant aerogels were evaluated. Prior studies of sol-gel reactions of chalcogenides were performed in systems where the nanocrystals had thiolate ligated surfaces. This often required a thiolate capping step before gelation was conducted. Recently the Brock group reported the mechanism of gelation for metal chalcogenides.⁹⁶ During gelation, surface thiolate groups are first oxidatively removed either by a chemical oxidizing agent (TNM) or by photo-oxidation in the presence of air, liberating disulfides and other oxidized species. The exposed surface chalcogenide ions (E^{2-}) on the nanocrystals are then oxidized into $(E_2)^{2-}$ or $(E_n)^{2-}$, which are responsible for the interparticle bonding. Therefore, we surmise that nanocrystals without thiolate ligation can also be gelled as long as suitable depassivation of the nanocrystal surface can be achieved, potentially enabling time and cost-efficient gelation by removal of the thiolate capping step.

In Chapter 3, the assembly of CdTe aerogels from thiolate (MHA) coated and nonthiolate (TOPO) coated CdTe nanocrystals was demonstrated via the sol-gel synthetic

route previously developed for sulfides and selenides. The resultant materials retain the same crystal structure and nanocrystallinity of the primary nanocrystals. Both of the aerogels exhibit high BET surface areas and broad BJH pore size distributions (extending from micro through meso to macro-sized pores). Although the aerogels are a 3-D connected architecture, the intrinsic quantum confined optical properties of the nanoparticulate building blocks are still observed. Overall, the TOPO-capped and MHA-capped aerogels exhibit similar physicochemical properties regardless of the different surface ligation. However, the obtained aerogels show poor luminescence compared to recently reported CdTe gels and aerogels,¹⁰⁸ perhaps due to over-oxidation of the nanocrystals. This is a problem for tellurides in particular because they are so easily oxidized.

To improve the luminescence properties of CdTe aerogels, better control of the exposure of the nanocrystal surface to oxidizing agents is recommended. For example, slow centrifugation after the first sign of a viscosity change followed by washing might be a choice¹⁰⁸ to efficiently remove excess amount of oxidants and prevent over oxidation.

In order to extend the existing aerogel compositions and properties, a novel synthesis method for generating new metal chalcogenide aerogels by cation exchange reactions of CdSe wet gels was explored. The simplicity and efficiency of cation-exchange reactions has been demonstrated in nanoparticle systems for the preparation of new nanoparticle phases by treating the precursor nanoparticles with concentrated cation solutions.^{48, 49, 112} This synthesis route takes advantage of the low activation energy barrier on the nanoscale for diffusion of ions throughout the solid lattice as compared to their bulk counterparts.⁴⁹ Although metal chalcogenide aerogels are macroscopic assemblies, they are composed of nanoscale building blocks. Therefore, it was surmised that cation-exchange reactions should also be kinetically

rapid in the metal chalcogenide gel systems.

Chapter 4 of the dissertation study demonstrated the successful synthesis of Ag_2Se , CuSe and PbSe gels and aerogels by employing cation-exchange reactions of CdSe wet gels followed by supercritical CO_2 drying. The cation-exchange reactions were found to be simple, rapid and efficient. The resultant aerogels exhibit similar crystallite size, morphology, surface area and pore characteristics compared to the CdSe gel precursor, suggesting the bonding that is responsible for the formation of the gel network is not changed globally. In addition, it was observed that the monolithic shape of the precursor gel body was maintained all through the exchange process, suggesting the predominant motion is the diffusion of cations through the stationary anion sublattice in individual nano building blocks. Another important finding of the study is that partial cation exchanged gels and aerogels can be prepared by controlling the total amount of exchanging cations. Overall, this study reveals an alternative approach for the preparation of metal chalcogenide aerogels, particularly suitable for those systems where the synthesis methodology for nanoparticle precursors is not well developed or the parameters governing the gelation process have not been determined. The Ag_2Se , CuSe and PbSe aerogels are expected to have potential applications in 3-D batteries, electronic sensors, solar cells, IR detectors and photovoltaic absorbers, all of which are expected to benefit from an interconnected solid framework with a large interfacial surface area. The partially exchanged aerogels are potentially useful for applications that require composite aerogel architectures.

The thermodynamic driving forces for these cation-exchange reactions originate from the distinctive differences of the solubility product constants between the produced gel and the initial gel. The soft Lewis basic characteristic of the chalcogenide framework is responsible for preferential exchange by soft metal ions. Accordingly, chalcogenide aerogels

may be appropriate for heavy metal ion removal from contaminated water or other solvent media based on ion-exchange. Because the exchange process involves release of ions, the exchanged ions should not be toxic or should be less toxic than the adsorbed ions. Therefore, a continued study of cation-exchange chemistry focused on ZnS gels with various heavy metal ions (e.g. Cd^{2+} , Pb^{2+}) in aqueous solution is currently under investigation.

The dissertation research has also studied the sensing responses of highly porous CdSe aerogels to triethylamine (TEA). Aerogels are promising materials in sensing applications due to their high internal surface area and large open pore structure, which facilitates rapid diffusion of analyte molecules to the reactive sites on the surface of individual nanoparticles.^{67, 110} Further, by taking advantage of the intrinsic visible-range luminescence properties, metal chalcogenide aerogels are particularly interesting for optical sensing applications.¹¹⁰

Previous studies have demonstrated enhanced photoluminescence intensity in CdSe single crystals (bulk phase materials),²¹ and in discrete nanoparticles, in the presence of Lewis bases (e.g. amines).²² A similar sensing principle is applicable to CdSe aerogels due to the inherent Lewis acidic surface characteristics of the individual nano building blocks. TEA was chosen as the sensing analyte because (1) TEA was used in the discrete CdSe nanoparticle study; (2) TEA is a liquid and volatile, and can be transported to the gas phase for sensing by bubbling with an inert carrier gas.

As described in Chapter 5, CdSe aerogels showed significant and reversible enhancement of photoluminescence intensity upon exposure to TEA relative to the intensity at the argon reference level. The enhancement is concentration dependant and sensitively affected by surface characteristics of the aerogel. Importantly, the sensing study provides key

insights into the functional behavior of CdSe aerogels. These include the observations: (1) that the porosity enables access of bulky molecules (relative to nitrogen, used in porosimetry studies) to active surface sites, (2) that the oxidative conditions under which gelation occurs do not inhibit the native sensing ability of the individual quantum dot building blocks; (3) that vacuum heating, even at modest temperatures, completely suppresses any sensing, possibly due to oxidation and formation of a thick dead layer; and (4) that the surfaces are not just responsive, but also reactive (i.e., reactive gases can lead to dissociation of residual ligands), thus potentially opening the door to post-synthetic functionalization in these systems.

While the aerogels presented here are not expected to exhibit a high degree of specificity, a recent study showed that different PL response profiles could be obtained for polar and nonpolar gases by tuning the sizes of CdSe nanoparticles.¹⁵³ This suggests that multiplex sensing may be feasible in composite aerogels assembled from nanoparticles of a range of sizes.

Over all, this dissertation research has produced three key outcomes. (1) The synthesis of high surface area CdTe aerogels from thiolate capped and nonthiolate capped nanocrystals via oxidation induced sol-gel assembly and the demonstration that thiolate capping is not a prerequisite to gelation; (2) The establishment of cation-exchange reactions as a simple and efficient approach for the preparation of new compositions of metal chalcogenide aerogels; and (3) the demonstration of reversible bulk-phase photoluminescent response of metal chalcogenide monoliths to external chemical agents bound at the high surface area interface.

REFERENCES

- (1) Trindade, T.; O'Brien, P.; Pickett, N., *Chem. Mater.* **2001**, *13*, 3843-3858.
- (2) West, A. R., *Basic Solid State Chemistry* Second ed.; Jonh Wiiey & Sons, Ltd: New York, 1999.
- (3) Klimov, V. I., *Semiconductor and Metal Nanocrystals*. Marcel Dekker, Inc: New York, 2004.
- (4) Alivisatos, A. P., *Science* **1996**, *271*, 933-937.
- (5) Steigerwald, M. L.; Brus, L. E., *Acc. Chem. Res.* **1990**, *23*, 183-188.
- (6) Brus, L. E., *J. Chem. Phys* **1983**, *79*, 5566-5571.
- (7) Brus, L. E., *J. Chem. Phys* **1984**, *80*, 4403-4407.
- (8) Murray, C. B.; Norris, D. J.; Bawendi, M. G., *J. Am. Chem. Soc.* **1993**, *115* (19), 8706-8715.
- (9) Murray, C. B.; Kagan, C. R.; Bawendi, M. G., *Annu. Rev. Mater. Sci.* **2000**, *30*, 545-610.
- (10) Peng, Z. A.; Peng, X., *J. Am. Chem. Soc.* **2001**, *2001*, 183-184.
- (11) Qu, L.; Peng, Z. A.; Peng, X., *Nano Letters* **2001**, *1* (6), 333-337.
- (12) Yu, W. W.; Wang, Y. A.; Peng, X., *Chem. Mater.* **2003**, *15* (22), 4300-4308.
- (13) Chestnoy, N.; Harris, T. D.; Hull, R.; Brus, L. E., *J. Phys. Chem.* **1986**, *90* (15), 3393-3399.
- (14) Somers, R. C.; Bawendi, M. G.; Nocera, D. G., *Chem. Soc. Rev.* **2007**, *36*, 579-591.
- (15) Alivisatos, A. P., *Science* **1998**, *281*, 2013-2016.
- (16) Dubertret, B.; Skourides, P.; Norris, D. J.; Noireaux, V.; Brivanlou, A. H.; Libchaber,

- A., *Science* **2002**, *298*, 1759-1762.
- (17) Wu, X.; Liu, H.; Liu, J.; Haley, K. N.; Treadway, J. A.; Larson, J. P.; Ge, N. P., F; Bruchez, M. P., *Nat. Biotechnol.* **2003**, *21*, 41-46.
- (18) Guo, W.; Li, J. J.; Wang, Y. A.; Peng, X., *Chem. Mater.* **2003**, *15* (16), 3125-3133.
- (19) Kim, S.; Bawendi, M. G., *J. Am. Chem. Soc.* **2003**, *125* (48), 14652-14653.
- (20) Colvin, V. L.; Schlamp, M. C.; Alivisatos, A. P., *Nature* **1994**, *370*, 354-357.
- (21) Meyer, G. J.; Lisensky, G. C.; Ellis, A. B., *J. Am. Chem. Soc.* **1988**, *110*, 4914-4918.
- (22) Nazzal, A. Y.; Qu, L. H.; Peng, X. G.; Xiao, M., *Nano lett.* **2003**, *3*, 819-822.
- (23) Willard, D. M.; Carillo, L. L.; Jung, J.; Van Orden, A., *Nano Lett.* **2001**, *1* (9), 469-474.
- (24) Patolsky, F.; Gill, R.; Weizmann, Y.; Mokari, T.; Banin, U.; Willner, I., *J. Am. Chem. Soc.* **2003**, *125* (46), 13918-13919.
- (25) Gill, R.; Willner, I.; Shweky, I.; Banin, U., *J. Phys. Chem. B* **2005**, *109* (49), 23715-23719.
- (26) Goldman, E. R.; Medintz, I. L.; Whitley, J. L.; Hayhurst, A.; Clapp, A. R.; Uyeda, H. T.; Deschamps, J. R.; Lassman, M. E.; Mattoussi, H., *J. Am. Chem. Soc.* **2005**, *127* (18), 6744-6751.
- (27) Sargent, E. H., *Adv. Mater.* **2005**, *17*, 515-522.
- (28) Yoffe, A. D., *Adv. Phys.* **2001**, *50*, 1-208.
- (29) Hu, J.; Odom, T. W.; Lieber, C. M., *Acc. Chem. Res.* **1999**, *32* (5), 435-445.
- (30) Steigerwald, M. L.; Alivisatos, A. P.; Gibson, J. M.; Harris, T. D.; Kortan, R.; Muller, A. J.; Thayer, A. M.; Duncan, T. M.; Douglass, D. C.; Brus, L. E., *J. Am. Chem. Soc.* **1988**, *110* (10), 3046-3050.

- (31) Mohanan, J. L.; Arachchige, I. U.; Brock, S. L., *Science* **2005**, *307*, 397-400.
- (32) Gacoin, T.; Malier, L.; Boilot, J.-P., *Chem. Mater.* **1997**, *9*, 1502-1504.
- (33) Fendler, J. H., *Chem. Rev.* **1987**, *87* (5), 877-899.
- (34) Arachchige, I. U.; Brock, S. L., *J. Am. Chem. Soc.* **2006**, *128*, 7964-7971.
- (35) LaMer, V. K.; Dinegar, R. H., *J. Am. Chem. Soc.* **1950**, *72* (11), 4847-4854.
- (36) Burda, C.; Chen, X.; Narayanan, R.; El-Sayed, M. A., *Chem. Rev.* **2005**, *105* (4), 1025-1102.
- (37) Peng, X.; Wickham, J.; Alivisatos, A. P., *J. Am. Chem. Soc.* **1998**, *120* (21), 5343-5344.
- (38) Talapin, D. V.; Haubold, S.; Rogach, A. L.; Kornowski, A.; Haase, M.; Weller, H., *J. Phys. Chem. B* **2001**, *105* (12), 2260-2263.
- (39) Jose, R.; Biju, V.; Yamaoka, Y.; Nagase, T.; Makita, Y.; Shinohara, Y.; Baba, Y.; Ishikawa, M., *Appl. Phys. Mater. Sci. Process.* **2004**, *79* (8), 1833-1838.
- (40) Yang, Y. A.; Wu, H.; Williams, K. R.; Cao, Y. C., *Angew: Chem. Int. Ed.* **2005**, *44*, 6712-6715.
- (41) Gao, M.; Kirstein, S.; Mohwald, H.; Rogach, A. L.; Kornowski, A.; Eychmuller, A.; Weller, H., *J. Phys. Chem. B* **1998**, *102* (43), 8360-8363.
- (42) Gaponik, N.; Talapin, D. V.; Rogach, A. L.; Hoppe, K.; Shevchenko, E. V.; Kornowski, A.; Eychmuller, A.; Weller, H., *J. Phys. Chem. B* **2002**, *106* (29), 7177-7185.
- (43) Rogach, A. L.; Franzl, T.; Klar, T. A.; Feldmann, J.; Gaponik, N.; Lesnyak, V.; Shavel, A.; Eychmuller, A.; Rakovich, Y. P.; Donegan, J. F., *J. Phys. Chem. C* **2007**, *111* (40), 14628-14637.

- (44) Fedorov, V. A.; Ganshin, V. A.; Korkishko, Y. N., *Phys. Status Solidi A* **1993**, *139*, 9-65.
- (45) Chen, C.-C.; Herhold, A. B.; Johnson, C. S.; Alivisatos, A. P., *Science* **1997**, *276*, 398-401.
- (46) Dloczik, L.; Könenkamp, R., *Nano Lett.* **2003**, *3*, 651-653.
- (47) Dloczik, L.; Könenkamp, R., *J. Solid State Electrochem.* **2004**, *8*, 142-146.
- (48) Son, D. H.; Hughes, S. M.; Yin, Y.; Alivisatos, A. P., *Science* **2004**, *306*, 1009-1012.
- (49) Wark, S. E.; Hsia, C.; Son, D. H., *J. Am. Chem. Soc.* **2008**, *130*, 9550-9555.
- (50) Camargo, P. H. C.; Lee, Y. H.; Jeong, U.; Zou, Z.; Xia, Y., *Langmuir* **2007**, *23*, 2985-2992.
- (51) Cumberland, S. L.; Hanif, K. M.; Javier, A.; Khitrov, G. A.; Strouse, G. F.; Woessner, S. M.; Yun, C. S., *Chem. Mater.* **2002**, *14* (4), 1576-1584.
- (52) Manna, L.; Scher, E. C.; Alivisatos, A. P., *J. Am. Chem. Soc.* **2000**, *122* (51), 12700-12706.
- (53) Peng, Z. A.; Peng, X., *J. Am. Chem. Soc.* **2002**, *124* (13), 3343-3353.
- (54) Tang, Z.; Kotov, N. A.; Giersig, M., *Science* **2002**, *2002*, 237-240.
- (55) Torimoto, T.; Yamashita, M.; Kuwabata, S.; Sakata, T.; Mori, H.; Yoneyama, H., *J. Phys. Chem. B* **1999**, *103* (42), 8799-8803.
- (56) Tang, Z.; Zhang, Z.; Wang, Y.; Glotzer, S. C.; Kotov, N. A., *Science* **2006**, *314*, 274-278.
- (57) Lin, Y.; Skaff, H.; Beker, A.; Dinsmore, A. D.; Emrick, T.; Russell, T. P., *J. Am. Chem. Soc.* **2003**, *125* (42), 12690-12691.
- (58) Cho, Y. H.; Cho, G.; Lee, J.-S., *Adv. Mater.* **2004**, *16*, 1814-1817.

- (59) Shavel, A.; Gaponik, N.; Eychmüller, A., *Eur. J. Inorg. Chem.* **2005**, 2005, 3613-3623.
- (60) Franzl, T.; Shavel, A.; Rogach, A. L.; Gaponik, N.; Klar, T. A.; Eychmüller, A.; Feldmann, J., *Small* **2005**, 1, 392-395.
- (61) Puentes, V. F.; Krishnan, K. M.; Alivisatos, A. P., *Appl. Phys. Lett.* **2001**, 78, 2187-2189.
- (62) Whetten, R. L.; Shafiqullin, M. N.; Khoury, J. T.; Schaaff, T. G.; Vezmar, I.; Alvarez, M. M.; Wilkinson, A., *Acc. Chem. Res.* **1999**, 32 (5), 397-406.
- (63) Zheng, N.; Fan, J.; Stucky, G. D., *J. Am. Chem. Soc.* **2006**, 128 (20), 6550-6551.
- (64) Murray, C. B.; Kagan, C. R.; Bawendi, M. G., *Science* **1995**, 270, 1335-1338.
- (65) Motte, L.; Billoudet, F.; Lacaze, E.; Pileni, M. P., *Adv. Mater.* **1996**, 8, 1018-1020.
- (66) Redl, F. X.; Cho, K.-S.; Murray, C. B.; O'Brien, S., *Nature* **2003**, 423, 968-971.
- (67) Rolison, D. R.; Dunn, B., *J. Mater. Chem.* **2001**, 11, 963-980.
- (68) Hüsing, N.; Schubert, U., *Angew. Chem. Int. Ed.* **1998**, 37, 22-45.
- (69) Tewari, P. H.; Hunt, A. J.; Lofftus, K. D., *Mater. Lett.* **1985**, 3, 363-367.
- (70) Harreld, J. H.; Dong, W.; Dunn, B., *Mater. Res. Bull.* **1998**, 33, 561-567.
- (71) Leventis, N.; Elder, I. A.; Rolison, D. R.; Anderson, M. L.; Merzbacher, C. I., *Chem. Mater.* **1999**, 11, 2837-2845.
- (72) Willi, R.; Koppel, R. A.; Baiker, A., *Ind. Eng. Chem. Res.* **1997**, 36 (8), 3013-3018.
- (73) Fanelli, A. J.; Verma, S.; Engelmann, T.; Burlew, J. V., *Ind. Eng. Chem. Res.* **1991**, 30 (1), 126-129.
- (74) Rolison, D. R., *Science* **2003**, 299, 1698-1701.
- (75) Pierre, A. C.; Pajonk, G. M., *Chem. Rev.* **2002**, 102 (11), 4243-4266.

- (76) Pierre, M.; Buisson, P.; Fache, F.; Pierre, A., *Biocatal. Biotransform.* **2000**, *18*, 237-251.
- (77) Power, M.; Hosticka, B.; Black, E.; Daitch, C.; Norris, P., *J. Non-Cryst. Solids* **2001**, *285*, 303-308.
- (78) Ivanisevic, A.; Yeh, J.; Mawst, L.; Kuech, T. F.; Ellis, A. B., *Nature* **2001**, *409*, 476.
- (79) Rolison, D. R.; Dunn, B. J., *J. Mater. Chem.* **2001**, *11*, 963-980.
- (80) Plalta, D. L.; Briones, Y. J.; Wolfe, R. L.; Carroll, M. K.; Bakrania, S. D.; Mandel, S. G.; Anderson, A. M., *J. Non-Cryst. Solids* **2004**, *350*, 326-335.
- (81) Leventis, N.; Rawashdeh, A. M.; Elder, I. A.; Yang, J.; Dass, A.; Sotiriou-Leventis, C., *Chem. Mater.* **2004**, *16*, 1493-1506.
- (82) Ayers, M. R.; Hunt, A. J., *J. Non-Cryst. Solids* **1998**, *225*, 343-347.
- (83) Lakowicz, J. R., *Principles of Fluorescence Spectroscopy*. Kluwer Academic/Plenum Publishers: 1999.
- (84) Wallace, J. M.; Rice, J. K.; Pietron, J. J.; Stroud, R. M.; Long, J. W.; Rolison, D. R., *Nano Letters* **2003**, *3* (10), 1463-1467.
- (85) Kistler, S. S., *Nature* **1931**, *127*, 741-741.
- (86) Foster, H. D.; Keyes, D. B., *Ind. Eng. Chem.* **1937**, *29*, 1254-1260.
- (87) Pekala, R. W.; Mayer, S. T.; Poco, J. F.; Kaschmitter, J. L., *Mat. Res. Soc. Symp. Proc.* **1994**, *349*, 79-84.
- (88) Mohanan, J. L.; Brock, S. L., *J. Non-Cryst. Solids* **2004**, *350*, 1-8.
- (89) Allen, G. C.; Paul, M.; Dunleavy, M., *Adv. Mater.* **1992**, *4*, 424-427.
- (90) Sriram, M. A.; Kumta, P. N., *J. Mater. Chem.* **1998**, *8*, 2441-2451.
- (91) Carmalt, C. J.; Dinnage, C. W.; Parkin, I. P.; White, A. J. P.; Williams, D. J., *Inorg.*

- Chem.* **2002**, *41*, 3668-3672.
- (92) Seisenbaeva, G. A.; Gohil, S.; Jansson, K.; Herbst, K.; Brorson, M.; Kessler, V. G., *New J. Chem.* **2003**, *27*, 1059-1064.
- (93) Gacoin, T.; Malier, L.; Boilot, J.-P., *J. Mater. Chem.* **1997**, *7*, 859-860.
- (94) Gacoin, T.; Lahlil, K.; Larregaray, P.; Boilot, J.-P., *J. Phys. Chem. B* **2001**, *105*, 10228-10235.
- (95) Arachchige, I. U.; Brock, S. L., *J. Am. Chem. Soc.* **2007**, *129* (7), 1840-1841.
- (96) Pala, I. R.; Arachchige, I. U.; Georgiev, D. G.; Brock, S. L., *Angew. Chem. Int. Ed.* **2010**, *49*, 3661-3665.
- (97) Yu, W. W.; Qu, L.; Guo, W.; Peng, X., *Chem. Mater.* **2003**, *15* (14), 2854-2860.
- (98) Manna, L.; Milliron, D. J.; Meisel, A.; Scher, E. C.; Alivisatos, A. P., *Nature Mater.* **2003**, *2*, 382-385.
- (99) Ma, J.; Chen, J.-Y.; Zhang, Y.; Wang, P.-N.; Guo, J.; Yang, W.-L.; Wang, C.-C., *J. Phys. Chem. B* **2007**, *111* (41), 12012-12016.
- (100) Smith, A. M.; Nie, S., *Angew. Chem. Int. Ed.* **2008**, *47*, 9916-9921.
- (101) Gaponik, N. P.; Talapin, D. V.; Rogach, A. L., *Phys. Chem. Chem. Phys.* **1999**, *1*, 1787-1789.
- (102) Lin, Y.-W.; Tseng, W.-L.; Chang, H.-T., *Adv. Mater.* **2006**, *18*, 1381-1386.
- (103) Bertoni, C.; Gallardo, D.; Dunn, S.; Gaponik, N.; Eychmuller, A., *Appl. Phys. Lett.* **2007**, *90*, 034107/1-034107/3.
- (104) Boyle, D. S.; Hearne, S.; Johnson, D. R.; O'Brien, P., *J. Mater. Chem.* **1999**, *9*, 2879-2883.
- (105) Kosyachenko, L. A.; Mathew, X.; Motushchuk, V. V.; Sklyarchuk, V. M., *Sol.*

- Energy* **2006**, *80*, 148-155.
- (106) Deng, Z.; Zhang, Y.; Yue, J.; Tang, F.; Wei, Q., *J. Phys. Chem. B* **2007**, *111*, 12024-12031.
- (107) Zhang, L.; Zou, X.; Ying, E.; Dong, S., *J. Phys. Chem. C* **2008**, *112*, 4451-4454.
- (108) Gaponik, N.; A., W.; Marx, R.; Lesnyak, V.; Schilling, K.; Eychmu" ller, A., *Adv. Mater.* **2008**, *20*, 4257-4262.
- (109) Chen, H.; Lesnyak, V.; Bigall, N. C.; Gaponik, N.; Eychmuller, A., *Chem. Mater.* **22** (7), 2309-2314.
- (110) Arachchige, I. U.; Brock, S. L., *Acc. Chem. Res.* **2007**, *40* (9), 801-809.
- (111) Arachchige, I. U.; Mohanan, J. L.; Brock, S. L., *Chem. Mater.* **2005**, *17* (26), 6644-6650.
- (112) Dzhafarov, T. D.; Serin, M.; Ören, D.; Süngü, B.; Sadigov, M. S., *J. Phys. D: Appl. Phys.* **1999**, *32*, L5-L8.
- (113) Lubeck, C. R.; Han, T. Y.; Gash, A. E.; Satcher, J. H., Jr. ; Doyle, F. M., *Adv. Mater.* **2006**, *18*, 781-784.
- (114) Ayers, M. R.; Hunt, A. J., *J. Non-Cryst. solids* **1998**, *225*, 343-347.
- (115) Plalta, D. L.; Briones, Y. J.; Wolfe, R. L.; Carroll, M. K.; Bakrania, S. D.; Mandel, S. G.; Anderson, A. M., *J. Non-Cryst. Solids* **2004**, *350*, 326-335.
- (116) Arachchige, I. U.; Brock, S. L., *J. Am. Chem. Soc.* **2007**, *129*, 1840-1841.
- (117) Brock, S. L.; Arachchige, I. U.; Kalebaila, K. K., *Comm. Inorg. Chem.* **2006**, *27*, 103-126.
- (118) Shriver, D. F.; Drezdson, M. A., *The Manipulation of Air-Sensitive Compounds*. Wiler-Interscience Publication: New York, Chichester, Brisbane, Toronto, Singapore,

- 1986.
- (119) Flewitt, P. E. J.; Wild, R. K., *Physical Methods for Materials Characterisation*. Institute of Physics Publishing: Bristol and Philadelphia, 1994.
- (120) *Surf. Interface Anal.* **1988**, *11*, 119-124.
- (121) Gregg, S. J.; Sing, K. S. W., *Adsorption, Surface Area and Porosity*. 2nd ed.; Academic Press: New York, 1982.
- (122) Webb, P. A.; C., O., *Analytical Methods in Fine Particle Technology*. Micromeritics: Norcross (Georgia), 1997.
- (123) Settle, F. A., *Handbook of Instrumental Techniques for Analytical Chemistry* Prentice Hall PTR: Upper Saddle River, NJ 1997.
- (124) Wendlandt, W. W.; Helcht, H. G., *Reflectance Spectroscopy*. Interscience: New York, 1966.
- (125) Tandon, S. P.; Gupta, J. P., *Phys. Stat. Sol.* **1970**, *38*, 363-367.
- (126) Frei, R. W.; MacNeil, J. D., *Diffuse Reflectance Spectroscopy in Environmental Problem-Solving*. CRC: Ohio, 1973.
- (127) Harvey, D., *Modern Analytical Chemistry*. The McGraw-Hill Companies, Inc.: Boston Burr Ridge, IL Dubuque, IA Madison, WI New York San Francisco St. Louis, Bangkok Bogotá Caracas Lisbon London Madrid Mexico City Milan New Delhi Seoul Singapore Sydney Taipei Toronto, 2000.
- (128) Peng, Z. A.; Peng, X., *J. Am. Chem. Soc.* **2001**, *123*, 183-184.
- (129) Aldana, J.; Wang, Y. A.; Peng, X., *J. Am. Chem. Soc.* **2001**, *123*, 8844-8850.
- (130) Brock, S. L.; Arachchige, I. U.; Kalebaila, K. K., *Comments on Inorganic Chemistry*, **2006**, *27*, 103-126.

- (131) Yao, Q.; Arachchige, I. U.; Brock, S. L., *J. Am. Chem. Soc.* **2009**, *131* (8), 2800-2801.
- (132) Liu, I.; Lo, H.; Chien, C.; Lin, Y.; Chen, C.; Chen, Y.; Su, W.; Liou, S., *Journal of Materials Chemistry* **2008**, *18*, 675-682.
- (133) Bouroushian, M., *Electrochemistry of Metal Chalcogenides*. Springer-Verlag Berlin, Heidelberg, 2010.
- (134) Boolchand, P.; Bresser, W. J., *Nature* **2001**, *410*, 1070-1073.
- (135) Nazzal, A. Y.; Qu, L. H.; Peng, X. G.; Xiao, M., *Nano lett.* **2003**, *3*, 819-822.
- (136) Yao, Q.; Brock, S. L., *Nanotechnology* **2010**, *21* (115502), 1-10.
- (137) Peng, Z. A.; Peng, X. G., *J. Am. Chem. Soc.* **2001**, *123*, 183-184.
- (138) Borchert, H.; Shevchenko, E. V.; Robert, A.; Mekis, I.; Kornowski, A.; Grübel, G.; Weller, H., *Langmuir* **2005**, *21*, 1931-1936.
- (139) Brus, L. E., *J. Chem. Phys.* **1983**, *79*, 5566-5571.
- (140) Pejova, B.; Tanusevski, A.; Grozdanov, I., *J. Solid State Chem.* **2004**, *177*, 4785-4799.
- (141) Cullity, B. D., *Elements of X-ray Diffraction*. 2nd ed.; Addison-Wesley: Reading, MA, 1978.
- (142) Nirmal, M.; Brus, L. E., *Acc. Chem. Res.* **1999**, *32*, 407-414.
- (143) Raevskaya, A. E.; Stroyuk, A. L.; Kuchmii, S. Y., *J. Nanoparticle Res.* **2004**, *6*, 149-158.
- (144) Fujii, T.; Tanaka, N.; Tai, H.; Obara, S.; Ellis, A. B., *Bull. Chem. Soc. Jpn.* **2000**, *73*, 809-813.
- (145) Meyer, G. J.; Lisensky, G. C.; Ellis, A. B., *J. Am. Chem. Soc.* **1988**, *110*, 4914-4918.

- (146) Fujii, T.; Tanaka, N.; Tai, H.; Obara, S.; Ellis, A. B., *Bull. Chem. Soc. Jpn.* **2000**, *73*, 809-813.
- (147) Leventis, N.; Rawashdeh, A. M.; Elder, I. A.; Yang, J.; Dass, A.; Sotiriou-Leventis, C., *Chem. Mater.* **2004**, *16*, 1493-1506.
- (148) Wallace, J. M.; Rice, J. K.; Pietron, J. J.; Stroud, R. M.; Long, J. W.; Rolison, D. R., *Nano lett.* **2003**, *3*, 1463-1467.
- (149) Katari, J. E. B.; Colvin, V. L.; Alivisatos, A. P., *J. Phys. Chem.* **1994**, *98*, 4109-4117.
- (150) Murray, C. B.; Norris, D. J.; Bawendi, M. G., *J. Am. Chem. Soc.* **1993**, *115*, 8706-8715.
- (151) Wuister, S. F.; de Mello Donegá, C.; Mijerink, A., *J. Phys. Chem. B* **2004**, *108*, 17393-17397.
- (152) Brock, S. L.; Arachchige, I. U.; Kalebaila, K. K., *Comments Inorg. Chem.* **2006**, *27*, 103-126.
- (153) Potyrailo, R. A.; Leach, A. M., *Appl. Phys. Lett.* **2006**, *88*, 134110-134113.

ABSTRACT**METAL CHALCOGENIDE NANOCRYSTAL ASSEMBLY: FROM SYNTHESIS TO APPLICATIONS**

by

QINGHONG YAO**August 2010****Advisor:** Dr. Stephanie L. Brock**Major:** Chemistry**Degree:** Doctor of Philosophy

This dissertation study is focused on (1) the application of an oxidation-induced sol-gel assembly method to formation of CdTe aerogels; (2) extension of existing aerogel compositions and properties by an alternative synthetic approach: cation-exchange reactions; and (3) probing the functionality of CdSe aerogels as optical sensors of Lewis base analytes.

Highly porous CdTe aerogels were successfully synthesized by sol-gel assembly of CdTe nanocrystals with thiolate or nonthiolate (phosphine oxide) ligated surfaces by treatment with tetranitromethane. Both phosphine oxide-capped and the thiolate-capped aerogels exhibit similar structure, morphology and porosimetry properties, suggesting that precursor ligation does not have a no major effect on the gelation process and the resultant aerogel properties. These data clearly shows that thiolate capping is not a necessary step in the gelation process; the exposure of reactive sites and the subsequent surface oxidation reaction to form chalcogenide linkages is the key.

Cation-exchange reactions in metal chalcogenide gels were explored for the first time. Ag₂Se wet gel monoliths were successfully prepared by an ion-exchange reaction of a

monolithic CdSe wet gel and converted to an aerogel by drying under supercritical conditions. The newly prepared Ag₂Se aerogels adopt the cubic phase and exhibit a typical pearl-necklace morphology and the high surface area characteristics of aerogels. The ion-exchange synthesis route can also be successfully employed for other gel systems, including PbSe and CuSe.

The photoluminescence (PL) response of highly porous CdSe aerogels to triethylamine (TEA) is investigated and compared to prior studies on single crystals and nanoparticle-polymer composites. As-prepared CdSe aerogels show significant and reversible enhancement of luminescence intensity upon exposure to TEA relative to the intensity in pure argon carrier gas. The enhancement in the PL response is concentration-dependant and linear over the range of TEA concentration studied (4.7×10^3 - 75×10^3 ppm). The sensing response of previously tested samples exhibits saturation behavior that is modeled using Langmuir adsorption isotherms, yielding adsorption equilibrium constants in the range 300 to 380 atm⁻¹. The response is sensitively affected by the surface characteristics of the aerogel; when the wet gels are treated with pyridine prior to aerogel formation, the response to TEA is diminished, and when as-prepared aerogels are heated in a vacuum, no response is observed. Deactivation is attributed to an increase in surface oxide (SeO₂) and decrease in surface Cd²⁺ Lewis acid sites. Sensing runs of approximately one hour have little impact on the morphology or crystallinity of the aerogels, but do result in partial removal of residual thiolate ligands left over from the gelation process.

AUTOBIOGRAPHICAL STATEMENT

QINGHONG YAO

Education

- **2005-2010 Ph.D** Inorganic Chemistry, Wayne State University , Detroit, MI
Dissertation: Metal Chalcogenide Nanocrystal Assembly: from Synthesis to Application
Advisor: Prof. Stephanie L. Brock.
- **2000-2003 M.Sc.** Analytical Chemistry, Dalian Institute of Chemical Physics, Chinese Academy of Sciences, Dalian, China
Thesis title: Determination of urinary oxidative DNA damage marker 8-hydroxy-2'-deoxyguanosine and curcumin in Traditional Chinese Medicines: *curcuma* and *curcuma kwangsiensis*
Thesis Advisor: Prof. Guowang Xu
- **1996-2000 B.Sc.** Chemistry, Wuhan University, Wuhan, China

Research and Teaching Experience

- **08/2005-07/2010** Graduate Research/Teaching Assistant, Department of Chemistry, Wayne State University, Detroit, MI
- **08/2000-07/2003** Graduate Research Assistant, Dalian Institute of Chemical Physics, Chinese Academy of Sciences, Dalian, China

Technical Skills

- Experience with powder X-ray diffractometry, diffuse reflectance UV-Visible spectroscopy, dynamic light scattering, fluorescent microscopy, scanning electron microscopy, transmission electron microscopy, energy dispersive spectroscopy, thermogravimetric analysis, and porosimetry analysis, atomic absorption spectroscopy, infrared spectroscopy, UV-Visible spectroscopy, fluorescence spectroscopy

Awards and Fellowships

- Summer Dissertation Fellowship, 2009 summer, Graduate School, WSU
- Thomas C. Rumble University Graduate Fellowship, 2009-2010, Graduate School, WSU

Publications

- **Yao, Q.;** Brock, S. L., *Nanotechnology* **2010**, 21, 115502-115512
- **Yao, Q.;** Arachchige, I. U.; Brock, S. L., *J. Am. Chem. Soc.* **2009**, 131(8), 2800-2801
- Mei, S.; **Yao, Q.;** Wu, C.; Xu, G., *J. Chromatogr. B*, **2005**, 827, 83–87
- Xu, G.; **Yao, Q.;** Su, B.; Zhang, X.; Xiong, J., *J. Pharmaceu. Biomed. Anal.* **2004**, 36, 101–104
- **Yao, Q.;** Mei, S.; Weng, Q.; Zhang, P.; Yang, Q.; Wu, C.; Xu, G., *Talanta*, **2004**, 63, 617-623.
- Mei, S.; **Yao, Q.,** Cai, L.; Xing, J.; Xu, G., *Electrophoresis* **2003**, 24, 1411-1415